Doctoral Dissertation
Doctoral Program in Chemical Engineering (35th Cycle)

# Doped ZnO nanoparticles in biomedicine: their role as stimuli-responsive anticancer agents

By

**Marco Carofiglio**

******

**Supervisor:**
Prof. Valentina Cauda

Politecnico di Torino
2022

# Declaration

I hereby declare that the contents and organization of this dissertation does not compromise in any way the rights of third parties, including those relating to the security of personal data. This dissertation is my own work and work done in collaboration with others.

Most of the chapters of this dissertation are based on research published in scientific journals and available in open access:

Chapter 1: **M. Carofiglio**, S. Barui, V. Cauda, M. Laurenti "*Doped zinc oxide nanoparticles: synthesis, characterization and potential use in nanomedicine*" Applied Sciences, 2020, Vol. 10(15), pp. 5194, EISSN 2076-3417, DOI: 10.3390/app10155194

Chapter 2: **M. Carofiglio**, M. Laurenti, V. Vighetto, L. Racca, S. Barui, N. Garino, R. Gerbaldo, F. Laviano, V. Cauda "*Iron-Doped ZnO Nanoparticles as Multifunctional Nanoplatforms for Theranostics. Nanomaterials*" Nanomaterials, 2021; 11(10):2628. DOI: 10.3390/nano11102628

Chapter 3: **M. Carofiglio**, M. Conte, L. Racca, V. Cauda "*Synergistic phenomena between iron-doped ZnO nanoparticles and shock waves exploited against pancreatic cancer cells*" ACS Applied Nanomaterials, doi:10.1021/acsanm.2c04211

Marco Carofiglio

2022

*To Paola, mamma and papà*

# Acknowledgment

If the research work that follows these words is finally written down, it is undoubtedly due to all the people I met during these years. Most of them have given me a lot in terms of personal growth and support, sometimes even more than help with research and academic matters. Here, I would limit my acknowledgement to the academic and scientific side, because compressing in a bunch of words the gratitude I have towards all of them would be far too reductive.

I would like to start from my supervisor, Prof. Valentina Cauda. She gave me the opportunity to work in her laboratory during these three years of PhD, investing time and support in me and always showing me the right path to follow in the difficulties of research, always with patience and enthusiasm.

Big, great thanks to all the people who have been part of the TNH lab. To Luisa, Bianca and Marta who helped me in every kind of situation in the lab (I believe that the sentence “ask Luisa, Bianca or Marta” saved me in solving more than half of my problems in the lab); to Marzia, Giada, Nicolò, Federica, Giulia and Maria Cristina, thanks to whom I am really happy to come to the lab, for showing me new approaches and contributing to who I am as a researcher, and to all the thesis students who went through our lab. A very special thank goes to Veronica, who is the company I needed during this journey: it would have not been possible to make to the end without knowing I have a friend in my office.

Finally, I would like to thank Marco Laurenti, which was my first mentor and from whom I hope to have learnt at least a bit of his passion and ability as a researcher, Simelys Hernandez, Nadia Garino and Giancarlo Canavese, for their precious advice in the many fields I needed help with.

# Abstract

The research in nanomedicine is focusing considerable attention on smart nanoparticles thanks to their multifunctional properties which gather their use in several fields like imaging, therapy or a combination of the two, i.e. theranostics. Among the various nanomaterials, zinc oxide nanoparticles (ZnO NPs) present physical and chemical properties which could fulfill the requirements for an efficient nanotheranostic system, like antimicrobial, photocatalytic, semiconducting and piezoelectric properties. However, pure ZnO NPs also suffer from poor stability in biological media and consequent possible cytotoxic effects. This important limitation to their use could be overcome by doping, i.e. the inclusion of a new element inside the ZnO crystalline structure. Depending on the doping element, the already interesting properties of ZnO NPs could be further enhanced or new properties introduced. For example, the safety of the NPs could be improved, as well as its piezoelectric properties, while novel magnetic responsiveness can be induced.

The aim of the PhD thesis here presented is to explore the potentialities of newly synthetized iron doped ZnO NPs (Fe:ZnO NPs) in the field of nanomedicine to treat pancreatic cancer. Iron doping, in particular, was chosen as it can lead to magnetic responsiveness and enhanced safety to the ZnO NPs. Fe:ZnO NPs were synthetized by means of a simple, fast and cheap wet chemical method that lead to nano-sized spherical particles. The NPs surface was functionalized during the synthesis with a capping agent, oleic acid, aimed at increasing the colloidal stability.

A further amino-propyl functionalization was performed after NPs formation to provide functional groups exploited for dye labelling, useful in cell cultures. Then, a complete physical and chemical characterization of the Fe:ZnO NPs was fulfilled, and the Fe:ZnO NPs were compared to pure ZnO NPs. The doping was confirmed through X-ray diffraction, electron microscopy, energy dispersive spectroscopy and X-ray photoemission spectroscopy, while the success of the two functionalizations was verified by Fourier-transform infrared spectroscopy. Finally, the colloidal stability and surface charge were established through Dynamic Light Scattering and Z-potential measurements, respectively. The novel features gathered by doping were also investigated. The optical behavior of the NPs was analyzed, searching for new energy states that could suggest interesting applications for medical imaging. From the therapeutic standpoint, the electromechanical response of Fe:ZnO NPs was studied and compared to ZnO NPs, finding an enhanced response for the doped NPs. However, the most interesting result was found in terms of magnetic responsiveness. In this sense, Fe:ZnO NPs acquire, thanks to doping, a considerably enhanced magnetic responsiveness that could be efficiently used in magnetic resonance imaging.

To have a first proof-of-concept application of the fabricated nanoparticles, Fe:ZnO NPs were tested on a pancreatic adenocarcinoma cell line as a sonosensitizing agent. The idea leading the research was to couple Fe:ZnO NPs with shock waves, i.e. high pressure waves, that can be remotely provided to cancer cells to kill them once they have internalized Fe:ZnO NPs. In this view, a safe dose of Fe:ZnO NPs is administered to cells and a harmless dose of shock waves is provided to the cancerous tissue. The damages to the diseased tissues are obtained only when the two treatments are combined, providing a strong control on the cell death and reducing, in turn, the risks of collateral effects. To perform this task, the cytotoxicity of the NPs on cancer cells was evaluated and compared to the toxicity of the same particles on non-cancerous cells. Then, the Fe:ZnO NPs internalization

was measured and analyzed with fluorescence microscopy and cytofluorimetry to determine the best treatment conditions. With these optimized parameters, Fe:ZnO NPs and shock waves were administered together to the cells, finding an enhanced toxicity only when the two treatments are combined and proving the efficacy of the nanotheranostic agent. Finally, the cell death mechanism was analyzed through fluorescence microscopy analyses and kinetics cell death analyses to provide further insight on the whole system, in view of further tests in vivo.

The results presented in this PhD thesis consider the fabrication of a multifunctional Fe:ZnO NPs based system from its design up to its application in vitro. The main goal is to prove the effectiveness of this nanoplatform in a proof-of-concept application and to open to the exploitation of the system as a nanotheranostic device in several fields of the fight against cancer. The final results suggest the use of the nanoconstruct in further tests in vivo, before the hopeful application of them in clinical tests.

# Contents

# List of Figures

# List of Tables

# Chapter 1

# Introduction to doped ZnO nanoparticles in biomedicine

Part of this chapter has been taken from the open-access publication "Carofiglio, M.; Barui, S.; Cauda, V.; Laurenti, M. *Doped Zinc Oxide Nanoparticles: Synthesis, Characterization and Potential Use in Nanomedicine*. Appl. Sci. 2020, 10, 5194"[1].

## 1.1 Introduction

Nanomedicine is an emerging branch of science dealing with the use of smart materials for medical applications. Some practical examples include new generation functional materials for physical therapy (hyperthermia, photodynamics and sonodynamics) and advanced drug delivery systems, but also for tissue engineering, contrast agents and in vivo imaging.

The integration of smart materials with nanomedicine is challenging as it poses a severe limitation about the corresponding size, which must be comparable to that characterizing most of the biological systems. For this purpose, nanomaterials are the most promising candidates to meet such requirements as the average size lies at the nanometer scale. Moreover, the medical technologies resulting from the use of nanomaterials benefit from this reduced size, as they are considered to be less invasive and possibly implantable in the body. Another advantage is that the physical–chemical properties of nanomaterials can be easily tuned with various methods so that unprecedented functionalities with respect to the bare material can

be provided. In this sense, nanomaterials for nanomedicine are conceived as smart, i.e., materials designed for the exploitation of specific functions, even remotely controlled and activated by an external stimulus[2]. This specific function can thus be exploited after the injection of the nanomaterial in the human body and only once the site of interest has been reached.

Among nanomedicine applications, the efficacy of nanoparticles-based drug delivery systems has been largely demonstrated[3,4]. With respect to the standard methods, the use of nanoparticles with a high surface area as drug carriers has highly improved the encapsulation efficiency of drugs and a more targeted delivery of the drug to the site of interest is foreseen. Moreover, drug delivery systems based on the use of nanoparticles also show improved pharmacokinetics and biodistribution of the drug[3]. Complex delivery mechanisms have been developed to achieve the controlled release of the drug, including pH-triggered release systems[5] or are driven by an external activation with light/mechanical stimulation [6,7]. In some cases, nanoparticles have been also investigated as nanoantibiotics due to their promising antimicrobial activity[8] and high potential in fighting antibiotic resistance[9]. More recently, nanoparticles started to be studied on their own as new generation nanodrugs for anticancer therapy[10]. Actually, the conventional treatments based on chemotherapy show several limitations: for example, the lack of selectivity and solubility of the chemotherapeutic agents, which induced undesirable side effects[11]. On the other side, the successful treatment of cancer cells by using nanoparticles can benefit from the following aspects: (i) the high surface area to volume ratio and (ii) the rich surface chemistry, both of which allow the anchoring of specific functional groups and make the functionalized nanoparticles more selective toward selected tumor cells[12,13]; (iii) the reduced size (5–100 nm), allowing their preferential accumulation at tumor sites that lack an effective lymphatic drainage system[14–17]; (iv) a spontaneous biodegradation into non-toxic reaction products, thus avoiding the accumulation of toxic elements in the body once the therapeutic action has been completed[18,19].

Nanoparticles with improved functionalities have been developed for in vivo imaging as well[20]. The reduction of the particle size down to the nanometer scale results in quantum confinement effects such as size-tunable light emission properties (quantum dots, QDs). In this sense, nanoparticles can be used as contrast agents with improved imaging properties. For example, fluorescent nanoparticles based on semiconducting QDs, or polymeric or metallic nanoparticles have been developed to achieve higher contrast imaging than using standard molecular fluorophores[21,22]. Magnetic nanoparticles have also been combined with the

magnetic resonance imaging (MRI) technique and used as contrast agents for tumor visualization[23]. Metallic nanoparticles have been successfully tested as contrast agents for optical or X-ray imaging and allowed for the detection of atherosclerotic plaques, intravascular thrombus, or fibrotic tissue[24].

More recently, theranostic nanoparticles have captured considerable attention as well[25]. Theranostics deals with the development of multifunctional platforms able to perform diagnostics and therapy at the same time, also with the aid of nanoparticles and nanotechnologies (nanotheranostics). Some materials are characterized by the coexistence of specific physical and chemical properties, such as the optical, magnetic or catalytic properties, so that both the imaging and therapeutic effects are combined together within the same nanoparticles. Within this scenario, it is thus possible to prepare nanosized materials able to be injected in the human body, reach the specific target organ and release the therapeutic agent, but also be directly monitored and visualized in the target site. As an example, Au nanoparticles (NPs) have been demonstrated to serve as extremely versatile theranostic nanovectors since they act as an imaging probe and as the therapeutic agent for hyperthermia at the same time[26–28]. Another successful approach involves the use of magnetic nanoparticles (MNPs)[29–31] or the combination of MNPs (acting as contrast agents) with mesoporous silica nanoparticles with high surface areas to maximize the drug loading efficiency of the overall theranostic system and allow for a stimuli-responsive release of the therapeutic payload[32,33]. Other techniques currently being investigated involve photothermal, photodynamic or sonodynamic therapy in combination with other imaging tools such as optical imaging, magnetic resonance imaging and ultrasound imaging[34–37].

Nanomaterials have also been successfully applied in tissue engineering (TE) as tools able to promote the repair of damaged tissues and organs[38]. Similar to the other nanomedicine applications previously mentioned, the advantage of using nanoparticles in TE derives from their small size and large surface to volume ratio. Among others, these features allow for an easy surface functionalization of the particles with peptides, ligands or proteins, their easy diffusion across membranes and facilitated cellular uptake. Moreover, nanoparticles can show superior biocompatible properties in some cases, while the nanoparticles' size resembles the nanometric scale of components present in the extracellular matrix of tissues. Carbon-based nanomaterials, as well as metal oxide- and silica-based nanoparticles, have been used either alone or else in combination with other polymeric materials for the fabrication of smart composite scaffolds with improved functionalities in terms of their biological, electrical and mechanical properties[39–42]. The use of

metal/metal oxide nanoparticles also led to very promising antibacterial activity, thus regulating bacterial infections often present after surgery to remove/replace organs and tissues[43]. In other cases, the use of ceramic and metal oxide nanoparticles allowed for the induction of the remotely-controlled mechanotransduction of cells, with evident effects on cells proliferation and tissue regeneration rates[44,45]. The use of magnetic nanoparticles for remote cell patterning was also successfully demonstrated[46].

As expected, a plethora of nanomaterials, both of organic and inorganic derivation, have been successfully explored as smart functional materials in nanomedicine. In the specific case of ceramic materials and metal oxides, some examples include: mesoporous silica nanoparticles as nanocarriers in drug delivery systems[47,48] and as bioactive agents for bone tissue engineering[49]; cerium oxide nanoparticles featuring antibacterial and antioxidant therapeutic properties[50–52]; magnetic iron oxide nanoparticles, which were successfully proposed as theranostic nanovectors coupling therapeutic effects against cancer cells through hyperthermia with MRI contrast agent properties[53–55].

More recently, the use of zinc oxide (ZnO) in nanomedicine captured considerable attention[56]. ZnO is a low-cost, abundant material, classified as a generally recognized as safe (GRAS) material from the Food and Drug Administration[57], which makes it suitable for a plethora of biomedical applications. Moreover, ZnO is a wide band-gap semiconductor (3.37 eV) featuring peculiar physical and chemical properties, such as photo- and sono-catalytic activities[58–60], piezoelectricity[61,62] and pyroelectric[63] behaviors. The abovementioned properties can be combined together and even strengthened by selecting, among the numerous ZnO morphologies, the most appropriate one: thin films[64,65], nanowires (NWs)[66], nanorods (NRs)[67], nanobelts[68], nanoparticles (NPs)[69] and flower-like structures[70] can be easily synthesized by wet and dry preparation approaches such as sol-gel and hydrothermal routes, and vapor-phase deposition techniques.

Various ZnO nanomaterials have been successfully applied in TE[71]. ZnO NWs[72], NRs[73] and nanoflowers[74] have been found to promote the adhesion, growth, and differentiation of several cell lines. ZnO NPs can be easily addressed in the human body due to their reduced size, which also facilitates cellular uptake[75]. Therefore, the promising osteogenic and angiogenic properties of ZnO NPs have been demonstrated, along with their use as nanotherapeutic agents to fight bacterial infections[76,77]. In this sense, ZnO NPs are defined as nanoantibiotics due to their promising antimicrobial properties against both Gram-positive and Gram-negative bacteria.

ZnO nanomaterials as targeted drug delivery systems have been reported as well[78–80]. ZnO QDs (2–10 nm) were combined with doxorubicin-loaded MSNs and used as nanolids to cover silica nanopores and achieve a sustained and pH-triggered delivery of the anticancer drug[81]. Other works include the use of mesoporous ZnO nanospheres[82], dandelion-like mesoporous ZnO capsules[83] and porous hexagonal ZnO nanodisc structures[84]. In the latter cases, the targeted and pH-triggered delivery of chemotherapeutic agents against cancer cells was effectively demonstrated. ZnO nanoparticles have been also used as imaging agents[80] for cell labeling[85], tumor targeting[86] and diagnostics[87]. ZnO NPs can also serve as a nanodrug to treat cancer cells[69,88,89]. The therapeutic effect is accomplished by the release of harmful species ($Zn^{2+}$ cations and reactive oxygen species, ROS) upon interaction of ZnO with aqueous media[90–92]. The therapeutic efficacy of ZnO NPs against different cancer cell lines was confirmed in vitro. In some cases, the remote activation of ZnO NPs cytotoxicity has also been obtained. It is the case of photodynamic[93] and sonodynamic[90,94] therapeutic approaches, an external stimulus (a light or mechanical one) was able to activate the cytotoxic effect of the nanotherapeutic drug, i.e., the ZnO NPs themselves, which could generate a harmful ROS or mechanical damage to cancer cells.

Despite the promising results, the use of ZnO nanomaterials in nanomedicine is still limited because of some intrinsic limitations such as a low stability of the ZnO particles in biological fluids and the non-controllable release of $Zn^{2+}$ cytotoxic species[95,96]. Hence, additional efforts are required to make ZnO more attractive. For this purpose, the doping of ZnO served as a powerful approach to confer on ZnO new functionalities rather than to improve pre-existing ones. The various physical and chemical properties of ZnO NPs have been properly customized for a specific function by inserting ad-hoc chemical elements (dopants) into the ZnO crystalline structure. For example, the optical[97], electrical[98], electromechanical[99] and catalytic[59] properties could be optimized and strengthened after doping ZnO with appropriate elements. In other cases, doped ZnO nanomaterials showed unprecedented properties with respect to the pure material counterpart[100]. Therefore, ZnO doping represents an intriguing solution to overcome some of the abovementioned limitations and, to a further extent, a way to use ZnO NPs in nanomedicine.

## 1.2 Aim of the thesis

This thesis aims at exploring the potentialities of doped ZnO NPs in the field of nanomedicine as a way to treat pancreatic cancer. More in detail, iron doped ZnO NPs (Fe:ZnO NPs) were chosen for particular features gathered by iron doping, like magnetic responsiveness and enhanced safety of the NPs.

This Thesis works is structured in three chapters presenting diverse aspects of the Fe:ZnO NPs. A first chapter is focused on the literature panorama related to doping of ZnO NPs exploited as biomedicine tools. This Chapter (based on the work Carofiglio, M.; Barui, S.; Cauda, V.; Laurenti, M. Doped Zinc Oxide Nanoparticles: Synthesis, Characterization and Potential Use in Nanomedicine. Appl. Sci. 2020, 10, 5194)[1] covers the more recent achievements in the strategies adopted to dope ZnO NPs, the acquired new properties or the enhanced features and final their applications in nanomedicine. The first section summarizes the most diffuse elements for doping ZnO nanoparticles. Then, a general overview of the main synthetic approaches used to prepare doped ZnO NPs is provided. Finally, the main applications of doped ZnO NPs in nanomedicine are reviewed, with a particular focus on their use as antimicrobial agents, contrast agents for bio imaging applications and as therapeutics against cancer. From this literature study, the choice on the doping element fell on iron, which presents interesting features which could be extremely useful for biomedical applications.

The second chapter focuses on the synthesis of the Fe:ZnO NPs and their characterization. This work is the object of another publication (Carofiglio, M.; Laurenti, M.; Vighetto, V.; Racca, L.; Barui, S.; Garino, N.; Gerbaldo, R.; Laviano, F.; Cauda, V. Iron-Doped ZnO Nanoparticles as Multifunctional Nanoplatforms for Theranostics. Nanomaterials 2021, 11, 2628.)[101]. The aim of the chapter herein proposed is to develop multifunctional iron-doped ZnO nanoparticles (Fe:ZnO NPs) thought as theranostic nanoplatforms that can be introduced safely inside the cell and that present intrinsic imaging and therapeutic potentialities to fight different types of cancer cells.

Finally, the third chapter explores an example of application of the Fe:ZnO NPs. Their effectiveness as sonosensitizing agent is proved, demonstrating the reduced pancreatic cancer viability in vitro when The Fe:ZnO NPs are coupled with a remote mechanical stimulation, i.e. shock waves. Fe:ZnO NPs are thus tested first in terms of their cytocompatibility, cellular uptake and NPs dissolution in cell

culture media in comparison to undoped ZnO NPs. The obtained results aim to increase the understanding of the Fe:ZnO NPs fate inside the cell, when their administration is not coupled with a remote physical stimulation, and to evaluate the final and safe biodegradation. The coupling of the NPs with a mechanical stimulation, i.e. pressure shock waves, is exploited to induce cell death only on demand, to achieve a remotely-controlled and safe therapy. Therefore, BxPC-3 viability is assessed with the coupled treatment and then the cell fate is observed to determine the cell death mechanism and other possible aspects that could be improved in view of a future clinical translation.

## 1.3 Materials for Doping ZnO Nanoparticles (NPs)

Zinc oxide (ZnO) is an inorganic material that has been successfully applied in numerous fields, ranging from gas sensing[102] and energy harvesting[103–105] to biomedicine[71,106], to name only a few. In addition to the properties mentioned above, it may be useful to add further functionalities to ZnO rather than to improve the pre-existing ones, with the final aim to design a multifunctional system.

For this purpose, doping represents a valuable approach to tune various ZnO properties. Doping consists of the insertion of a specific ion into a crystal lattice, not originally present in the starting material. It can be particularly useful to modulate the energy band-gap, with a direct consequence on the ZnO photocatalytic properties and related antimicrobial activity. Moreover, the insertion of selected elements in the ZnO lattice allows for the generation of a weak ferromagnetic behavior in the doped particle[107–109], the tuning of the degradation properties in aqueous environments[59,110], or even the modulation of the electromechanical response[99,100]. All these aspects, summarized schematically in Figure 1, may be exploited in nanomedicine to design a multifunctional theranostic nanoplatform able to perform both diagnoses (for example, through magnetic resonance imaging) and therapy (such as photodynamic therapy or enhanced reactive oxygen species generation) at the same time.

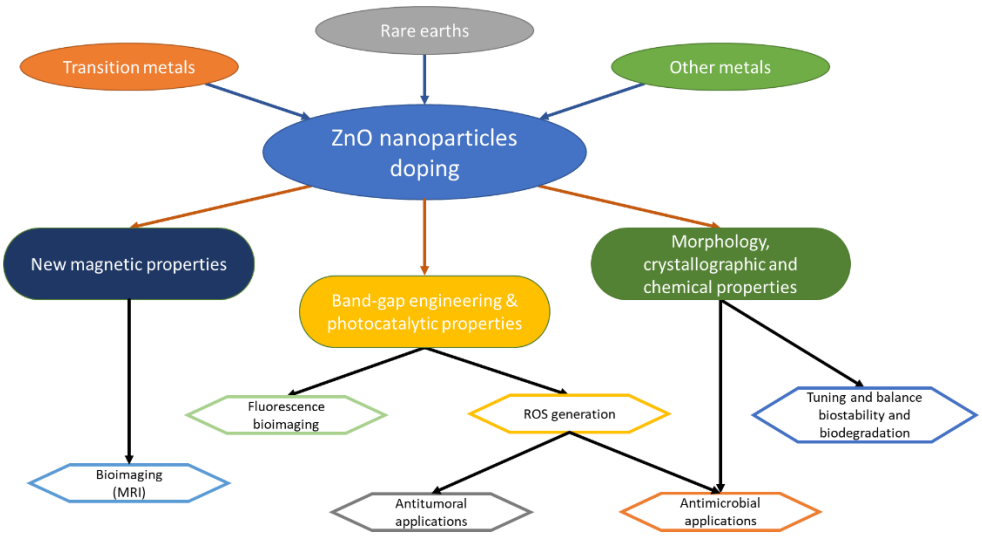


Figure 1: Main applications of doped ZnO nanoparticles in nanomedicine.

The physical and chemical properties of doped ZnO are strongly dependent on the doping element. Actually, several aspects, such as the ions' dimensions, the electronegativity, the coordination state etc., all contribute to determine the final properties of the doped material[111]. For these reasons, the use of ad-hoc dopants must be foreseen on the basis of the expected new functionality. In the following, the most used ions reported in literature are briefly presented, and their effects, due to their inclusion in the wurtzite ZnO crystal lattice, are summarized.

### 1.3.1 Rare Earth (RE) Elements

Rare earth (RE), or lanthanide, elements are widely exploited for the doping ZnO nanomaterials and to properly modify the corresponding electronic band structure[112]. As highlighted in the work of Cerrato et al.[113], upon UV light irradiation, ZnO presents a very fast recombination of the photogenerated charge carriers. This results in a low quantum efficiency when this system is used as a photocatalyst. The use of lanthanide, due to the 4f configuration, may help in increasing the recombination time of the electron/hole pair in the semiconductor[113], resulting in a higher efficiency of the system in the photocatalytic process, with consequences on the antimicrobial activity. Cerium, for example, has been proven to enhance the photocatalytic properties of ZnO nanorods through this mechanism[114], exceeding the performance of titanium dioxide ($TiO_2$), which is the material typically exploited as a reference for these purposes.

The change in the band-gap and the generation of trap states make RE doping interesting; also, from the luminescence point-of-view, this increases the possibility of ZnO being used as an imaging agent. The trap states induced by doping may act as radiative recombination sites not present in the pure crystal and the dopant atoms and, together with aspects such as the crystallite size, contribute to change the band-gap of the system, resulting in the possibility to tune the optical properties of ZnO. In the work of Kumar et al.[115], it is pointed out that ZnO may have improved luminescence properties from RE doping because of the transitions with the 4f orbitals of the RE elements in the crystal lattice. For example, Zhao et al.[116], synthesized an array of terbium-doped ZnO nanotubes which showed three emission bands in the range of visible light (543 nm, 586 nm and 620 nm, as clearly visible in Figure 2a) due to terbium doping. In particular, it was also demonstrated that the 586 nm band was due to the energy transfer between ZnO and $Tb^{3+}$ ions obtained through the electron transitions depicted in Figure 2b.

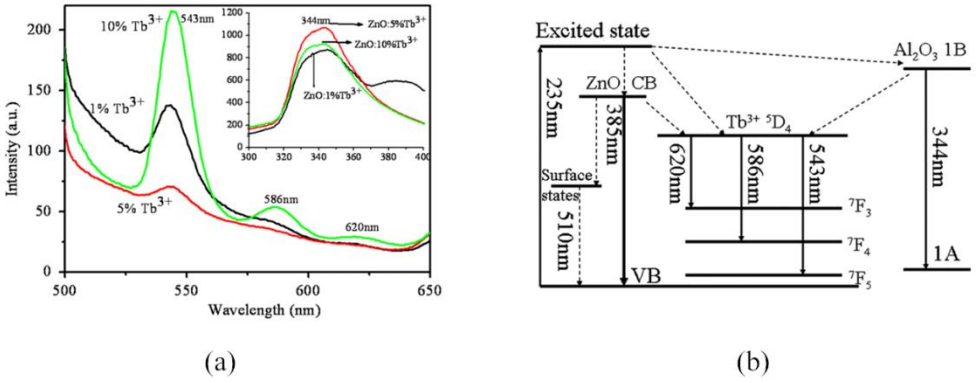


Figure 2: Photoluminescence properties of Tb-doped ZnO nanotubes. (a) Emission spectra of ZnO with different dopant levels excited by a 235 nm radiation; (b) energy-levels schematic with the electron transition processes in Tb-doped ZnO nanotubes grown onto alumina. Adapted from[116].

Doping with RE materials is also a valuable method to change the piezoelectric behavior of ZnO. Indeed, the introduction of defects into the crystal further enhances the asymmetry of the wurtzite crystalline structure responsible for ZnO piezoelectricity. For example the generation of a ferroelectric behavior in lanthanum-doped ZnO was reported, alongside an increase of the piezoelectric coefficient $d_{33}$ by one order of magnitude (≈101.30 pm/V for La-doped ZnO (mean value) vs. the accepted value of 12.4 pm/V for bulk ZnO[117]). The reason for this behavior was attributed to the large ionic radius of the dopant element (1.22 Å) with

respect to zinc's radius (0.74 Å), which induced a stronger distortion of the crystal cell and the rise of a stronger spontaneous polarization[118].

It is worth noting that, despite transition metals dopants being the best choice to induce room temperature (RT) ferromagnetism in ZnO, gadolinium, an RE element, has been proven to successfully induce a magnetic behavior in ZnO nanoparticles[119,120]. In particular, RT ferromagnetism was observed for a film made of Gd:ZnO nanoparticles, doped by low energy ion implantation method. The authors found that a thermal annealing at 650 °C was able to favor the diffusion of the dopant atoms into the ZnO lattice. The as-prepared ZnO:Gd film showed a RT ferromagnetism and the formation of some super-paramagnetic clusters[121]. The reason of this behavior is still under debate and the use of RE doping elements in general, and gadolinium in particular, is to induce magnetism in ZnO nanoparticles, which is reported by few works. On the contrary, most of the research on magnetic ZnO nanoparticles is focused on the use of transition metals, as discussed in the next section.

In conclusion, RE elements have been more extensively studied to increase the photocatalytic and optical properties of ZnO nanomaterials, but also to confer on ZnO magnetism and improved electromechanical properties in some cases.

### 1.3.2 Transition Metals (TM) Elements

Another class of elements that have been widely exploited as doping agents for ZnO are the transition metals. Elements such as cobalt (Co)[122], chromium (Cr)[123], iron (Fe)[124], manganese (Mn)[125] and copper (Cu)[126] have all been successfully used to enhance pre-existing properties or to give new features to ZnO, making it interesting also from the nanomedicine point of view.

The research on TM-doped ZnO gained lots of attention because of the ability of this material to work as a diluted magnetic semiconductor (DMS). DMSs are semiconducting materials that also present a ferromagnetic behavior because of the presence of transition metal (TM) ions that are ferromagnetic in their pure form, such as Mn and Fe. Despite such behaviors being still under debate[127], numerous works have reported the observation of RT ferromagnetism in TM-doped ZnO nanomaterials.

As in the case of RE elements, doping with TMs does not only contribute to the ferromagnetic behavior of ZnO: both the optical[128] and electrical[129] properties can be tuned by these materials and are heavily affected by several parameters such as the oxidation state, ionic radius, electronegativity and other features of the doping ion[111].

Among TM dopants, iron is one of the most used. This element can exist into two different oxidation states ($Fe^{2+}$ and $Fe^{3+}$). They both induce a different effect on both the electrical and structural properties, due to the different ionic radius and charge carried in the system. The studies on Fe-doped ZnO are mainly focused on the analysis of the corresponding magnetic properties. However, some works also showed that Fe doping represents an effective approach to improve the chemical stability of ZnO nanoparticles in aqueous media[130] or to enhance the electromechanical response[131]. As an example of such a study, in the work of Srinivasulu et al.[132], an increasing ferromagnetic behavior at room temperature is reported with the increase of iron doping in ZnO thin films. Additionally, another work shows that the ferromagnetic behavior of Fe-doped polycrystalline ZnO powders is influenced by the post-synthesis annealing conditions[133]. In particular, the ferromagnetic response was optimized by means of an annealing in a hydrogen atmosphere, while an argon atmosphere annealing would not produce any ferromagnetic behavior. Still, the reason for the rising of such a behavior is not clear and controversial explanations are currently reported in the literature. In terms of the piezoelectric properties of Fe-doped ZnO, the work of Luo et al.[131] focuses the attention on the chemical state of Fe ions introduced in the ZnO crystal. According to this work, the oxidation state of the dopant ion plays a fundamental role in determining the electromechanical response of the doped ZnO films because of the different ionic radius; a smaller ion ($Fe^{3+}$) leads to a higher piezoelectric coefficient (~128 pC/N vs. 9 pC/N for 1.2 at.% Fe doping) than doping with a larger one ($Fe^{2+}$).

Manganese has been also extensively used as a dopant agent. Mn is characterized by several oxidation states with a higher difficulty in controlling this parameter. In addition, in this case, the dopant agent is used to modify the optical, structural and magnetic properties of the resulting ZnO semiconductor[120]. The ferromagnetic behavior of Mn-doped ZnO was found to be dependent on the doping amount but without a linear relationship between the two parameters[125]. Another work pointed out that the behavior of Mn-doped ZnO was diamagnetic at 1 at.% of doping and ferromagnetic at 5 at.%[128]. Additionally, the piezoelectric response of Mn-doped ZnO nanoparticles was found to be heavily dependent on the amount of Mn ions introduced in the ZnO crystal but not in a linear way. In the work of Pan et al.[111], the $d_{33}$ piezoelectric coefficient is found to first decrease with the increase of Mn doping up to 4.8 at.% and then it increased with further Mn doping. This behavior is attributed to the change in the oxidation state of Mn ions because of the use of different doping amounts. A different Mn oxidation state means a different

ionic radius and hence, a change in the resistance against the rotation of the oxygen–metal bonds in the ZnO lattice.

Among the TM dopants, the use of copper is reported as a tool to increase the antimicrobial activity of ZnO. Hassan et al. successfully demonstrated the fabrication of Cu-doped ZnO coatings with enhanced antimicrobial activity against *E.Coli* under light illumination[126]. The higher performance obtained by Cu doping was attributed to an enhanced reactive oxygen species (ROS) generation and the release of cytotoxic zinc and copper ions.

Other works also showed the use of chromium and cobalt ions as doping agents for ZnO. Chromium-doped ZnO nanoparticle films were prepared by reactive magnetron co-sputtering. The incorporation of Cr ions within the ZnO crystal lattice resulted into the rise of ferroelectric properties and it notably improved the piezoelectric response with respect to the pure ZnO films[123]. This induced ferroelectric behavior was attributed to the substitution of some of the $Zn^{2+}$ ions by smaller $Cr^{3+}$ ions, which generates a permanent electric dipole. On the other side, cobalt doping was found to increase the band-gap of ZnO, making it transparent to most of the visible light. Additionally, for this doping element, a room temperature ferromagnetic behavior could be observed in Co-doped ZnO nanoparticles[134].

Noble metals, such as gold and silver, were used in different applications as well. For example, the photoluminescence properties of Au-doped ZnO nanoparticles were investigated[135]. The results showed the presence of additional weak luminescence peaks in the visible spectral range the intensity of which was dependent on the doping amount. Gold and silver doping were also investigated as potential antimicrobial boosters for ZnO[136]. In this work, both Ag and Au ions were found to be suitable for increasing the photocatalytic properties of ZnO. However, Au was not able to improve in a significant way the antibacterial activity of ZnO, while Ag-doped ZnO nanoparticles showed enhanced antifungal activity. In another work, the antibacterial activity of Ag-doped ZnO nanoflowers, obtained by means of a green combustion method, was evaluated. The results highlighted a good antimicrobial activity against both Gram-positive and Gram-negative bacteria, as well as an antifungal efficacy against different plant pathogenic fungal strains[137].

In summary, many TMs have been studied for doping ZnO mainly because of their ability to give ferromagnetic properties to ZnO but also to improve its electrical and optical behavior. In the particular case of nanomedicine, doping ZnO with TMs could represent a valuable tool for the design of new multifunctional ZnO nanomaterials with newly acquired bioimaging features, i.e., magnetic resonance imaging.

### 1.3.3 Other elements

Apart from RE and TM elements, other elements have also been exploited as dopant atoms. For example, aluminum has been used mainly for the fabrication of flexible detectors. For example, a stretchable $NO_2$ gas sensor was developed by allowing the diffusion of Al ions in an array of vertically aligned ZnO nanorods[138]. A flexible pH sensor based on Al-doped ZnO nanosheets was also obtained. Due to Al doping, the sensitivity of the device was highly improved (50.2 mV/pH) with respect to the pure ZnO nanosheets (34.13 mV/pH)[139].

Magnesium is another common choice for ZnO doping and it was used mainly for improving the optical and electromechanical properties with respect to pure ZnO. As in the case of gold, Mg doping was found to increase the photoluminescence properties of ZnO in the visible spectrum of light[140]. In the same work, the photocatalytic degradation of rhodamine B was proven to be enhanced by Mg doping. Moreover, an enhanced antibacterial activity was also obtained, which was correlated to a lower band-gap and the resulting enhanced photocatalytic activity with respect to pure ZnO. From the electromechanical point of view, in a work from Chen et al., the piezoelectric coefficient of $Mg_xZn_{(1-x)}O$ appeared to be increased ($d_{33}$ = 54.1 pm/V) by increasing the amount of Mg up to x = 0.28[141]. After this point, which was found to be the limit for not observing the formation of any secondary phase in the crystalline structure of ZnO, the authors found that the $d_{33}$ coefficient abruptly reduced values below the pure ZnO one.

Nitrogen-doped ZnO nanowires, further coated by a thin layer of titania to form a core–shell structure, were also proposed[142]. After the thermal annealing of ZnO nanowires in a nitrogen atmosphere, the nanomaterials showed a higher absorption of UV and visible light than the corresponding air-annealed samples, due to slightly lower values obtained for the band-gap. Ultimately, the one-dimensional ZnO-$TiO_2$ core-shell nanostructures were proposed for photoelectrochemical water splitting, showing enhanced efficiencies under solar light illumination.

Actually, the choice in terms of dopants is very wide, as witnessed by a few other works reporting the use of other elements such as chlorine[143], antimony[144], fluorine[145], lithium[146] and many others, each of which changes specific properties of pure ZnO that may be suitable for a specific application.

## 1.4 Synthesis Methods and Characterization

As already mentioned, one of the main advantages in using ZnO is the availability of a plethora of morphologies which can be easily prepared by various methods[12]. Figure 3 shows the electron microscopy images of microparticles with a very high specific area and various morphologies, such as a flower-like shape[70,147], multipods[148,149], nanorods[150], films with a nanostructured surface[78] and nanoparticles[77] of different shapes and dimensions, all of them well established and reported in the literature. Moreover, the methods through which these particles are obtained are even larger in number than the morphologies themselves. Therefore, it is difficult to make a comprehensive overview of all the possibilities that are already present. By considering the specific subject of this chapter, the most rapid low-cost and high-yield methods for preparing doped ZnO nanoparticles are discussed.

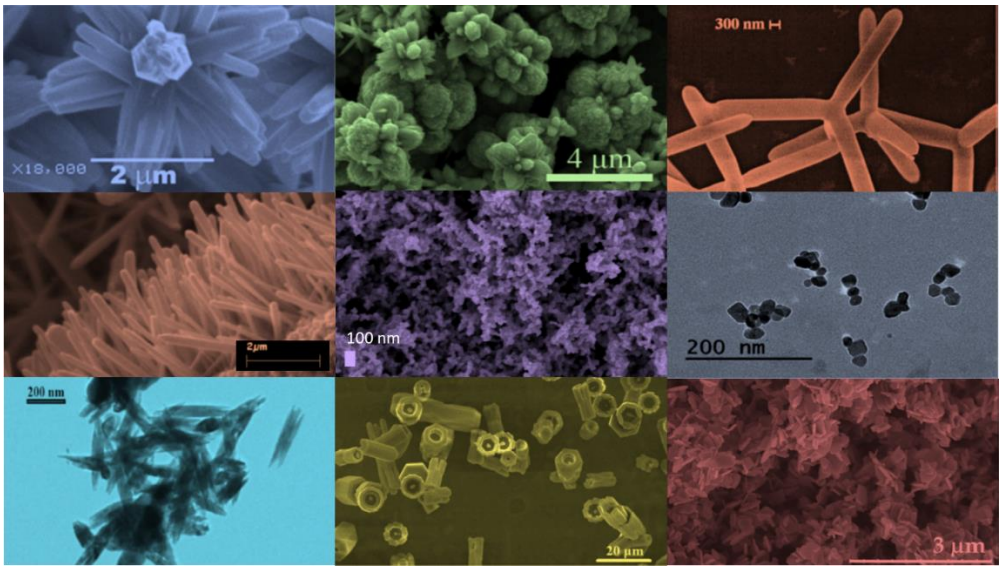


Figure 3: Possible morphologies of ZnO nanostructured systems. From left to right and from top to bottom: nanoflowers (adapted from ref.[151]), nanopods (adapted from ref.[149]), nanorods (adapted from ref.[150]), mesoporous films, spherical nanoparticles, nanoneedles (adapted from ref.[152]), hollow microcolumns (adapted from ref.[153]), and micropods (adapted from ref.[154]).

In the following, wet chemical methods are first presented. This category is probably the most diffuse one, due to the excellent trade-off between the quality of

produced materials, versatility and poor requirement in terms of instrumentation, and, in particular, for doping ZnO with rare earth elements. Then, other methods, such as flame spray pyrolysis[130], sputtering[155] or pulsed laser deposition[156], are described as being widely used for the preparation of both doped ZnO films and nanoparticles.

### 1.4.1 Wet Chemical Methods

Wet chemical methods are among the most promising techniques adopted to synthesize micro- and nanostructured materials. Among the main advantages are the use of non-toxic solvents, low synthesis temperatures, and the use of simple equipment. Moreover, due to the relatively good purity and stoichiometry of the resulting material, wet chemical methods appear to be a promising choice for the development of doped ZnO nanoparticles.

A typical sol-gel/hydrothermal method to prepare ZnO-based materials is based on the following reactions[70]:

$$Zn^{2+} + 2OH^- \rightarrow Zn(OH)_2, \quad (1)$$

$$Zn(OH)_2 + 2OH^- \rightarrow Zn(OH)^{2-}_4, \quad (2)$$

$$Zn(OH)^{2-}_4 \rightarrow ZnO + H_2O + 2OH^- \quad (3)$$

Typically, this process is assisted by a mineralizing agent that provides the $OH^-$ groups necessary to tune the pH of the solution, avoiding the precipitation of zinc hydroxide and promoting the formation of ZnO. Typical choices are NaOH[147], KOH[70] and, less often, $NH_4OH$[157].

Among the zinc precursors, the main used are zinc acetate[158,159], zinc nitrate[160,161] and zinc chloride[152,162,163], which readily dissolve in most of the solvents used in this kind of reaction (water[154,164], ethanol[165] and methanol[166]). For the dopant precursor, chlorides[140], nitrates[167,168] and acetates[146] from the corresponding dopant elements are the typical choices. Then, the inclusion of the dopant can be obtained in a practically straightforward way, by mixing the dopant ion solution together with the zinc precursor solution, before mixing with the base.

Another challenging aspect is the design of particles with an appropriate morphology. Indeed, it play an important role in determining the NPs biological behavior, influencing factors such as cell internalization. The morphology and the dimension of the nanoparticles can be controlled through surfactants such as sodium dodecyl sulphate[169] or cetyltrimethylammonium bromide[170]. Moreover, the use of different surfactants in different amounts has been demonstrated to completely

change the final morphology of the particles, leading to very peculiar shapes such as nanoflowers, nanomultipods or even nanopyramids[171].

The sol-gel approach is widely used when doping ZnO with rare earth elements is pursued.

Goel et al. reported the synthesis of Gd-doped ZnO nanorods by means of a wet chemical solution route that involved zinc chloride and gadolinium (III) chloride hydrate dissolved in distilled water[163]. The salt solution was prepared to have $Gd^{3+}$ at a 5 mol.% concentration with respect to ZnO, and it was mixed dropwise to a sodium hydroxide (NaOH) solution in order to get powder precipitation. By TEM and XRD analyses, the authors found useful information about the structural changes occurring in the ZnO wurtzite crystalline structure: after the correct insertion of Gd dopant, there was no other secondary phase in the resulting material. An increase of the unit cell parameters for Gd-doped ZnO (a = 3.2524 Å, c = 5.2095 Å and V = 47.73 Å3) was found with respect to the pure ZnO nanorods (a = 3.2518 Å, c = 5.2095 Å and V = 47.70 Å3), as expected from the larger ionic radius of $Gd^{3+}$ (0.94 Å), with replacement taking place at the $Zn^{2+}$ sites in the host ZnO lattice, which is able to modify the dimensions of the crystal unit cell. This distortion of the crystalline cell leads to an enhancement of the piezoelectric coefficient, which changed from 12.4 pm/V of pure ZnO[117] to 45.49 pm/V for the Gd-doped nanoparticles (maximum value). A change in the unit cell parameters was observed in a large variety of works in which ZnO was doped, as it has been summarized in Table 1.

**Table 1**: Doped ZnO structural properties

| Ref. | Dopant Element | Doping Level | (Ox. State) Ionic Radius [pm] | $a$ | $a_D$-$a_0$ [1] | $c$ | $c_D$-$c_0$ [2] | Unit Cell Volume |
|---|---|---|---|---|---|---|---|---|
| [172] | Bulk ZnO | - | (+2) 74 | 3.2500 Å | | 5.2047 Å | - | 47.609 Å$^3$ |
| [118] | La | 5 % mol | (+3) 103 | 3.2497 Å | −1.3 × $10^{-3}$ Å | 5.2058 Å | −3.0 × $10^{-3}$ Å | 47.610 Å$^3$ |
| [173] | Ce | 1 % mol | (+3) 101 | 3.2503 Å | −1.6 × $10^{-3}$ Å | 5.2058 Å | −6.2 × $10^{-3}$ Å | 47.629 Å$^3$ |
| [174] | Nd | 5 % mol | (+2) 129, (+3) 98 | 3.2495 Å | 12.9 × $10^{-3}$ Å | 5.2058 Å | 20.7 × $10^{-3}$ Å | 47.605 Å$^3$ |
| [152] | Eu | 5 % mol | (+2) 117, (+3) 95 | 3.251 Å | 2.0 × $10^{-3}$ Å | 5.209 Å | 4.0 × $10^{-3}$ Å | 47.693 Å$^3$ |
| [159] | Gd | 5 % mol | (+3) 93 | 3.2735 Å | 20.6 × $10^{-3}$ Å | 5.2128 Å | 2.6 × $10^{-3}$ Å | 48.375 Å$^3$ |

| | | | | | | | | |
|---|---|---|---|---|---|---|---|---|
| [175] | V | 5 % mol | (+2) 79, (+3) 64, (+4) 58, (+5) 54 | 3.2522 Å | 0.5 × $10^{-3}$ Å | 5.2075 Å | −1.0 × $10^{-3}$ Å | 47.699 Å$^3$ |
| [128] | Mn | 5 % at. | (+2) 81, (+3) 72 (+4) 67, (+7) 60 | 3.2520 Å | 2.2 × $10^{-3}$ Å | 5.2093 Å | 3.0 × $10^{-3}$ Å | 47.710 Å$^3$ |
| [176] | Fe | 5.09 % mol | (+2) 75, (+3) 69 | 3.2536 Å | 2.3 × $10^{-3}$ Å | 5.2093 Å | 11.1 × $10^{-3}$ Å | 47.757 Å$^3$ |
| [177] | Co | 5 % mol | (+2) 79, (+3) 68 | 3.2503 Å | −2.0 × $10^{-3}$ Å | 5.2059 Å | −0.8 × $10^{-3}$ Å | 47.629 Å$^3$ |
| [178] | Cu | 5 % at | (+1) 91, (+2) 87 | 3.2494 Å | −0.2 × $10^{-3}$ Å | 5.2054 Å | −0.4 × $10^{-3}$ Å | 47.598 Å$^3$ |
| [154] | Ag | 5 % mol | (+1) 129, (+2) 108 | 3.2579 Å | 3.6 × $10^{-3}$ Å | 5.2220 Å | 3.7 × $10^{-3}$ Å | 48.000 Å$^3$ |
| [146] | Li | 5 % at | (+1) 90 | 3.225 Å | −30 × $10^{-3}$ Å | 5.162Å | −50 × $10^{-3}$ Å | 46.495 Å$^3$ |
| [140] | Mg | 5 % mol | (+2) 86 | 3.2585 Å | −3.6 × $10^{-3}$ Å | 5.2181 Å | −7.5 × $10^{-3}$ Å | 47.982 Å$^3$ |

[1] Relative variation of parameter a of doped ZnO ($a_D$) with respect to the pure counterpart evaluated in the paper ($a_0$). [2] Relative variation of parameters of doped ZnO ($c_D$) with respect to the pure counterpart evaluated in the paper ($c_0$).

In the work of Selvaraj et al., gadolinium (III) nitrate hexahydrate was used as a doping precursor as well[179]. Different levels of Gd doping were considered and the photocatalytic properties of Gd-doped ZnO nanoparticles were evaluated. The nanoparticles synthesized in this work, whose electron microscopy images are reported in Figure 4 -seen in the bottom panel- were obtained through a co-precipitation method in which the metal precursors were first mixed together at a proper ratio and then NaOH was added to allow the precipitation of the particles. In this case, after the synthesis, the obtained samples were also calcined at 500 °C for 2 h. The XRD pattern of the resulting samples (Figure 4, top left panel) showed that 5 mol.% Gd-doped ZnO nanoparticles presented a secondary phase. Therefore, this level of Gd doping can be assumed as the $Gd^{3+}$ solubility limit for this synthesis. Fourier transform infrared spectroscopy (FTIR) was also carried out (Figure 4, top right panel) and it evidenced that the peak associated with the Zn-O bond (443 $cm^{-1}$) was broader in the doped ZnO nanoparticles, due to the deformation of the lattice. A reduction of the band-gap energy value was also reported for increasing the amount of doping from 0 mol.% up to 3 mol.% of $Gd^{3+}$, while an increase was observed for 5 mol.% of doping. The reduced band-gap energy was ascribed to quantum confinement effects deriving from the reduction of the crystallite size as the Gd percentage increased.

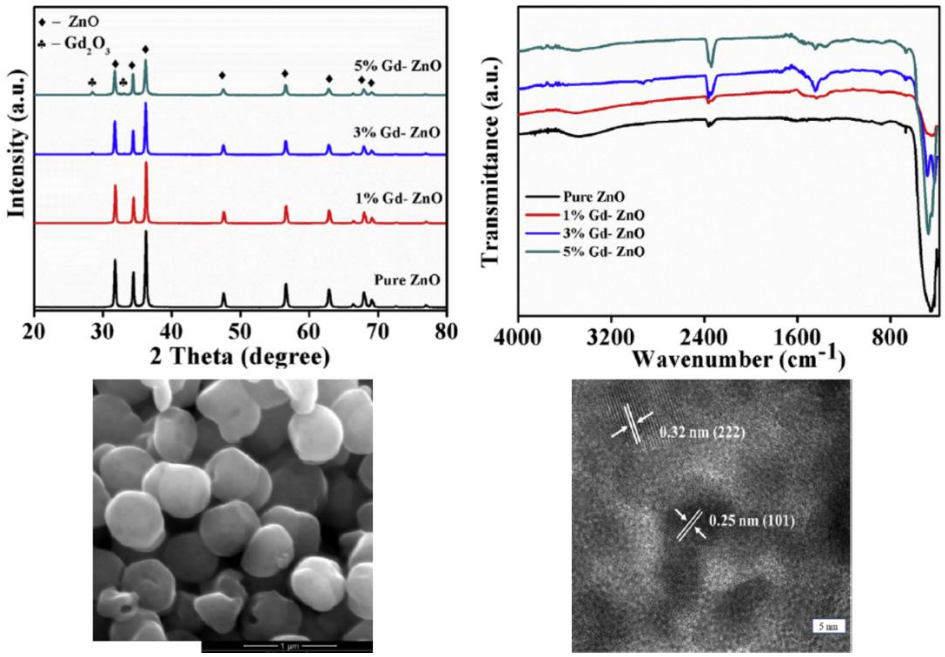


Figure 4: Characterization of gadolinium-doped ZnO nanoparticles. From left to right and top to bottom: XRD patterns and Fourier transform infrared spectroscopy (FTIR) spectra of the nanostructures at different doping levels, scanning electron microscope and transmission electron microscope images of 3% Gd-doped ZnO nanoparticles. Adapted from ref. [179].

Europium (Eu) doping was also demonstrated as a valuable tool to enhance the X-rays absorption properties of ZnO nanoparticles in cancer radiation therapy. In this case, Eu-doped ZnO nanoparticles were synthesized through a chemical precipitation technology[166]. Zinc acetate was dissolved in methanol together with europium (III) nitrate pentahydrate (5 mol.% of Eu doping) and the oxide formation was achieved through an NaOH addition. The resulting 8 to 9 nm sized ZnO:Eu nanoparticles showed an increased ability to generate reactive oxygen species, when subjected to X-rays, with respect to pure ZnO nanoparticles.

Other RE elements such as lanthanum (La) and cerium (Ce) were successfully used to prepare doped ZnO nanoparticles by the sol-gel method. For example, zinc nitrate and lanthanum (III) chloride heptahydrate were used to synthetize ZnO:La nanoparticles with improved light absorption properties and were successfully used as photo-anodes in dye-sensitized solar cells[118]. Ce-doped ZnO nanorods were fabricated starting from zinc chloride and cerium chloride[173]. The correct insertion of La and Ce dopants within the host ZnO crystal was confirmed by XRD. In both the cases, the wurtzite diffraction peaks present in the pattern of the doped nanorods

were shifted toward higher diffracting angles with respect to the pure counterparts, evidencing a higher crystalline defectiveness induced by the correct inclusion of the ions in the lattice.

Additionally, yttrium (Y, considered both an RE and TM element) was successfully included into the crystal lattice of ZnO nanosheets obtained by a co-precipitation method that involved the use of zinc chloride and yttrium (III) chloride hexahydrate. As reported by Sinha et al., a huge increase of the piezoelectric coefficient $d_{33}$ (up to 420 pm/V against 12.4 pm/V of pure ZnO) in Y-doped nanosheets was measured[162]. The XRD pattern of the Y-doped and undoped ZnO nanosheets revealed a shift toward higher angles of the peaks in the case of the doped material, evidencing a change in the lattice spacing among atoms. This aspect, together with the different charge of the inserted dopant and the changed morphology that the inclusion of the dopant has led, are considered the factors which increase the piezoelectric coefficient.

Differently from RE elements, for which wet chemical methods are the most frequently used to develop doped ZnO nanoparticles, transition metals have a plethora of synthesis methods available. However, sol-gel and co-precipitation methods are still the most used in the literature.

Among TMs, iron has been extensively studied as a dopant for ZnO due to its ability to induce a ferromagnetic behavior to the system[180–182]. Many works have dealt with flame spray pyrolysis synthesis[124,130,183], but a lot of works have also reported a wet chemical method to obtain Fe-doped ZnO nanoparticles. Samanta et al. reported the synthesis of Fe-doped ZnO nanoparticles ($Fe_xZn_{(1-x)}O$) with dimensions below 50 nm through a sol-gel method[157]. Zinc acetate dihydrate and ferric nitrate were dispersed in distilled water together with citric acid and ethylene glycol as anti-agglomerating agents at a temperature of 65 °C. Aqueous ammonia was added to precipitate the powders that were successively calcined. No secondary iron oxide phases were observed up to x = 0.15 of iron doping. Moreover, the unit cell volume of the ZnO:Fe nanoparticles crystal slightly changed with respect to the pure ZnO counterpart, with a not-proportional trend with respect to the dopant amount. This was attributed to the different fractional substitution of the two alternative coordination numbers of iron ($Fe^{2+}$ and $Fe^{3+}$) and their respective different bond lengths with oxygen. A general increase of the band-gap energy value was also found but without a direct proportionality with the amount of doping. In particular, the maximum increase was obtained for the x = 0.06 Fe ratio. In another work, the attention was focused on the antibacterial activity of Fe-doped ZnO nanoparticles obtained by a sol-gel method. Zinc nitrate hexahydrate, iron

nitrate nonahydrate and gelatin were dissolved in distilled water and the resulting nanoparticles showed a dimension of approximately 20–30 nm[184]. This study reported a reduced 2° angle of the (101) diffraction peaks together with a general decrease of the intensity of the wurtzite diffraction peaks by increasing the amount of Fe doping, which is attributed to an increased disorder of the ZnO lattice after Fe doping.

Manganese-doped ZnO nanoparticles were successfully prepared by a wet chemical method as well. The electronic and magnetic properties of the as-prepared Mn-doped ZnO nanoparticles were investigated[185], by changing the amount of the Mn dopant between 0.5 at.% and 3 at.%. The particles were synthesized from zinc nitrate and manganese nitrate being dissolved in ethanol and polyethylene glycol (PEG). Both the XRD patterns and TEM images showed that Mn doping sensibly reduced the particle size to 20–50 nm.

Cobalt is another commonly used TM element exploited as a dopant ion for ZnO. The sol-gel method was successfully used also in this case, as shown by the work of Lima et al. In this study, the promising photocatalytic and antibacterial properties of Co-doped ZnO were reported[186]. Zinc nitrate and cobalt nitrate were dispersed in aqueous diluted PVA and mixed together. The solvent was dried without the use of any mineralizing agent up until the gel formation, which was finally dried and calcined to form the nanoparticles. Cobalt was successfully inserted in the ZnO crystal without the formation of any secondary phase (up to 10 mol.%) of doping, and an increase of the unit cell volume was observed by increasing the amount of doping. The particles showed an average size below 40 nm and revealed a red shift of the UV-visible photo-absorption spectrum together with a reduction of the band-gap energy. The changes in the optical properties of ZnO:Co nanoparticles were attributed to the increase of the unit cell volume (due to the quantum confinement effect) and to the introduction of trap states in the band-gap, in agreement with other works such as the one by Kayani et al.[134]. On the contrary, a different behavior was found by Manjula et al.[187]. In this case, the nanoparticles were produced again by a co-precipitation method involving zinc acetate and cobalt acetate, and a blue shift of band-gap was observed with an increasing amount of dopant. These contrasting results evidence that a complete understanding of the mechanism of Co doping ZnO nanoparticles has not been reached and many other aspects have to be considered. Moreover, it is worth mentioning that a reduction of the photocatalytic activity was observed by other works[186,187]. This suggests that additional efforts are required to better understand

the role played by Co dopants in determining the physical properties of the resulting ZnO nanoparticles.

Wet chemical routes were also used to prepare copper-doped ZnO nanoparticles. An example is represented by the work of Abinaya et al.[154], where 5 mol.% Cu-doped ZnO nanoplates were synthesized by a hydrothermal method. Briefly, zinc acetate and copper (II) acetate monohydrate were dissolved in water, and NaOH aqueous solution was then added to the solution until a gel formed. Differently from the co-precipitation and sol-gel techniques previously discussed, in this case the gelled solution was placed in an autoclave at 160 °C for 5 h to get the formation of the ZnO:Cu powders. The as-prepared Cu-doped nanoplates exhibited variable dimensions of few hundreds of nm, as shown in Figure 5. Additionally, in this case, the dopant agent slightly increased the unit cell volume of the ZnO crystal. Cu-doped nanoplates were tested in terms of their antimicrobial properties against *E. coli* and *S. aureus*, showing a decrease in the minimum inhibitory concentration (MIC) with respect to pure ZnO (Figure 5).

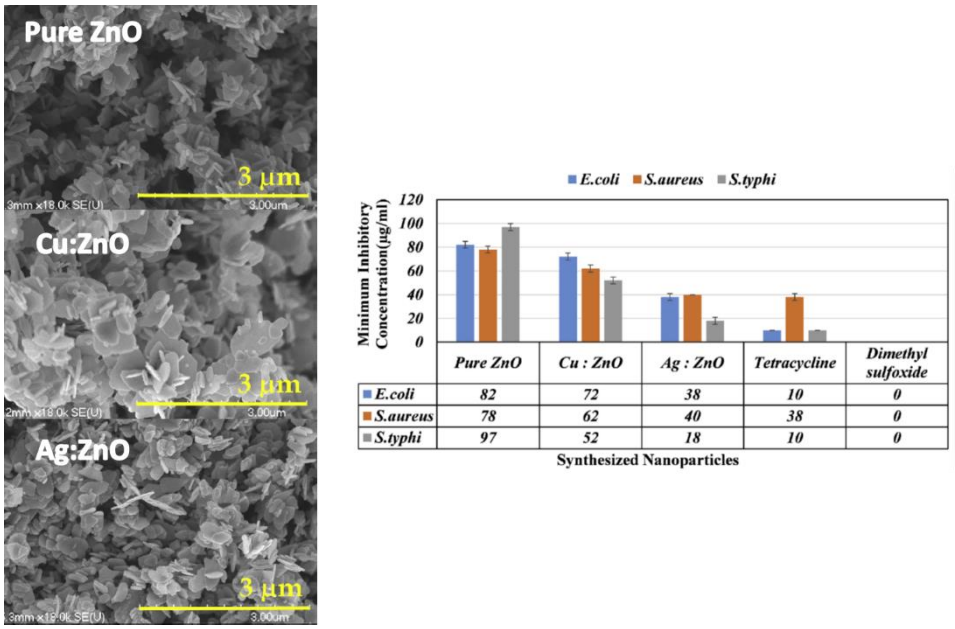


| | Pure ZnO | Cu : ZnO | Ag : ZnO | Tetracycline | Dimethyl sulfoxide |
|---|---|---|---|---|---|
| E.coli | 82 | 72 | 38 | 10 | 0 |
| S.aureus | 78 | 62 | 40 | 38 | 0 |
| S.typhi | 97 | 52 | 18 | 10 | 0 |

Figure 5: SEM images and antimicrobial performances of Cu- and Ag-doped nanoplates. Adapted from ref.[154].

Silver is a noble metal widely explored for antimicrobial applications due to the action of $Ag^+$ on bacterial membranes[188]. Therefore, it was considered as a TM element to prepare antimicrobial Ag-doped ZnO nanoparticles. A study going in this direction is reported by Sharma et al., in which zinc acetate and silver nitrate

were chosen as precursors, while ammonia was used as agent for inducing particle precipitation[167]. In addition, in this case, Ag doping induced a shift in the diffraction pattern toward higher angles with the increase of the doping amount.

Other metals such as magnesium, lithium and aluminum were used for doping ZnO nanoparticles by wet chemical synthesis. For magnesium, the enhanced photocatalytic activity of Mg-doped ZnO nanoparticles with respect to their pure counterparts was reported[140]. The doped nanoparticles were prepared by a co-precipitation method and the effective insertion of an Mg dopant in the host ZnO crystal lattice was confirmed by XRD which highlighted an increase of the volume of the unit cell.

With regard to lithium doping, a work reported its use in enhancing the photoactivated ROS generation of ZnO when using this system for anticancer therapy[146]. In this work, zinc acetate dihydrate and lithium acetate dihydrate were used as precursors in a polyol synthesis performed in triethyleneglycol (TREG) as the solvent.

Finally, Al-doped ZnO (AZO) nanoparticles were synthesized by a wet chemical method and their antibacterial performances were studied. Zinc nitrate hexahydrate was mixed with the aluminum precursor (aluminum nitrate nonahydrate) for the oxide synthesis[189].

Among wet chemical syntheses, the reverse-micelles microemulsion method was also explored for the preparation of doped ZnO nanoparticles[190]. The presence of specific surfactants by this approach can lead to peculiar ZnO morphologies, such as hollow structures[191], and can also limit the dimensions of the particles during nucleation. For example, the reverse-micelles method has been successfully exploited to develop Eu-doped[192,193] and Mn-doped[194] ZnO nanorods and nanoparticles with a controlled size. In particular, in the case of europium-doped nanoparticles, it is possible to obtain either very small nanospheres with an average diameter of about 5 nm, or nanorods with lengths of some hundreds of nanometers and a diameter of some tens of nanometers, by changing precursors ($Zn(CH_3COO)_2 \cdot 2H_2O$ and $Eu(CH_3COO)_3 \cdot 4H_2O$ for nanospheres and $ZnCl_2$ and $EuCl_2$ for nanorods), oils and surfactants (sodium bis(2-ethylhexyl) sulfosuccinate and heptane for nanospheres and octane, CTAB and butanol for nanorods).

As a summary, it may be stated that wet chemical methods are the mostly exploited ones for the development of doped ZnO nanoparticles. The main advantages of these techniques are the simplicity of the process and the wide variety of morphologies obtainable. Table 2 summarizes the main aspects of some of the techniques used to synthesize doped ZnO nanoparticles.

**Table 2**: Dopant ions and their respective precursors for the synthesis of ZnO nanoparticles by wet chemical methods.

| Dopant Element | Dopant Precursors | Doping Level | Solvent | Particles Dimensions | Ref. |
|---|---|---|---|---|---|
| La | $LaCl_3 \cdot 7H_2O$ | 5 % mol | $H_2O$ [a] | 123 nm [1] | 118 |
| Ce | $CeCl_3 \cdot 7H_2O$ | 1 % mol | $H_2O$ [a] | 20–30 nm [1] | 173 |
| | $Ce(NO_3)_2 \cdot 6H_2O$ | 0.1–5 % mol | $H_2O$ [b] | 70–85 nm [1] | 114 |
| Nd | $Nd(NO_3)_3 \cdot 6H_2O$ | 5 % mol | $H_2O$ [a] | 101 nm [1] | 174 |
| Sm | $Sm(NO_3)_3 \cdot 6H_2O$ | 1–4 % mol | $H_2O$ [a] | 35 nm [1] | 195 |
| Eu | $EuCl_3 \cdot 6H_2O$ | 5 % mol | $H_2O$ [a] | 79 nm [1] | 152 |
| | $Eu(NO_3)_3 \cdot 5H_2O$ | 5 % mol | $CH_3OH$ [a] | 9 nm [2] | 166 |
| Gd | $Gd(NO_3)_3 \cdot 6H_2O$ | 5 % mol | $CH_3OH$ [a] | 9 nm [2] | |
| | $Gd(CH_3CO_2)_3$ | 2–30 % mol | $CH_3CH_2OH$ | 4 nm [2,3] | 165 |
| V | $NH_4VO_3$ | 1 % mol | $H_2O$ [a] | 47 nm [2] | 196 |
| Mn | $Mn(NO_3)_2$ | 0.5–3 % mol | $CH_3CH_2OH$ | 50–120 nm [2] | 185 |
| | $MnCl_2 \cdot 4H_2O$ | 1–5 % mol | $CH_3OH$ | 100 nm [2] | 128 |
| Fe | $Fe(SO_4) \cdot 7H_2O$ | 3–7 % mol | $H_2O$ [a] | 15–35 nm [2] | 197 |
| | $FeCl_3$ | 1–10 % mol | $H_2O$ [a] | 9–15 nm [2] | 164 |
| | $Fe(NO_3)_3$ | 2–6 % mol | $H_2O$ [a] | ~250nm [4] | 198 |
| Co | $Fe(NO_3)_2 \cdot 6H_2O$ | 1–10 % mol | $H_2O$ | 25–50 nm [2] | 186 |
| | $CoCl_2$ | 5–10 % mol | $H_2O$ [a] | Various morphologies | 177 |
| Ni | $NiCl_2 \cdot 6H_2O$ | 3 % mol | $CH_3CH_2OH$ [a] | 25–40 nm [1] | 161 |
| Cu | $CuCl_2 \cdot 2H_2O$ | 0.5–30 at % | $H_2O$ [b] | ~250 nm [4] | 178 |
| Ag | $AgNO_3$ | 5 % mol | $H_2O$ [a] | 80 nm × 350 nm [5] | 154 |
| Li | $Li(CH_3CO_2)_3 \cdot 2H_2O$ | 3–5 at % | TREG ($C_6H_{14}O_4$) | ~250 nm [4] | 146 |
| Mg | $Mg(NO_3)_2 \cdot 6H_2O$ | 5 % mol | $H_2O$ [a] | 62 nm | 168 |
| Al | $Al(NO_3)_3 \cdot 9H_2O$ | 15 % mol | $H_2O$ [a] | ~ 60 nm [1] | 189 |

[a] NaOH as base, [b] $NH_4OH$ as base [1] Rod's mean diameter. [2] Spherical particles' diameters. [3] TMAH and oleic acid were also added in the synthesis procedure. [4] The dimensions have been estimated by electron microscopy images. [5] Nanoplates' thicknesses and diameters.

## 1.4.2 Combustion Methods

Apart from wet chemical methods, combustion-based synthesis techniques have been also explored as an alternative for the synthesis of doped ZnO nanoparticles.

In solution combustion methods, the precursors of the desired material, i.e., zinc and dopant element precursors, are firstly dissolved in a fuel (urea, glycine fuels or citric acid)[199]. Then, the solution is placed in a muffle furnace pre-heated to a temperature higher than the ignition temperature of the fuel. During the combustion of the fuel, a strong exothermic reaction takes place between the fuels and the oxidizing agents present in the solution, generating the target oxide and gaseous species[199].

This gas generation leads to an expansion of the volume of the solid phase and a rapid decrease of its temperature, leading to the formation of ultra-fine and well dispersed powders[199]. This last aspect is very important in biomedical applications where the formation of clusters must be avoided as much as possible since it affects the cellular uptake of nanoparticles.

By tuning the amount of fuel in the solution, various ZnO nanomaterials were synthesized through this versatile synthesis mechanism, showing different morphologies such as pyramid-like particles, nanodisks[200] or nanoparticles[201].

Concerning the doping of nanomaterials, different ions have been successfully included into ZnO. An example is represented by noble metals such as gold and silver. In the work of Pathak et al., both Ag- and Au-doped ZnO nanoparticles were synthesized by a solution combustion method[136]. Zinc nitrate hexahydrate was mixed in urea (used as fuel) together with a small amount of silver nitrate or tetrachloroauric-III-acid hydrate to act as dopants. The obtained solution was dissolved in 5 mL of water pre-heated to 80 °C and then placed in a furnace at 500 °C to start the ignition. Differently from sol-gel methods, the dopant agents generated the secondary phases of noble metals, as observed from the SEM images and XRD patterns reported in Figure 6.

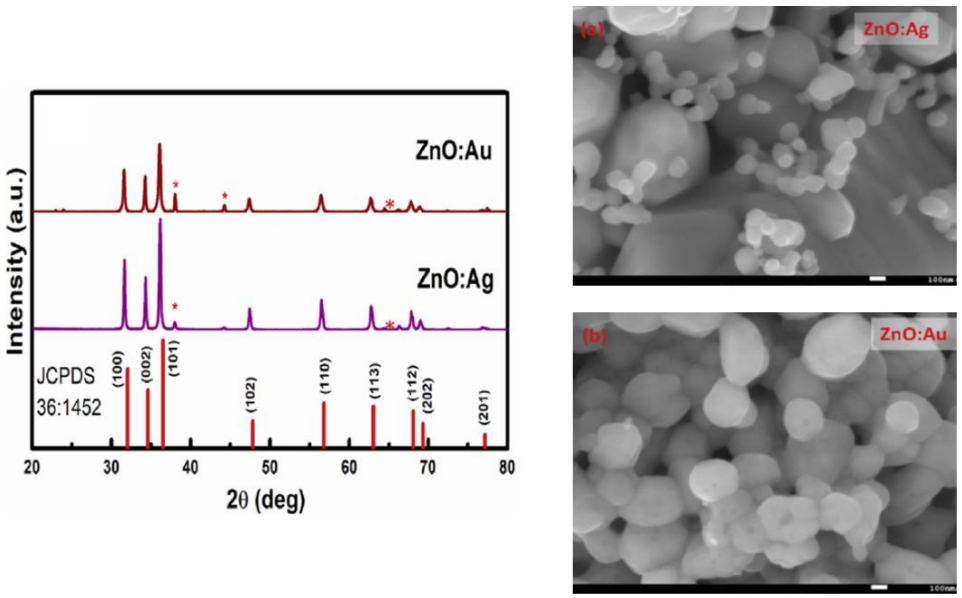


Figure 6: Au- and Ag-doped nanoparticles synthesized through a combustion method. On the left is the XRD patterns of the resulting particles, highlighting the presence of further peaks related to the secondary phases. On the right, the corresponding scanning electron microscope images of Ag-doped (a) and Au-doped (b) nanoparticles. Adapted from ref.[136].

ZnO was also doped with nickel by a solution combustion method. In the work of Silambarasan et al., zinc acetate, nickel (II) acetate, ethanol and ethylene glycol were mixed together and inflamed to get the doped ZnO powder[202]. The XRD patterns showed the high crystallinity of the material. However, also in this case, the doped samples showed additional diffraction peaks related to an NiO secondary phase.

A similar problem was observed for vanadium-doped ZnO nanoparticles. In this case, zinc nitrate hexahydrate and glycine were used as a precursor and to fuel for the reaction, respectively[175]. The dopant precursor was ammonium metavandate ($NH_4VO_3$) while water was used as solvent. The XRD analysis performed on the burnt powders showed again the presence of additional peaks related to the formation of a secondary phase, especially for high doping levels.

In another work, Ti-doped ZnO powders obtained by a solution combustion technique exploited titanium (IV) isopropoxide as a dopant precursor[203]. In this case, the additional XRD peaks due to $TiO_2$ appeared only at the highest level of doping (7.5 at.%), while Ti ions were correctly inserted in the host ZnO lattice for lower dopant concentrations (up to 5 at.%).

The solution combustion method was also proposed to synthesize iron-doped zinc oxide nanoparticles in a faster way than sol-gel methods[204]. Zinc nitrate, iron nitrate and urea were used as precursors and fuel, respectively. The solution was heated at 400 °C up to the ignition of the solution and until the formation of a very fragile foam that could be reduced to powder form. Interestingly, the XRD pattern representative of these powders did not present any additional peaks due to the secondary phase up to 5% of Fe doping, while weak peaks related to ferrite were detected only for higher doping levels. However, the formation of secondary phases was not considered a drawback at all. Actually, it was responsible for the promising ferromagnetic behavior observed in the mostly doped samples, even if a weaker hysteresis loop was also found for lower doping levels.

The iron doping of ZnO nanoparticles was achieved by flame spray pyrolysis as well. Differently from the standard solution combustion described previously, the precursor solution is sprayed before setting on fire. Again, a fuel is needed to allow the self-sustainability of the flame as in the case of the solution combustion method[205]. However, a nozzle tip is usually exploited to nebulize the solution precursor.

Many studies have exploited flame spray pyrolysis rather than sol-gel methods to prepare Fe-doped ZnO nanoparticles with an improved biostability in aqueous media[183,206,207]. Concerning this aspect, the work of Xia et al. highlighted the decreased dissolution of Fe-doped ZnO nanoparticles in biological media[207]. This doping reduced the amount of $Zn^{2+}$ dissolved in the biological medium with positive consequences on the biocompatibility of the nanoparticles system. The doped nanoparticles were synthesized through flame spray pyrolysis. Zinc and iron naphthalene were mixed separately in xylene. The solutions were sprayed, atomizing the precursor and allowing for combustion through the co-delivery of methane and oxygen. The resulting doped particles were smaller with respect to the pure counterparts and the XRD patterns did not exhibit additional peaks apart from the usual wurtzite phase ones.

Other works reported the use of the same synthesis procedure to develop ZnO:Fe nanoparticles with a good reproducibility[183,206]. Each of these works was focused on the dissolution kinetic of the produced particles and their fate in a biological environment. In all the cases, iron doping was demonstrated to be a very interesting tool to limit nanoparticles' dissolution and to enhance ZnO cytocompatibility.

As a conclusive remark, it can be stated that combustion methods are not able to efficiently incorporate the dopant agent in the ZnO crystalline structure with

respect to wet chemical techniques. This can be the explanation for the limited use of solution combustion routes to fabricate doped ZnO nanoparticles with respect to sol-gel or hydrothermal routes.

### 1.4.3 Other Techniques

Despite their application being mostly limited to the synthesis of ZnO films, other synthesis techniques for doping ZnO are worthy of mention.

An example is chemical vapor deposition (CVD), which is typically used to grow thin films. In the work of Shuang et al., Mn-doped ZnO flower-like structures were successfully grown in a CVD system and the corresponding optical properties were analyzed[208]. In this case, Zn and $MnCl_2$ in powder form were used as solid source materials for growing the flower-like structures. The SEM results reported highly oriented structures, but most of the dopant ions accumulated on the outermost surface of the nanostructures. A Fe/Co doping of ZnO nanowires was obtained by the CVD method as well and the resulting nanostructures were characterized by a high degree of crystallinity and an interesting ferromagnetic behavior[209].

Sonochemical syntheses are recently acquiring a lot of interest as well, since the high energy which is freed due to air bubble cavitation can be exploited to locally overcome the limits of pressure and temperature which commonly affect other techniques[210]. A sonochemical wet impregnation method was instead exploited for the fabrication of Ce-doped ZnO nanoparticles for photocatalytic applications[211]. The doped ZnO nanoparticles were fabricated by keeping in sonication a solution of ZnO nanoparticles and ammonium ceric nitrate in distilled water, and then drying the precipitates.

Other examples include the synthesis of ZnO–graphene nanohybrids, where different morphologies could be obtained according to the synthesis solution pH[212]. The sonochemical approach has been successfully exploited also to dope ZnO with both common and exotic doping elements like dysprosium[213], magnesium[214] and praseodymium[215], revealing the high versatility of this method.

An alternative technique for doping is to mix pure ZnO powders with those of the dopant species, and then thermally anneal the mixed powders together at a high temperature. This method was exploited by Ivetic et al. to obtain Mg-doped nanoparticles and to evaluate the increase of the corresponding photocatalytic activity with respect to pure ZnO[216]. Mechanical alloying - which does not use temperature, but simply mixes and ball mills ZnO and the dopant metal powders together - was able to include the metal into the ZnO particles. With this method,

Fe was included in the ZnO matrix up to 7.08% without any clear evidence of the formation of iron clusters[176]. A ferromagnetic behavior was also found in this system.

Finally, other techniques are based on the deposition of doped ZnO coatings and thin films such as magnetron sputtering[131], pulsed laser deposition[217] and many others.

In summary, wet chemical methods are surely the most exploited and promising routes to obtain good quality doped ZnO nanoparticles, with a large variety of precursors and parameters that allow an extreme customizability of the resulting material. Other techniques, like combustion methods, revealed to be useful in terms of the rapidity of reaction but the dopant atom inclusion in the crystalline lattice of ZnO is poor with respect to chemical routes, limiting their applications to systems in which the quality of the material is not a key parameter.

## 1.5 Use of Doped ZnO NPs in the Biomedical Field

Zinc oxide has been part of many applications in the biomedical field. Many of them are related to its antimicrobial activity[218], but other applications also prove the use ZnO as a therapeutic agent against cancer cells[219,220] or as a tool for tissue engineering[71,79]. However, despite pure ZnO showing many interesting properties, it still presents many factors that need to be further optimized for its further exploitation in the biomedical filed in general, and in nanomedicine in particular.

A first important aspect to be considered is its dissolution behavior in aqueous media. Actually, zinc oxide can dissolve in water generating free $Zn^{2+}$ cations. This can more easily occur in presence of high surface area nanoparticles because of their superior surface reactivity[218]. $Zn^{2+}$ cations are successfully exploited to increase the bactericidal activity of ZnO[221]. However, this aspect may also result in an increased cytotoxicity that could prevent its use in the human body.

Despite the high quality of ZnO as an antimicrobial agent, its performance may be even enhanced if the corresponding photocatalytic activity is further optimized. ZnO is a semiconductor able to generate highly cytotoxic/antimicrobial ROS[222]. Upon interaction with electromagnetic radiation, semiconducting ZnO materials are able to promote electrons from the valence band to the conduction band, generating free electrons which are able to migrate up to the outermost ZnO surface and react with the external aqueous environment, leading to the generation of ROS[93,223]. Band-gap engineering of ZnO may be a valuable tool to increase the efficiency of this process, reducing or increasing the energy required to generate free electrons

and controlling the efficiency in ROS generation. This ability in generating ROS can be exploited in photodynamic therapy, transforming ZnO nanoparticles into an interesting weapon against cancer.

Finally, ZnO on its own lacks intrinsic imaging properties which are very useful for various biomedical applications, such as in theranostics. Tuning its dimensions and energy band-gaps, the corresponding optical properties can be properly optimized and interesting luminescent properties can be gathered as in the case of ZnO quantum dots[165,224]. Moreover, as already stated, the inclusion of transition metals in the crystal lattice confers on ZnO a magnetic behavior, paving the way to its exploitation as a contrast agent in magnetic resonance imaging[120].

All these aspects can be fulfilled by doping ZnO with specific elements. In the following, the main findings in this sense will be described.

### 1.5.1 Biological Behavior

One of the main problems related to the use of ZnO in biomedical applications is its dissolution in aqueous/biological media[225]. ZnO is in fact stable at a basic pH, while it can easily dissolve in an acid environment[226]. The pH of a biological medium depends on several parameters and can change over time. Therefore, it is possible to have a certain degree of ZnO dissolution, which can be even enhanced when the dimensions of the nanoparticles under analysis are highly reduced, exposing a large area to the liquid environment[226]. The dissolution leads to the release of zinc cations ($Zn^{2+}$) which have been proven to be harmful for cells, damaging the cellular zinc homeostasis and, consequently, leading to lysosome and mitochondria damage and cell death[225]. Hence, particular attention should be paid to the control of ZnO dissolution, in order to limit cytotoxicity.

For the chemical design of ZnO-based systems with increased zinc cation stabilities in media, specifically used in medical applications, one successful approach is represented by the methodology based on electrochemical equilibria in aqueous solutions[227]. An alternative approach to improve the biocompatibility and zinc cation stability of ZnO nanoparticles is to cover their surface with inorganic[228–230] or organic[142,231,232] coating materials. However, this approach requires additional synthesis steps and a general increase of the nanoparticles' size, which may represent a limitation for specific applications.

The best situation would be to prepare ZnO nanoparticles that are intrinsically stable in a biological medium, without the addition of any external layer. This task can be addressed once again by including a dopant atom in the crystal lattice of ZnO.

Actually, Fe doping has been proposed as a stabilizer of ZnO in aqueous media. George et al.[130] demonstrated that the inclusion of Fe ions into ZnO nanoparticles successfully decreased the dissolution rate by measuring the amount of zinc ions released in an electrolytic solution at pH 7 ± 0.04. The $Zn^{2+}$ kinetics were evaluated by measuring the nitric acid amount required to maintain the solution pH at the fixed value. The results showed that, by increasing the amount of doping, the dissolution of the nanoparticles decreased accordingly (Figure 7). This behavior was attributed to the stronger chemical bonds between the iron dopant and the host ZnO lattice, which resulted in a higher difficulty for the $Zn^{2+}$ ions to be released in the environment.

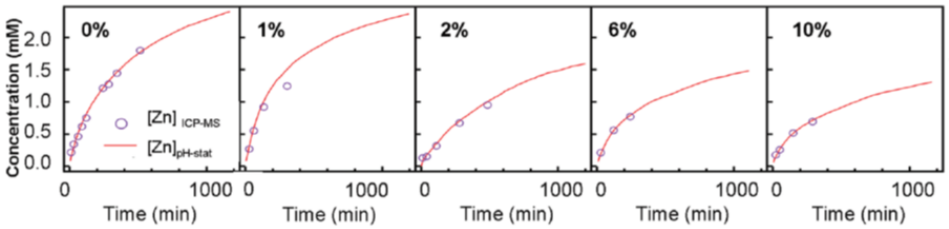


Figure 7: Zinc release in an aqueous solution at pH 7 by the dissolution of Fe-doped ZnO nanoparticles at different doping levels. Adapted from ref. [130].

First principle calculations confirmed these experimental evidences[110]. The computed energetics evaluated for different iron doping levels showed that iron can stabilize the ZnO nanoparticles. Moreover, in the same work, it was also proven that the coordination state of iron was mainly $Fe^{2+}$ and that the inclusion of the dopant did not damage the crystal lattice in a considerable way.

In another work, Fe-doped ZnO nanoparticles, synthesized by flame spray pyrolysis, were tested in terms of cytotoxicity[206]. The authors analyzed different Fe doping levels to find the best one, which allowed the selective killing of tumoral cells. The cytotoxicity assays were performed on normal murine mesenchymal stem cells (MSCs), human bronchial epithelial cells (Beas-2B), cancer murine lung squamous carcinoma cells (KLN-205) and human cervical cancer cells (HeLa) cells. The experimental results revealed that NPs with low doping levels were more efficient at damaging tumoral cells rather than the healthy cells. Furthermore, the amount of $Zn^{2+}$ released, measured by FluoZin-3 staining coupled with fluorescence microscopy (Figure 8), was reduced by increasing the Fe doping.

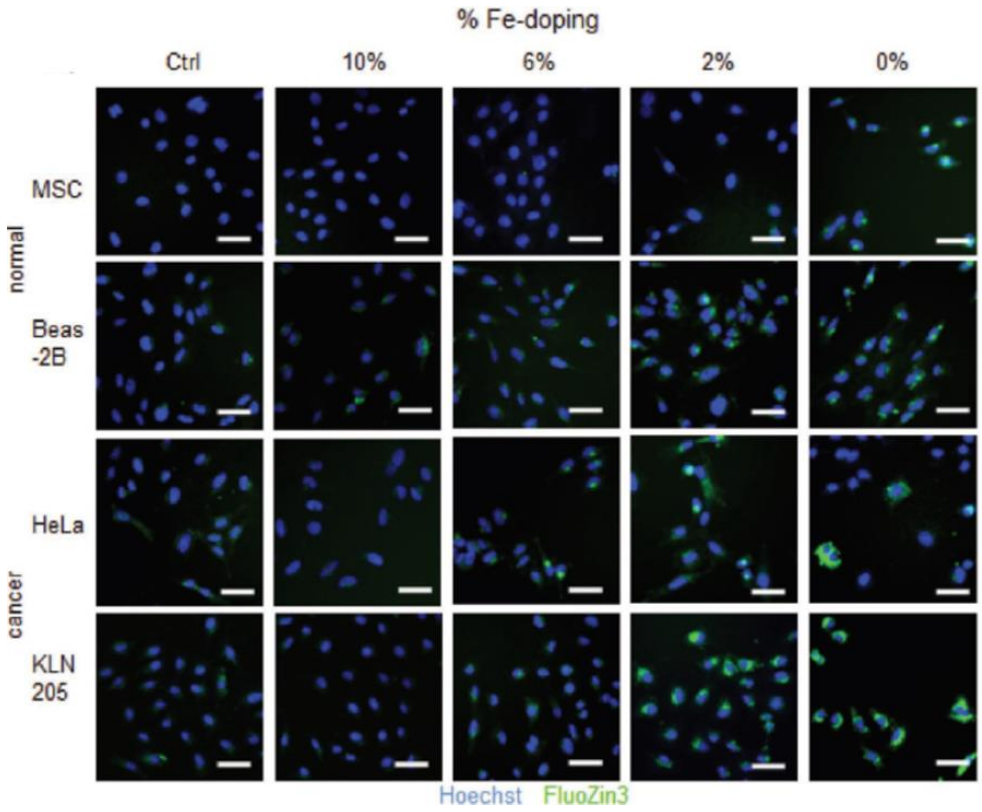


Figure 8: Fluorescence microscopy images of different cell lines exposed to differently Fe-doped ZnO nanoparticles (no nanoparticles (NPs) are present in the control samples). The green signal is related to $Zn^{2+}$ free ions (FluoZin3-AM binds to ions and have a green fluorescent emission), the blue signal is related to the presence of cell nuclei. Less doped ZnO nanoparticles lead to a higher concentration of free zinc ions. Adapted from ref.[206].

In detail, 2 wt.% Fe doping was considered the best choice to achieve selectivity between tumoral and normal cells. This finding was further confirmed by co-culture cells experiments, finding an increased toxicity against cancer cells with respect to healthy ones. Moreover, undoped ZnO nanoparticles were tested as well, which are toxic for any cell line. On the other hand, 10 wt.% Fe-doped nanoparticles were biocompatible for both the cell typologies.

Fe-doped ZnO nanoparticles obtained with a similar synthesis method were tested in another work in vivo[207]. Hatching zebrafish embryos were taken as an indication of the toxicity of Fe-doped and undoped ZnO nanoparticles. Zebrafish were bred so as to achieve fertilization and the embryos were collected. Then, the embryos were treated with ZnO nanoparticles doped with different Fe levels, and the hatching rate was evaluated. The results showed that there were significant

improvements with increased doping levels. Again, this was related to a decreased release of zinc cations. In the same work, it was also shown that iron doping can reduce the pulmonary inflammation and oxidative stress in rats and mice.

Despite the previous work being focused on the ability of a single dopant (iron) to stabilize the ZnO NPs stability, very promising results are found in terms of an increased cytocompatibility by using Fe-doped ZnO nanoparticles. This is corroborated by in vitro and in vivo tests, attributing the increased biocompatibility to a decreased level of zinc cations being released.

## 1.5.2 Antimicrobial Agents

Pure ZnO nanoparticles have been extensively used as antibacterial agents due to their photo-oxidizing and photocatalytic properties[218]. Its antimicrobial properties can be tailored in several ways: parameters like morphology, size, concentration, surface defects and functionalization all contribute to change the performances of ZnO nanoparticles in this field[218]. Despite the mechanisms through which ZnO induces bacterial and fungi death being still under debate, there are three main hypotheses, summarized in Figure 9.

The first one deals with ROS generation. As a matter of fact, ZnO is able to generate reactive oxygen species as a consequence of its photoexcitation from UV light in aqueous media[222]. The idea is that the electromagnetic radiation gives electrons lying in the valence band (VB) sufficient energy to jump to the conduction band (CB). The hole left in the VB can react with water, generating a hydroxyl radical (•OH) and $H^+$, while the CB electron can react with oxygen to generate a peroxide radical[233]. At this point, the following reactions can occur:

$$\bullet O_2 + H^+ \rightarrow HO_2\bullet, \qquad (4)$$

$$HO_2\bullet + H^+ + e^- \rightarrow H_2O_2, \qquad (5)$$

This leads to the formation of hydrogen peroxide, which can destroy bacteria by penetrating their membrane. If the generated ROS exceeds the capability of the bacterium to produce reducing agents able to contrast this phenomenon, oxidative stress phenomena are induced[234].

The second mechanism is based on the release of harmful zinc cations. Indeed, ZnO nanoparticles can dissolve releasing $Zn^{2+}$ ions into the environment, affecting the metabolism of bacteria and leading to dysfunctions of their enzymatic systems[218]. A work from Li et al. reported evidences of these effects[221]. ZnO nanoparticles, bulk ZnO and a solution of $Zn^{2+}$ ions were analyzed against *E. coli*,

finding similar toxicity curves and confirming the negative influence that zinc cations may have on bacterial viability. However, this work further confirmed that ZnO toxicity is subjected to several intrinsic conditions like the size, porosity, and concentration of the particles, coupled with external parameters like pH and the composition of the environment[218].

Finally, another possible mechanism that explains the antibacterial action of ZnO is the absorption of the nanoparticles into the bacteria membrane, leading to a physical disruption of the cell wall and ultimately to the microorganism's death[235]. This is possible because ZnO nanoparticles typically present a positive Z-potential, i.e., a positively charged surface, while the bacteria surface is characterized by a negative charge. Therefore, ZnO NPs are attracted toward the bacterium, damaging its outer membrane. Moreover, if the particles are smaller than 10 nm, NPs' internalization into the bacterium can also occur, damaging the internal components of the cell[234].

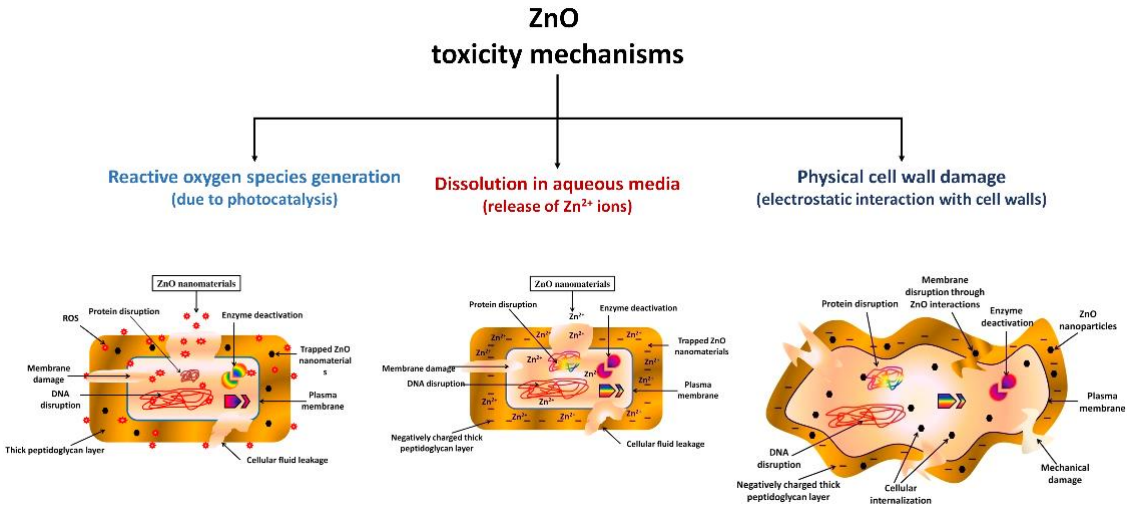


Figure 9: Schematic reporting the main ZnO toxicity mechanisms that make this material an effective antimicrobial agent. Adapted from ref.[234].

Additionally, it is worth mentioning that a different behavior can be found for different kinds of microorganisms. Actually, among bacteria there exist two main typologies, i.e., Gram-positive and Gram-negative ones, which show a different external cell membrane structure[218]. Therefore, it is clear that tests aimed at proving the antimicrobial mechanism of ZnO nanostructures should be performed on both these biological systems: Gram-negative bacteria such as Escherichia coli (*E. coli*), and Gram-negative ones such as Staphylococcus aureus (*S. aureus*)[236,237].

Doping has been demonstrated as a useful tool to tailor the antimicrobial properties of ZnO nanoparticles. Indeed, the generation of antibacterial reactive oxygen species from the customization of the optical properties due to ZnO doping can be an advantage.

Some improvements in the photocatalytic properties and photoexcitation efficiency, which are the main mechanism through which antimicrobial ROS are generated in ZnO-based systems, were found in several works by using different doping agents[140,145,187,211].

For example, silver is a possible choice in terms of dopants which are useful for increasing the antibacterial activity of ZnO. The reason lays in the intrinsic bactericidal activity of silver ions against a wide spectrum of bacteria typologies[188]. As shown in the work of Demirel et al., ZnO structures with large surface area morphologies and doped with different Ag amounts were tested against different microorganisms (bacteria, yeasts and fungi)[235]. Disk diffusion tests highlighted that hexagonal ZnO particles were effective in contrasting microorganism growth when pure ZnO was used. However, Ag doping was found to be efficient in boosting the antibacterial properties (with an optimal doping value of 0.05 mol.%) against most of the tested biological species, resulting in a broad spectra antimicrobial device.

Another work reported the comparison between pure, gold- and silver-doped ZnO nanoparticles synthesized by a combustion method[136]. The photocatalytic efficiency resulting from the degradation of methylene blue under UV exposure was proven to be higher for the doped particles. In particular, Ag-doped ZnO NPs reached a 45% methylene blue degradation efficiency after 160 min against a 25% efficiency for Au-doped ZnO and 8% for undoped ZnO. This result was attributed to the noble metal clusters formed on the surface of ZnO nanoparticles during synthesis, which inhibited the recombination of the photogenerated electron/hole pairs. However, the antibacterial activity against *E. coli* and *S. aures* was lower for doped ZnO with respect to the pure counterpart. On the contrary, Ag doping was effective against *E. ashbyii*, even if a direct comparison with other doped ZnO systems was difficult because of the presence of dopant clusters rather than a correct inclusion of dopant atoms in the ZnO crystal lattice. In the work by Sharma et al.[167], ZnO particles were successfully doped, including Ag ions into the crystal lattice and a reduction of the minimum inhibitory concentration (MIC) was found for *S. aures* with respect to pure ZnO, in contrast to what was found in the previous work.

Silver doping was also compared to copper doping in terms of antimicrobial activity. Hydrothermally synthesized undoped, Cu- and Ag-doped ZnO nanoplates were tested against *E. coli*, *S. aureus* and *Salmonella typhi* by a well diffusion

method in order to determine the MIC[154]. The results reported an increased bactericidal activity of both doped ZnOs, the result of a decreased MIC. Moreover, Ag-doped nanoplates were more efficient than Cu-doped ones. In this work, the authors also highlighted the role of light. The antimicrobial properties of the doped ZnO nanostructures were limited when the bacterial seeding and treatment processes were performed in dark conditions, suggesting that the photoexcitation of the semiconductor plays an important role in determining the antimicrobial activity of ZnO.

Cu-doped ZnO nanoparticles were analyzed in terms of antibacterial activity in another study. A green combustion method was followed to synthesize the nanoparticles, which were tested against *E. coli*, *S. aureus*, *Bacillus subtilis* and *Klebsiella* through the agar diffusion method[238]. Their photocatalytic activity was also evaluated by measuring the degradation of the Acid Black 234 (AB) organic dye under sunlight irradiation. Using the Cu-doped ZnO nanoparticles resulted in a more efficient dye degradation with respect to the pure counterpart as well as an inhibition of the bacterial growth for all the examined biological species. In particular, ZnO nanoparticles with higher levels of Cu doping showed enlarged inhibition zones with respect to a standard drug (cephradine). The reason behind the antibacterial activity of these nanoparticles was attributed to the permeation of Cu ions through the negatively charged bacterium cell membrane because of its electrostatic attraction.

Al-doped ZnO (AZO) nanorods were also proven to have superior antimicrobial properties with respect to pure ZnO[189]. The AZO nanorods showed a larger inhibition zone against *E. coli* and *E. hirae* (10.19 ± 0.04 mm and 10.20 ± 0.2 mm, respectively) with respect to pure ZnO (9.54 ± 0.08 mm and 9.62 ± 0.08 mm), and similar results with respect to the kanamycin drug (10.16 ± 0.07 mm and 10.17 ± 0.08 mm). This behavior was again attributed to the electrostatic interaction between the particles and the bacterial cell walls.

Iron doping was studied to improve the antibacterial ability of ZnO as well. In the work of Li et al.[124], FSP synthesized Fe-doped ZnO nanoparticles were tested against *B. subtilis*, *E. coli* and *Pseudomonas putida* through a high throughput bacterial viability assay able to evaluate the viability of bacteria through fluorescence signals. Interestingly, Fe doping did not impact in a major way on the antibacterial activity of ZnO, finding comparable results with respect to its pure counterpart. In another work, Fe- and Mn-doped ZnO nanoparticles were synthesized by a wet chemical method and analyzed in terms of photocatalytic activity before the antimicrobial tests[239]. The degradation of methylene blue under

UV light was taken to identify the system with the best photocatalytic activity, which was 10% Fe-doped ZnO NPs. Disc diffusion assays reported that the 10%-doped system (both Mn- and Fe-doped) exhibited the highest antimicrobial activity against several pathogenic entities compared to lower doped (1%) systems and pure ZnO NPs. The reason for the improvement of both photocatalytic and antibacterial properties was related to the increased generation of ROS, and that Mn and Fe ions may lead due to the formation of additional states in the band-gap structure of ZnO.

Additionally, magnesium was proven to increase the antimicrobial performances of ZnO. It was found that different Mg doping levels change the photocatalytic activity and rhodamine B degradation of the doped ZnO nanoparticles, finally influencing their antibacterial activity against both Gram-positive and Gram-negative bacteria[140]. The photocatalytic activity was found to increase with the doping level, reaching a maximum in the case of 7.5% Mg doping, and then decreasing for a further increase of the doping amount. The enhancement was attributed to the enlarged surface area of the ZnO NPs and to the oxygen vacancies induced by doping. For the antibacterial activity, disc diffusion analyses gave, as a result, an increment of the inhibition zone with the increase of the doping level. Another work reports the use of Mg-doped ZnO NPs loaded with an antibiotic drug[170]. An enhanced antimicrobial activity was found, and this behavior was attributed to the destabilization of the cell wall induced by the nanoparticles and their consequent increased permeability, which allowed the antibiotics to penetrate the bacterium membrane more efficiently.

Rare earth elements were also proposed as dopants to enhance the antibacterial properties of ZnO. In the work of Karunakaran et al., Ce-doped ZnO nanoparticles were tested first as a photocatalyst for cyanide photooxidation and then as a antimicrobial agent against *E. Coli*[211]. The authors reported an increased bactericidal activity in dark conditions for the doped ZnO NPs which was related to the physical attachment of the particles onto the bacteria membranes. Other examples are terbium and gadolinium[240]. Both were tested in the work of Daksh et al., in terms of photocatalytic activity, evaluating the efficiency in victoria blue degradation and in terms of the antibacterial activity against *S. Aureus*[240]. In both cases, increased performances were found with respect to pure ZnO.

The studies mentioned before highlight that doping is a valuable tool to enhance the antibacterial activity of ZnO nanoparticles. Both Gram-positive and Gram-negative bacteria appear to suffer the presence of doped nanoparticles since no particular differences are generally found in the two bacteria typologies. Moreover, the mechanism through which the doping can increase the toxicity against bacteria

appears slightly different among the various dopants. Many authors reported an increased photocatalytic activity which led to an increased ROS generation. In other cases, the increased bactericidal action was ascribed to a more efficient attachment of the nanoparticles to the cell membrane. The exact reason behind the improved antibacterial toxicity of doped ZnO nanoparticles is still unclear and further studies are required for each of the proposed dopants to assess the role of charge and the structural and electronic properties of doped ZnO on the antibacterial activity.

### 1.5.3 Nanotools for Photobioimaging

Pure ZnO has a wide band-gap of about 3.3 eV at room temperature and thus can only absorb UV light which is just 5% of the solar spectrum[241]. To improve the light absorption efficiency toward a more biologically-relevant visible-near infrared (vis-NIR) region, the modification of ZnO nanoparticles with impurities incorporated in the host lattice has been introduced. Actually, the stimulation of the photoluminescent response of doped ZnO NPs by using vis-NIR light, which does not damage tissues and organs, is expected to be particularly useful in bioimaging applications. Herein, to extend the emission range from the intrinsic band-gap of ZnO to the infrared region, doping with optically-active impurities like transition metals (TM) or rare earth (RE) elements has been reported even though TM and RE elements reveal different spectral properties[241]. For TMs, as the influence of the surroundings is stronger due to the weaker shielding of the 3d-shell by the 3s orbit, the spin-orbit coupling is weaker and the 3d-levels are broad. As a result, the energetic spacing varies with the host material and the electron–phonon interaction appears stronger than RE elements[242]. For RE elements, because of the strong shielding of the 4f-shell by the 5s2 and 5p6 orbits, the interaction with the surroundings is weak and almost all RE elements show intra-shell luminescence, i.e., the one least occupied, and unoccupied intra-shell levels are located in the band-gap of ZnO[242,243]. Thus, a very similar chemical behavior for all lanthanides in ZnO has been identified, whereas filling the d-shell in transition metals has a stronger influence on the outer shells and its bonding behavior in the ZnO lattice. To this end, there are various reports incorporating optically-active dopants in the ZnO lattice to change the band-gap value and increase the UV luminescence properties of pure ZnO[244–246]. Additionally, the optical parameters (band-gap) of the doped ZnO nanoparticles are summarized in Table 3. The band-gap values of the doped ZnO depend on several factors such as grain size, carrier concentration, lattice strain, size effect, oxygen vacancy and its related disorder-created localized defect states within the band-gap of ZnO, orbital hybridization between the dopant

and the host band, etc.[247,248]. Depending upon these factors, red shift behavior (or a decrease in the band-gap) and blue shift behavior (or an increase in the band-gap) have been reported by several research groups (Table 3).

**Table 3**: Doped ZnO: optical and magnetic properties.

| Ref. | Dopant | Dopant Concentration | Bandgap (eV) | Dopant Concentration | Saturation Magnetization (emu/g) |
|---|---|---|---|---|---|
| [249–251] | Cu | 0, 10% | 3.35, 3.30, respectively | 0.05–0.20 mol% | 0.011–0.063 |
| [182,252] | Fe | $Zn_{1-x}Fe_xO$ (x = 0, 0.01, 0.04, 0.05, 0.06) | 3.243, 3.236, 3.216, 3.197, 3.195, respectively | x = 0.20 | 1.74 |
| [253] | Cr | 0.00 to 4.63 at.% | from 3.26 to 3.15 | 2.49 at% | 4.86 |
| [177] | Co | 0, 5, 10 at% | 3.10, 3.17, 3.24, respectively | 5 at%, 10 at% | 1.42, 1.75 |
| [254–257] | Mn | 0, 3, 5, 10, 15 mol% | 3.31, 3.35, 3.38, 3.40, 3.42, respectively | 3.3 mol%, 4.2 mol% | 0.00123, 0.015 |
| [258] | Ni | $Zn_{1-x}Ni_xO$ (x = 0, 0.05) | 3.28, 3.32, respectively | x = 0.05 | 2.9–2.8 |
| [259,260] | Al | 0, 2 at.% | 3.07, 3.12, respectively | 0.03 at% | 0.012 |
| [140,261] | Mg | 0, 2.5%, 5%, 7.5% | 3.36, 3.27, 3.13, 3.04, respectively | 3% | $1.05 \times 10^{-3}$ |
| [262] | Nd | ZnO, $Zn_{0.97}Nd_{0.03}O$ | 3.34, 3.12, respectively | x = 0.03 | 0.67 |

| | | | | | |
|---|---|---|---|---|---|
| [263,264] | Sm | 0, 1, 3, 5 mol% | 3.27, 3.25, 3.10, 3.05, respectively | 0%–8% | 0.45, 0.363, 1.694, 3.613 and 2.197 emu/cm$^3$ |
| [265,266] | Eu | 0, 1, 3, 5 mol% | 3.18, 3.05, 3.00, 2.94, respectively | 10% | 0.040 |
| [267] | Tb | $Zn_{1-x}TbxO$ (x = 0, 0.02, 0.05, 0.1) | 3.35, 3.31, 3.30, 3.28, respectively | x = 0, 0.02, 0.05, 0.1 | 0.0042, 0.0276, 0.0359, 0.0519 |
| [119,268] | Gd | 0, 3, 6 % | 2.71, 2.74, 2.98, respectively | 1.1%, 3.5%, and 5.1% | 0.0001, 0.05, 0.0032 |
| [269,270] | La | 1, 5 wt% | 3.12, 3.18, respectively | 0, 1 mol% | 0.102, 0.232 |
| [271,272] | Ce | 0, 1, 3 and 5 at% | 3.21, 3.10, 3.08, 2.96, respectively | 0, 0.96, 1.96, 2.52 and 3.12 at.% | $1.895 \times 10^{-3}$, $31.612 \times 10^{-3}$, $26.818 \times 10^{-3}$, $26.136 \times 10^{-3}$, $23.608 \times 10^{-3}$ |

In recent years, diluted magnetic semiconductors (DMS) materials have attracted great research interest due to their potential combination of both semiconductive and magnetic properties. The application of ZnO-DMS, exploiting the electron charge associated with the intrinsic spin of the electron, has been noticed in spintronic devices [109,273]. It has been predicted in theory as well as proven in practice that ZnO nanoparticles doped with transition metals (TMs) or rare earth (RE) elements can result in a DMS material with a high Curie temperature, comprising ferromagnetic properties at room temperature[274–276]. The magnetic properties of TM or RE elements are implemented by the magnetic moments generated due to the presence of unpaired electrons in the outermost 3d or 4f orbital, respectively, although the nature of the magnetic moments of TM and RE elements are quite different. For instance, TMs have a small total magnetic moment per atom, as the outermost 3d electrons in TMs are exterior and delocalized, and their orbital momentum is frequently zero[274]. On the other hand, in RE elements, the peripheral

4f electrons are localized, having indirect exchange interactions among 5d or 6s conduction electrons. Therefore, RE elements can be expected to have a high total magnetic moments per atom owing to its high orbital momentum than that of TMs [115,277]. Various TMs such as Fe, Co, Cr, Mn, and Ni, and RE elements such as Eu, Tb, La and Gd have been exploited as dopants for creating doped ZnO NPs DMS. The magnetic parameters of the doped ZnO NPs are summarized in Table 3. Besides, there are few reports showing an enhanced ferromagnetism by exploiting Co-doped ZnO NPs[278–280]. The doped ZnO NPs can also be exploited as magnetic resonance imaging (MRI) contrast agents either to increase the signal intensity on T1-weighted images or to reduce the signal intensity on T2-weighted images[281–283]. Moreover, some research groups have reported Gd-doped ZnO quantum dots (QDs) as efficient dual modal fluorescence and MRI nanoprobes[165,284].

### 1.5.4 Doped ZnO ad Therapeutics against Cancer

ZnO nanoparticles present interesting properties useful for effectively fighting cancer as well. ROS generation and the ZnO particles dissolution are the main mechanisms responsible for cell and bacterial death. Therefore, it can be potentially toxic for tumoral cells.

For ZnO dissolution, the role of Fe doping as a stabilizer for the ZnO crystal lattice has been highlighted in Section 4.1, leading to a decreased dissolution rate of the nanoparticle. This has been proven to also inhibit tumoral cell growth. As a matter of fact, tumoral cells appeared to be more sensitive to the presence of ZnO than healthy ones[220,285]. By finely tuning the dissolution rate of ZnO nanoparticles with Fe doping, it was possible to reduce the toxicity to an optimal value so as to be harmful for cancer cells without damaging healthy cells[206]. The promising results obtained in in vitro tests gave the basis to perform a preclinical study on a rodent model for evaluating the antitumor response: pure 2 wt.% and 10 wt.% Fe-doped ZnO nanoparticles were tested in mice, finding again a reduced amount of free zinc ions being released, and a decreased tumor growth in the presence of the Fe-doped ZnO NPs. In particular, the tumor (KLN-205) was inoculated subcutaneously in mice and, after 10 days of treatment with pure ZnO NPs, mice displayed signs of toxicity to force the authors to stop the experiment with pure ZnO for ethical reasons. Figure 10 shows the growth of the tumor for the 2 wt.% and 10 wt.% Fe-doped ZnO NPs and the control (saline solution) treatments. As it can be seen in Figure 10, the 2 wt.% doped ZnO nanoparticles effectively inhibited the tumor growth, different to the control and the 10 wt.% doped ZnO NPs treatments.

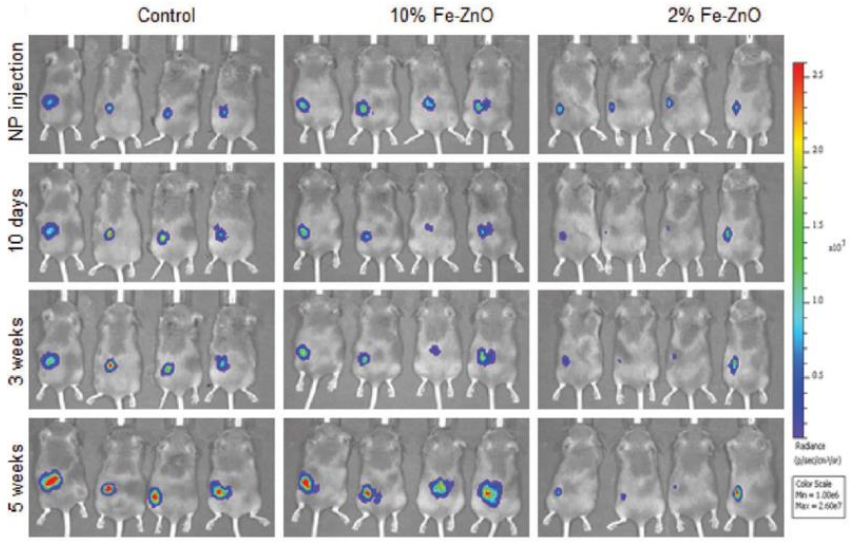


Figure 10: Tumor growth trend in mice at different times and differently doped ZnO nanoparticles. Tumor growth is reduced with 2% Fe-doped ZnO nanoparticles. Adapted from ref.[206].

Concerning ROS generation, ZnO NPs was successfully applied in photodynamic therapy. The idea behind this technique is to exploit the interaction between a photosensitizer (the semiconducting ZnO NP) and electromagnetic radiation in order to generate cytotoxic species (ROS) that kill cells and destroy tissues[286], with the mechanisms reported schematically in Figure 11. The photosensitizer should be internalized inside the cell and then exposed to light. By photoexcitation, it is possible to induce the electronic transition from the valence to the conduction band, which allows the formation of ROS, as already described in Section 4.2.

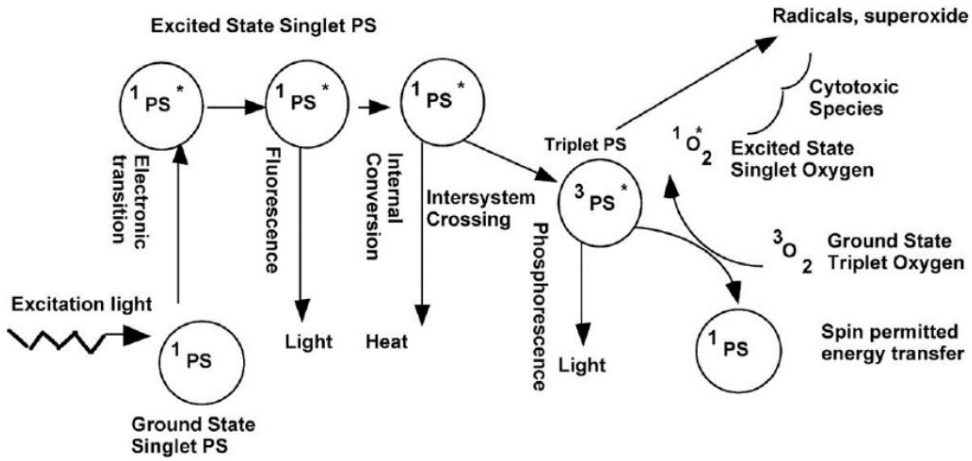


Figure 11: Photodynamic therapy mechanism. The photosensitizer (PS) is excited by external radiation, the excited electron may decay through different phenomena which may end in the generation of cytotoxic species. Adapted from ref.[286].

In the work of Hackenberg et al., the role of ZnO nanoparticles on the viability of tumoral and healthy cells was investigated[287]. Pure ZnO nanoparticles were tested on a human head and neck squamous cell carcinoma (HNSCC) cell line and on oral mucosa cells (pOMC). Different concentrations of ZnO NPs and the exposition time to UV light were explored on cell cultures internalizing the particles, and cell viability was evaluated through an MTT assay. The results showed that a high concentration (20 μg/mL) of nanoparticles reduced the viability for all the cells (~70 % of the survival percentage without UV exposure), while lower concentrations (up to 2 μg/mL) resulted in more toxicity toward cancerous cells when coupled with longer times of UV exposure (at a 2 μg/mL concentration of NPs and 15 minutes of UV exposure, ~40% of the survival percentage for cancerous cells vs. 90 % for normal cells). Even if the exposure to UV light highlighted the important role played by the photocatalytic activity of ZnO NPs against cancer cells, the cytotoxicity observed at high concentrations in the absence of UV exposure also suggested the presence of a secondary mechanism.

ZnO nanoparticles for photodynamic therapy were investigated also by Ancona et al.[93]. In this case, ZnO particles were coated by a lipid layer in order to increase the dispersion of the nanoparticles in biological media and to improve cellular uptake, and were then tested as photosensitizers against human epithelial carcinoma cells (HeLa). The lipid-coated nanoparticles were successfully internalized in the cells and an increased cytotoxicity was found with an increase of the concentration

of NPs coupled with UV irradiation, confirming the interesting antitumoral properties of bare ZnO.

In the previous sections of this review, several works reporting an increased photocatalytic activity of doped ZnO nanoparticles were described. This aspect can be extremely useful in enhancing NPs cytotoxicity against tumoral cells, in a similar manner to what has been demonstrated for antimicrobial applications.

Lithium-doped ZnO nanoparticles were proposed as generators of singlet oxygen for this purpose[146]. A physical characterization of these nanoparticles was provided, reporting an increase of the band-gap energy and a slight blue shift of the exciton energy. Moreover, an increased generation of singlet oxygen was clearly observed for the increasing doping levels, suggesting its use in photodynamic therapy.

In this sense, gadolinium and europium were also considered. In the work by Ghaemi et al., these two chemical species were proposed as dopant ions in ZnO nanoparticles and their influence was analyzed in terms of their cytotoxic behavior against normal (L929 fibroblast cells) and tumoral (Hela cervical cancer cells and PC3 prostate cancer cells) cells[166]. In particular, Gd- and Eu-doped ZnO NPs were internalized into cells and the cell cultures were exposed to UV, X-ray and γ radiations. Then, the cells viability was evaluated by an MTT assay, giving the results reported in Figure 12. In dark conditions, the NPs only slightly decreased the cells' viability with the increase of the concentration, demonstrating that Gd- and Eu-doped ZnO nanoparticles did not induce considerable cell death. However, when UV exposure was considered, the cells viabilities heavily reduced for all the doped and undoped-treated cell cultures, suggesting the importance of the photoexcitation of the ROS production. Another important aspect was a remarkable selectivity in killing only cancerous cells if intermediate concentrations of doped ZnO particles (10 μg/mL) were used. Cell lines incubated with ZnO NPs were also exposed to X-rays and γ-rays. While γ-rays did not give important changes in the viability of cells with respect to dark conditions, X-rays at 2 Gy were extremely effective at killing cells, with doped ZnO NPs in particular, perhaps because of a higher ROS generation.

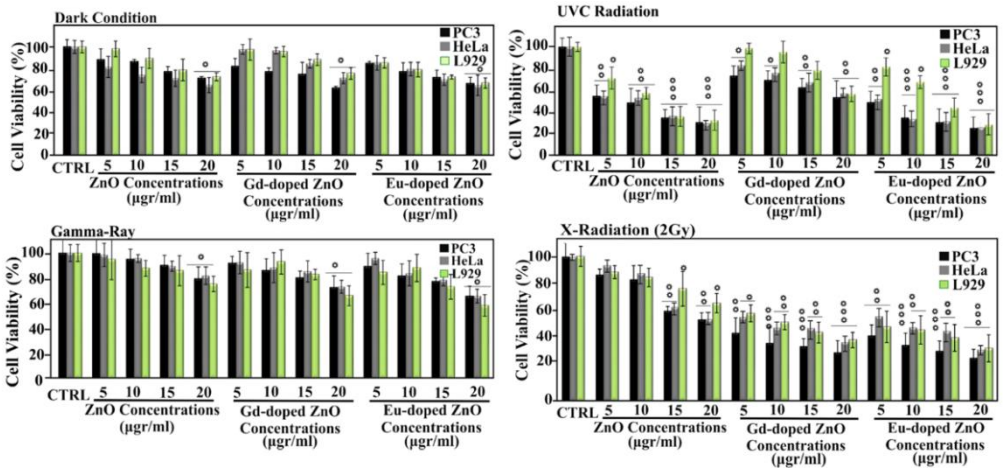


Figure 12: Cell viability of different cell lines exposed to different illumination sources and different concentrations, incubated with pure, Gd-doped and Eu-doped ZnO nanoparticles. Adapted from ref.[166].

Gadolinium doping coupled with X-ray radiation was tested also in another study, where Gd-doped ZnO nanoparticles were administered to lung carcinoma cells (SKLC-6) and irradiated with megavoltage X-rays[288]. Nanoparticles with a dimension of 9 nm were successfully internalized in the cell bodies as shown in Figure 13. A dose-dependent effect under X-rays irradiation was observed also in this case; the cells viability decreased when the NPs concentration was increased, reaching ~20% of cell viability with respect to the control at 100 μg/mL of the NPs concentration, as well as a reduction in the DNA repair efficiency.

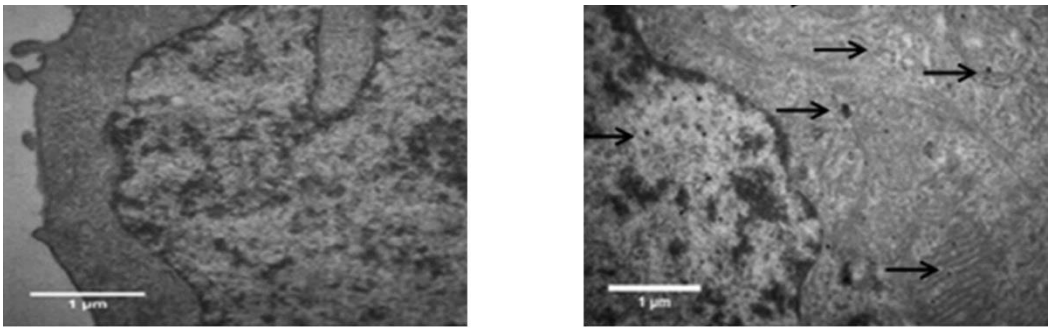


Figure 13: TEM images showing the internalization of pure (a) and Gd-doped (b) ZnO nanoparticles in lung carcinoma (SKLC-6) cells. Adapted from ref.[288].

Additionally, Mg-doped ZnO nanoparticles were proven to induce cell death in human breast cancer cells (MCF-7), and AO & EB staining coupled with

fluorescence microscopy showed that the main way through which cell died was apoptosis[168].

Cu-doped ZnO nanoparticles synthesized by a green method demonstrated similar anticancer properties[238]. The comparison on the cell viability between pure ZnO NPs, Cu-doped ZnO NPs and doxorubicin showed superior cytotoxic effects of the doped NPs against breast cancer cells. The proposed mechanism for cell death was the penetration of the small particles through the cell barrier.

Despite ZnO being already proposed as a therapeutic agent against cancer, doped ZnO nanoparticles still do not have a large literature pool through which the mechanism of toxicity can be stated univocally. Many studies have reported an increased cytotoxicity in concomitance with increased photocatalytic and antibacterial activities. Other works focused on the stability of the ZnO particle to tune specifically the antitumoral effect. Even if further studies are required, the results herein described clearly show that doped ZnO can be a powerful weapon to fight cancer.

## 1.6 Conclusions

In summary, doping represents a valuable tool to extend the use of ZnO NPs in nanomedicine. Wet chemistry approaches based on sol-gel, hydrothermal routes and combustion methods have been largely used to dope ZnO NPs with various elements including rare earth (REs) elements and transition metals (TMs). It is found that RE elements have been more extensively considered to improve the photocatalytic and optical properties, but also to confer on ZnO NPs magnetic and improved electromechanical behaviors. Overall, doping ZnO NPs with TMs was mainly considered to give ZnO unprecedented ferromagnetic properties.

Doped ZnO NPs have been successfully proposed as therapeutic agents against cancer and showed enhanced antibacterial properties against both Gram-positive and Gram-negative bacteria. The mechanism through which doping can increase ZnO NPs toxicity against cancer cells and bacteria is still controversial and not univocally stated. In some cases, it was ascribed to the improved photocatalytic activity and increased generation of harmful ROS. In other cases, the increased bactericidal action was due to a more efficient attachment of the nanoparticles to the cell membrane. Even if further studies are required, the results described herein clearly highlight that doped ZnO NPs can be a powerful weapon to treat cancer. Doping ZnO NPs with TMs also represents a powerful approach to acquire new bioimaging properties which have been successfully applied to magnetic resonance

imaging applications. Promising results were also found in terms of an increased cytocompatibility by using Fe-doped ZnO nanoparticles due to the reduced and even more controllable release of cytotoxic zinc cations. Therefore, the iron has been chosen as doping element for the ZnO NPs object of this work.

# Chapter 2

# Fe:ZnO NPs synthesis and characterization

Part of this chapter has been taken from the open-access publication "Carofiglio, M.; Laurenti, M.; Vighetto, V.; Racca, L.; Barui, S.; Garino, N.; Gerbaldo, R.; Laviano, F.; Cauda, V. *Iron-Doped ZnO Nanoparticles as Multifunctional Nanoplatforms for Theranostics*. Nanomaterials 2021, 11, 2628".[101]

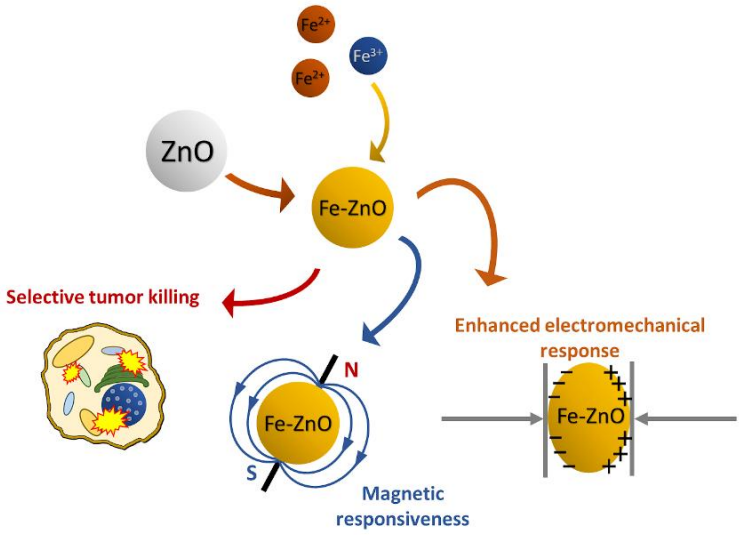


Figure 14: Graphical summary of the chapter. The aim of this part of the work is to obtain a ZnO NP that presents features exploitable for theranostics: selective tumor toxicity, magnetic responsiveness and enhanced electromechanical response[101].

## 2.1 Introduction

Novel therapeutic approaches based on the use of smart nanomaterials are considered the frontier in the development of next-generation, multifunctional nanosystems aimed for nanomedicine. Examples include theranostic nanoparticles (NPs), i.e. nanosystems capable of combining therapeutic and diagnostic functionalities, to deliver and activate a therapeutic agent towards a specific position inside the body, and to report the status of the disease and/or of the therapeutic agent at the same time[289].

One of the main and most appealing application of theranostics is surely for anti-tumoral purposes[290]. Indeed, the possibility to exploit both imaging capabilities and a therapeutic action of the theranostic agent in the human body, as well as to guide it toward the specific site of interest, gathers relevant advantages in terms of personalized medicine, allowing the application of a customized therapy and real-time diagnosis solely for the targeted organ or tissue.

In this regard, the study of theranostic nanoparticles gained relevant attention. Thanks to the reduced size, NPs represent one of the most suitable systems compatible with the cellular dimensions. This aspect also efficiently combines with the superior physical and chemical properties of NPs due to quantum-size effects typical of nanometer-sized materials, which can be also customized depending on the nanomaterials shape and on the selected class of material (metal, semiconductor, etc…). NPs also show passive tumor targeting, active targeting possibilities[27], as well as promising imaging potentialities[25]. Therefore, these aspects corroborate the use of NPs as optimal and versatile platforms to be employed for various therapeutic applications, including drug delivery[291], and stimuli-responsive ones, i.e. hyperthermia[292], photodynamic[93,232] or sonodynamic therapies[94,293,294]. As already extensively reported in Chapter 1, in the specific class of metal oxides, ZnO NPs are surely promising candidates and have been already proposed for nanomedicine[71,91,285]. First of all, ZnO NPs are extremely versatile in terms of existing techniques for NPs' preparation and of the resulting nanoparticle morphology, making easier the tailoring of the NP system for specific theranostic applications[71]. Moreover, ZnO NPs present very interesting optical properties, which have been proven to impart a photocatalytic activity and in turn, promising antimicrobial behaviors[295].

ZnO is also a well-known piezoelectric material. Piezoelectric NPs have been already explored in nanomedicine either as powerful system for tissue engineering[296,297] or as promising anticancer therapeutic[218]. Both these antithetic

approaches rely their efficacy on the interference that electrical stimuli, generated by the mechanically-activated piezoelectric NPs, may induce on cell ions homeostasis. If opportunely tuned, this interference may lead to cells differentiation or to cell anti-cancer drug sensitization. Based on the above-mentioned mechanism, ZnO piezoelectricity has been successfully exploited to develop several smart ZnO-based materials for tissue engineering applications[71,298].

From the therapeutic standpoint, it has also been demonstrated that ZnO NPs can act as sensitizing agents in photo- and sonodynamic therapy. Thanks to the enhanced reactive oxygen species generation when exposed to light[93] or mechanical stimuli[299], ZnO NPs are effective in killing cancer cells when coupled with ultraviolet (UV) light radiation or shock waves[94].

However, ZnO NPs on their pure form present some criticalities that should be considered in view of their translation to clinically-relevant applications. The most important one is their toxicity. As a matter of fact, despite being considered GRAS (Generally Recognised as Safe) in its bulky form by the Food and Drug Administration, nanosized ZnO demonstrates a dose dependent toxicity[300] which can be related to three main processes: (i) the release of zinc cations due to NP dissolution in biological media, which may lead to the disruption of the cell homeostasis[301]; (ii) the induced generation of cytotoxic reactive oxygen species by either photocatalysis or by sono-irradiation[90]; and finally, (iii) the mechanical damages that the NP could induce on the cell membrane during internalization[295]. Moreover, ZnO on its own is a wide band-gap semiconductor (approximately 3.4 eV[69]) and it can only absorb light in the UV region of the spectrum, thereby limiting its use as photo-sensitizing agent for photo-dynamic therapy. Indeed, ZnO NPs are able to generate ROS under photo-irradiation and kill tumoral cells only when exposed to UV light, which is however harmful also for healthy cells.

Therefore, both the therapeutic efficacy and the imaging abilities of ZnO NPs need to be properly optimized to account for the use of small and safe doses of the theranostic nanoparticles. As already reported in Chapter 1, doping ZnO NPs represents a valuable manner to optimize the material to fit the requirements for an effective theranostic NP.

In particular, among the various doped ZnO nanomaterials, the iron doped ones play a relevant role in the biomedical field. Indeed, it has been proven that Fe doping reduces the dissolution rate of ZnO nanoparticles in several biological media, hence representing a valuable approach to partially prevent undesirable cytotoxic effects against healthy cells[207]. Despite Fe:ZnO nanomaterials being already reported in the literature, to the best of our knowledge, a comprehensive

study focusing on the corresponding optical, piezoelectric, magnetic and biocompatible properties aimed at theranostics has not been reported yet.

Therefore, the aim of this thesis is to develop multifunctional iron-doped ZnO nanoparticles (Fe:ZnO NPs) thought as theranostic nanoplatforms that can be introduced safely inside the cell and that present intrinsic imaging and therapeutic potentialities to fight cancer cells.

For this purpose, Fe:ZnO NPs incorporating two different dopant amounts (6 and 12 at.%) were synthesized with a wet chemical synthesis technique using oleic acid as capping agent to stabilize the nanoparticles system in aqueous media. A further functionalization with amino-propyl groups was performed with a post-synthetic grafting approach for further dye labelling and increase the Z-potential value for improved stability in water media. In a similar way, undoped ZnO NPs were prepared as well, and used as reference to state the improved properties obtained in case of the doped Fe:ZnO NPs counterpart. All the NPs were investigated in terms of morphology and crystallographic structure to assess the distortion that doping induces on the ZnO crystal lattice. The chemistry of the NPs was investigated by spectroscopic techniques to define the amount of doping level and Fe oxidation state, as also to verify the correct functionalization of the NPs.

The nanoparticles were analyzed in terms of optical properties, electromechanical and magnetic behaviors, to establish the improved performances of the doped particles with respect to the undoped ones. Indeed, Fe doping gathers magnetic responsiveness to doped particles which could be used in magnetic resonance imaging. Moreover, by changing the amount of the inserted dopant, substitutional Fe ions with different radii and oxidation states relative to $Zn^{2+}$ one were noticed, finally influencing the electromechanical response of the doped NPs.

In this perspective, the results here obtained allow to propose a nanosystem in which the novel properties gathered by doping, i.e. luminescence, magnetism and piezoelectricity, can be fruitfully exploited for theranostics applications.

## 2.2 Materials and methods

### 2.2.1 ZnO and Fe:ZnO NPs synthesis procedure

Undoped and iron-doped zinc oxide nanoparticles (ZnO and Fe:ZnO NPs) were synthesized by a wet chemical process, exploiting oleic acid as stabilizing agent[120].

More in detail, for ZnO NPs, 526 mg of zinc acetate dihydrate ($Zn(CH_3COO)_2 \cdot 2H_2O$, ACS Reagent, ≥99.0%, Sigma-Aldrich, Darmstadt, Germany) was dissolved in 40 mL of ethanol (99%, Sigma-Aldrich). The ethanolic solution was placed in a 100 mL round-bottom flask. Then, 1 mL of bidistilled water (obtained from a Direct Q3 system, Millipore) and 140 μL of oleic acid (≥99 %, Sigma-Aldrich) were added to the solution.

The flask was placed in a silicon oil bath to be heated up to 70 °C in refluxing conditions.

In the meanwhile, 1.044 g of tetramethylammonium hydroxide pentahydrate (TMAH, 98.5 %, Sigma-Aldrich) was dissolved in 10 mL of ethanol and 1.052 mL of bidistilled water. The TMAH solution was rapidly poured to the main solution, after 10 minutes of moderate stirring at 70°C.

After further 10 minutes, during which the clear solution turned into an opaque particle dispersion, 40 mL of ice-cooled ethanol was included in the solution to stop the reaction. The flask was then placed in an ice bath for 3 minutes.

The resulting NPs were washed twice by centrifugating them at 8000 g for 10 minutes and then re-suspended in ethanol.

Similarly, Fe:ZnO NPs were obtained by including 58 or 116 mg of ferric nitrate nonahydrate ($Fe(NO_3)_3 \cdot 9H_2O$, HiMedia) for 6 at.% (Fe6:ZnO) and 12 at.% (Fe12:ZnO) doped nanoparticles, respectively, in the zinc acetate ethanolic solution.

### 2.2.2 ZnO and Fe:ZnO NPs functionalization procedure

Amino-propyl functionalization of the undoped and iron-doped ZnO nanoparticles was carried out prior to in vitro biological tests, following the procedure described by some of us[75]. In particular, 40 mg of NPs were dispersed in ethanol to obtain a 2.5 mg/mL dispersion. Then, the dispersion was placed in a 25 mL round bottom flask and heated up to 70 °C in refluxing conditions, under moderate stirring and continuous gaseous nitrogen flux. After 10 minutes, 10 mol% of 3-aminopropyltrimethoxysilane (APTMS) was added to the nanoparticles' dispersion. The system was kept in nitrogen atmosphere and continuous stirring for 6 hours and then washed two times with ethanol by a centrifugation and redispersion process (14000 g for 10 minutes).

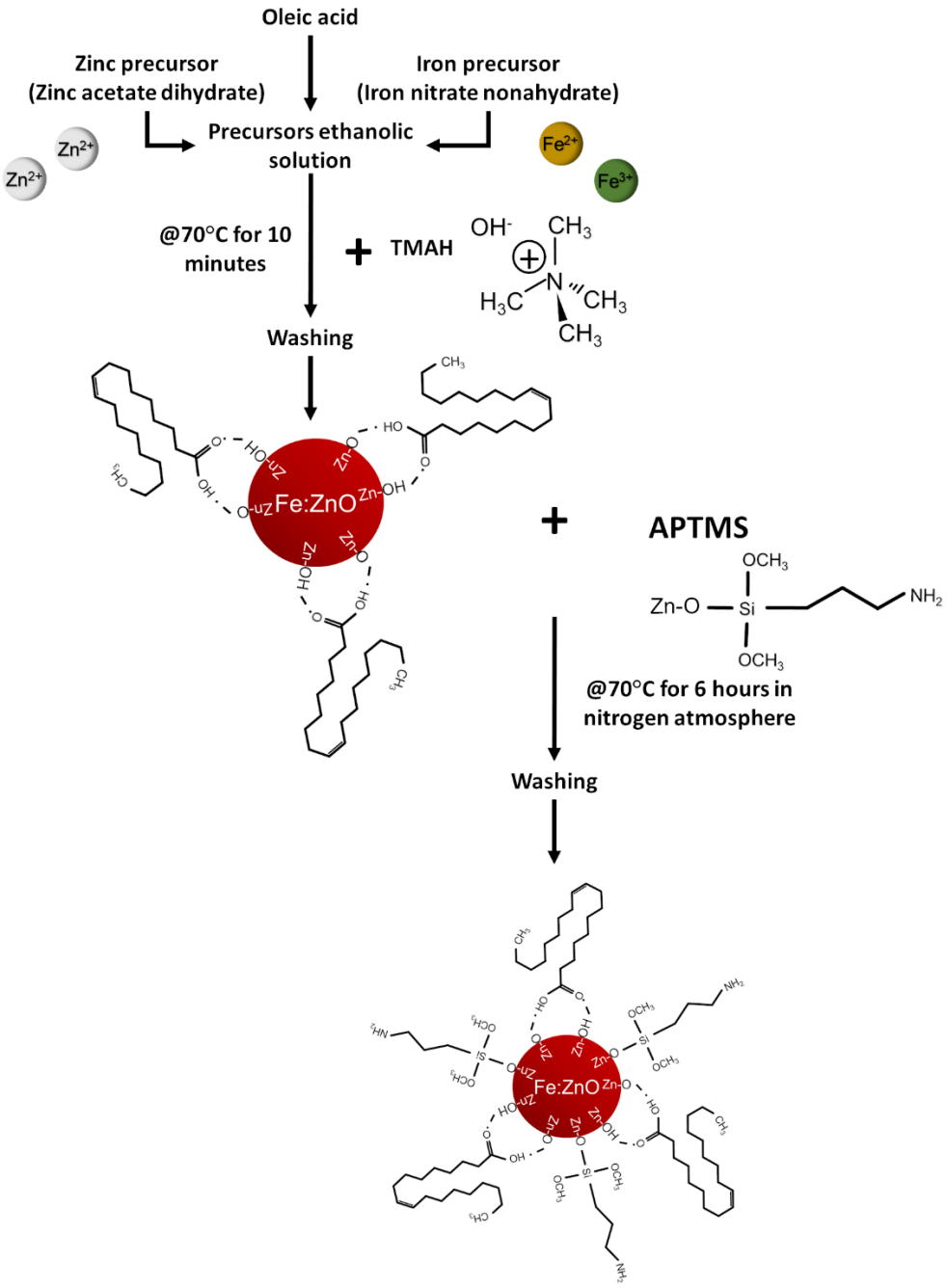


Figure 15: Iron-doped ZnO NPs synthesis and functionalization diagram .

### 2.2.3 Physico-chemical characterization

The morphology and chemical composition of the prepared materials deposited onto a silicon substrate were characterized by Field Emission Scanning Electron Microscopy (FESEM, SUPRA 40 from Zeiss) coupled with a detector for energy dispersive X-ray spectroscopy (EDS).

Also, Transmission Electron Microscopy (TEM) analysis was employed for their analysis. The observed samples were prepared by dispersing the NPs in water at a concentration of 25 μg/mL. Then, 10 μL of the solution were deposited onto a Lacey Carbon Support Film (300 mesh, Cu, Ted Pella Inc.) and let dry. The measurements were held with a Talos™ F200X G2 S(TEM) from Thermo Scientific at an operating voltage of 200 kV.

Fourier Transform Infrared (FT-IR) spectroscopy was performed in transmission mode on 500 μg of ZnO and Fe:ZnO NPs deposited onto a silicon wafer prior and after functionalization, in the region 4000-400 $cm^{-1}$ range with a Nicolet 5700 FT-IR spectrometer (Thermo Fisher).

The crystallinity of the synthesized nanoparticles was investigated by X-Ray diffraction (XRD) analyses, through a Panalytical X'Pert diffractometer in θ-2θ Bragg-Brentano mode (Cu-Kα radiation source, λ=1.54 Å, 40 kV and 30 mA) on samples prepared similarly to the ones exploited during FT-IR measurements. The evaluation of the peak shift was performed by fitting the peaks with a Gaussian function (Origin, OriginLab) and comparing the evaluated peak positions for the three main reflections. The same fit was exploited to determine the crystallite dimension (D) according to Debye-Scherrer formula[302] [38]:

$$D=(180\cdot\kappa\cdot\lambda)/(\pi\cdot\Delta 2\theta\cos(\theta)) \quad (1)$$

where κ=0.89, λ is the X-ray radiation wavelength, Δ2θ is the Full Width at Half Maximum (FWHM) expressed in radiant and θ is the diffraction angle.

X-ray Photoelectron spectroscopy (XPS) was carried out with a PHI 5000 VersaProbe (Physical Electronics) system. The X-ray source was a monochromatic Al Kα radiation (1486.6 eV energy). The relative atomic concentration (at.%) of each chemical element was calculated from the high-resolution (HR) spectra. XPS spectra were analyzed using CasaXPS software (version 2.3.18). All the XPS spectra were processed after Shirley background subtraction. HR core-level spectra deconvolution into individual mixed Gaussian–Lorentzian peaks was obtained after binding energy (BE) calibration according to C1s position for adventitious carbon (284.8 eV).

Dynamic Light Scattering (DLS) and Z-potential measurements were performed to evaluate the size and surface charge of nanoparticles. To this purpose, nanoparticles suspensions at the concentration of 100 μg/mL were prepared after 10 minutes of sonication in ethanol, water and cell culture medium (RPMI 1640, ATCC, supplemented with 10%v of Fetal Bovine Serum (ATCC) and 100 μg/mL streptomycin and 100 units/mL penicillin (P/S, Sigma-Aldrich)). DLS measurements were performed to determine the hydrodynamic radius of the particles both in their storage solvent (ethanol), in the aqueous medium (water) and in the medium exploited for cell culturing. Furthermore, Z-potential measurements were performed in water to investigate the surface charge of the nanoparticles.

The optical absorption properties of ZnO and Fe:ZnO nanoparticles in the ultraviolet and visible region of the light spectrum were evaluated in transmission mode through a double-beam Varian Cary 5000 UV-vis-NIR spectrophotometer. More in detail, ethanolic solution containing 2 mg/mL of ZnO and Fe:ZnO NPs were prepared and placed in quartz cuvettes (350 μL volume, 1 mm optical path length). The analysis was performed, using a pure ethanol sample as baseline curve. All the spectra were thus background subtracted. From the UV-recorded spectra, the optical band gap of the nanoparticles was estimated according to Tauc's plot.

Fluorescence excitation and emission spectra were measured with a Perkin Elmer LS55 fluorescence spectrometer. ZnO nanoparticles were suspended in ethanol at a concentration of 1 mg/mL and placed in quartz cuvettes.

A DC magnetic characterization was performed on ZnO and Fe:ZnO NPs. To avoid any movement of the NPs during the application of a large magnetic field, 1 mg of NPs was encapsulated into 100 μL of DurcupanTM ACM and thermally treated at 60°C for 3 days to harden the resin. Measurements were then performed on these samples at room temperature and quasi-static conditions with a DC magnetometer (Lake Shore 7225, Lake Shore Cryotronics, Inc., Westerville, OH, USA) equipped with a cryogen-free magnet system.

The electromechanical response of ZnO and Fe:ZnO nanoparticles was evaluated by a Piezo Evaluation System (PES, TFAnalyzer 2000HS, Aixacct). The nanoparticles suspension (3 mg dispersed in 200 μL of bidistilled water) was deposited on conductive Au-$SiO_2$ substrate. After solvent evaporation, a continuous nanoparticles film could be formed. Measurements were performed under the application of a triangular excitation signal (voltage amplitude ±20 V, frequency 100 Hz).

## 2.3 Results and discussion

### 2.3.1 Structural and morphological characterization

The morphology of the ZnO and Fe:ZnO NPs was investigated by FESEM analysis. As shown in Figure 16, the resulting particles are almost spherical and present a dimension between 4 and 10 nm. No particular differences are found in the morphology and dimension between undoped and Fe-doped NPs, differently to what typically reported in the literature[207], in which a reduction of the dimension is acknowledged because of doping. The maintenance of size and morphology reported here may be attributed to a preponderance of the steric effects of the reagents exploited in our synthesis procedure, rather than a possible effect that doping may have on the rate of NPs nucleation and crystal growth.

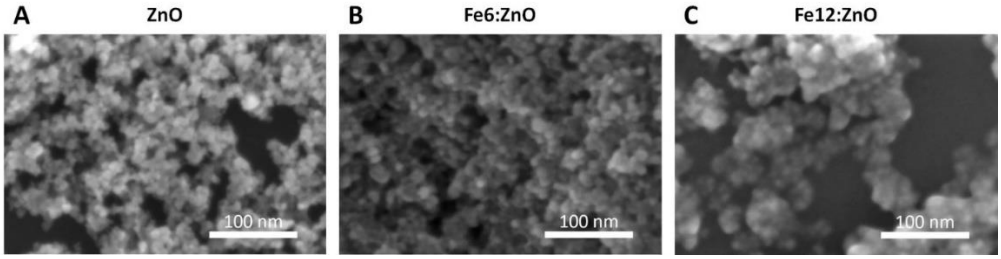


Figure 16: Field emission scanning electron microscopy images of ZnO (A), Fe6:ZnO (B) and Fe12:ZnO (C) nanoparticles having 0, 6, 12 at% of nominal iron doping respectively.

Another important point that arises from this analysis is the narrow size distribution of the nanoparticles. Independently of the level of doping, very uniform particle shapes and dimensions are observed. This aspect is further corroborated by DLS results discussed below.

EDS analyses were performed on Fe:ZnO nanoparticles to assess the actual level of iron incorporated in the nanoparticles (Figure 17). As it can be clearly observed from Table 4, by increasing the amount of the iron precursor during the synthesis, the atomic percentage of iron included in the NPs increases accordingly. In particular, the ratios between iron at.% and the sum of the iron and zinc at.% ($Fe_{at\%}/(Fe_{at\%}+Zn_{at\%})$ is equal to 4.8% and 7.8% for the Fe6:ZnO and Fe12:ZnO NPs, respectively. These results demonstrate that iron has been successfully included in the NPs system, and that the Fe doping level can be controlled by the synthetic procedure.

Among others, the high level of oxygen is instead attributed to the presence of organic species in the system, i.e. the oleic acid used to stabilize the nanoparticles.

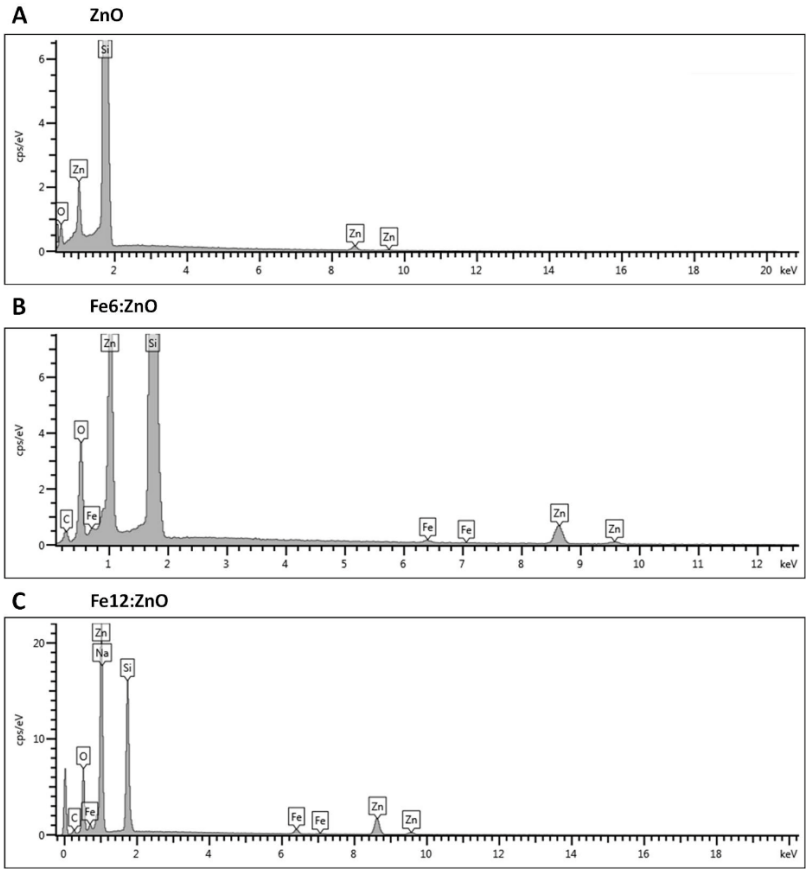


Figure 17: Field emission scanning electron microscopy images of ZnO (A), Fe6:ZnO (B) and Fe12:ZnO (C) nanoparticles having 0, 6, 12 at% of nominal iron doping respectively.

**Table 4**: Electron energy dispersive spectroscopy (EDS) results of Fe:ZnO nanoparticles. Here, only the results related to the Zn, Fe and O elements are considered.

| Sample | Zn [at. %] | Fe [at. %] | O [at. %] |
|---|---|---|---|
| ZnO | 18.65 | - | 81.35 |
| Fe6:ZnO | 23.68 | 1.20 | 74.82 |
| Fe12:ZnO | 22.70 | 1.90 | 75.4 |

Further electronic microscopy analyses on pure ZnO and Fe6:ZnO NPs were performed through a TEM analysis in which some of the nanocrystals can be recognized (Figure 18).

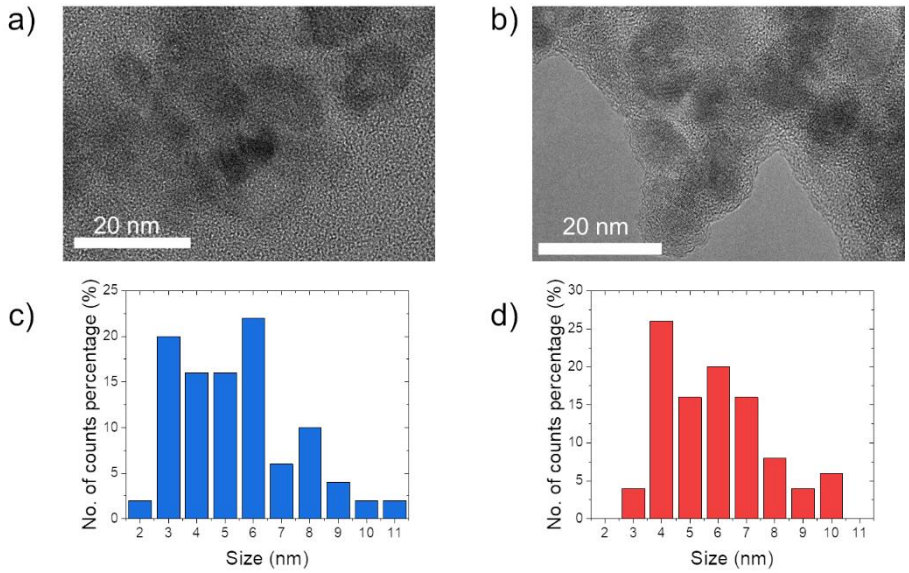


Figure 18: Transmission electron microscopy images of a) ZnO and b) Fe6:ZnO NPs having 0, 6 at.% of nominal iron doping respectively. Nanoparticles diameter size histograms of c) ZnO and d) Fe6:ZnO NPs.

From the nanocrystals recognition it is possible to assess that the formed NPs are monocrystalline and determine the spacing between the crystal planes forming the crystal. The measurement of the spacing leads to 2.81±0.30 Å and 2.74±0.25 Å for ZnO and Fe6:ZnO NPs respectively. The NPs size distribution confirms the good homogeneity of the synthesized NPs and evidences the absence of any significant difference in size and morphology of the differently doped NPs. As a final remark on the TEM images, it is possible to spot the presence of an organic layer surrounding the NPs, which could be possibly attributed to the oleic acid capping and to the amino-propyl functionalization.

Fourier transform infrared spectroscopy was carried out to verify the presence of the oleic acid functional groups on the nanoparticles and to check the correct amino functionalization, required to label the nanoparticles for biological tests and increase the stability of the nanoparticle.

In Figure 19, the spectra retrieved for the functionalized ZnO and Fe:ZnO NPs are reported. Despite the different doping levels, the Fe:ZnO NPs show several common features. First of all, there is an intense peak centered at ~440 $cm^{-1}$, which

can be related to the vibration of Zn-O bonds. Moreover, two peaks at ~1420 and ~1570 $cm^{-1}$ can be attributed to the C-O and C=O vibrations respectively, while the peaks at ~2860 and ~2925 $cm^{-1}$ are assigned to the $-CH_3$ and $-CH_2$ symmetric and asymmetric stretching vibrations. The presence of these peaks is expected because of the inclusion of oleic acid in the system, the amino-propyl functionalization and the use of zinc acetate in the synthesis procedure, which may result in some acetate residual. Finally, the broad band found between 3200 and 3600 $cm^{-1}$ is ascribed to the OH stretching vibration. The abundance of hydroxyl groups useful for promoting the anchoring of functional moieties on the NPs outermost surface is evident for both the amino-propyl functionalized and unfunctionalized NPs (Figure 20), witnessing how these NPs are prone to be functionalized without requiring any further surface activation steps.

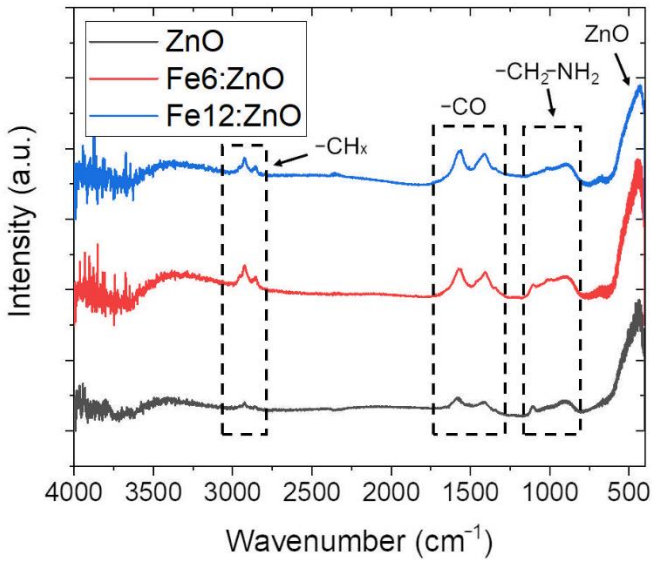


Figure 19: Fourier transform infrared spectroscopy spectra of ZnO, Fe6:ZnO and Fe12:ZnO NPs after ami-no-propyl functionalization.

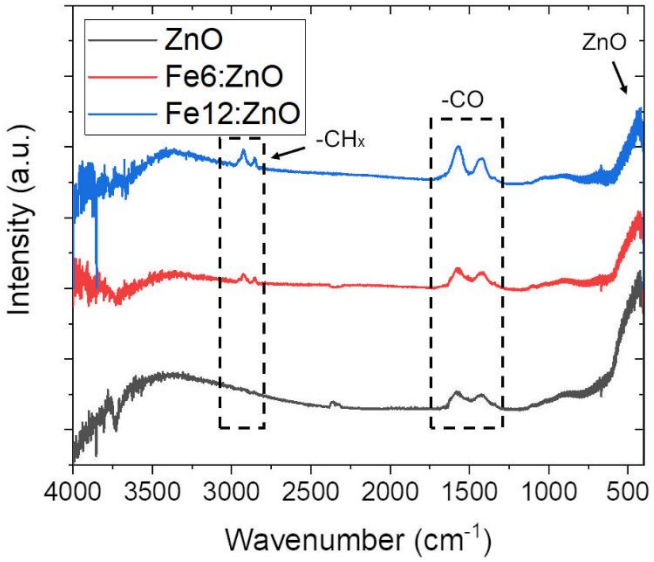


Figure 20: Fourier transform infrared spectroscopy spectra of ZnO, Fe6:ZnO and Fe12:ZnO NPs prior amino-propyl functionalization.

The effectiveness of amine functionalization is corroborated by the presence of a small but sharp peak in the region between 1100 and 750 $cm^{-1}$, which is attributed to primary aliphatic amines ($-CH_2-NH_2$)[303]. This peak is no longer visible in the IR spectra of the non-functionalized NPs (Figure 20).

Further insights about the composition of the prepared NPs were obtained by X-Ray Photoelectron Spectroscopy (XPS). The wide-energy range analysis for the undoped ZnO NPs revealed the presence of Zn, C, O, and N (Figure 21a). Additionally, Fe element was detected only for the doped NPs (Figure 21b,c). The detection of N1s signal for all the NPs, i.e. undoped and doped ones, confirms the successful amine functionalization. On the other side, the detection of Fe only for Fe:ZnO NPs was expected and highlights the success of the synthetic method for incorporating Fe dopant within ZnO NPs.

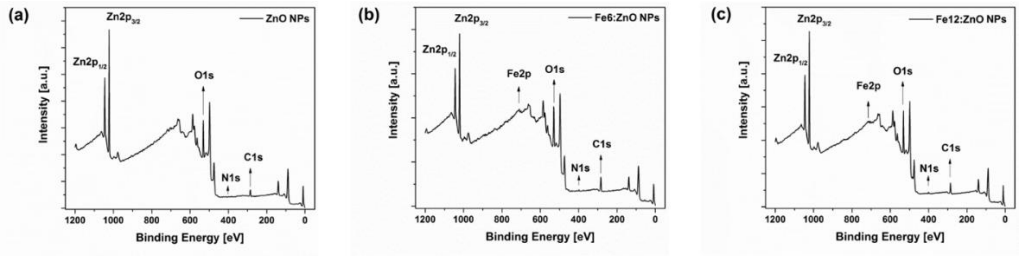


Figure 21: Wide-energy range XPS spectra for undoped ZnO (a), Fe6:ZnO (b) and Fe12:ZnO (c) NPs.

The relative atomic concentration (at.%) of each chemical element (Table 5) was estimated from the corresponding high-resolution (HR) spectra shown in Figure 22-24. The high presence of carbon is associated to the use of oleic acid in the synthesis process and to some contamination due to air exposure of the samples. Despite the amount of iron incorporated in the ZnO NPs being lower than the EDS data of Table 4, the ($Fe_{at\%}$/($Fe_{at\%}$+$Zn_{at\%}$) ratio estimated from XPS results is similar and equal to 5.7% and 8.3% for Fe:ZnO NPs doped at the nominal levels of 6 and 12 at.%, respectively.

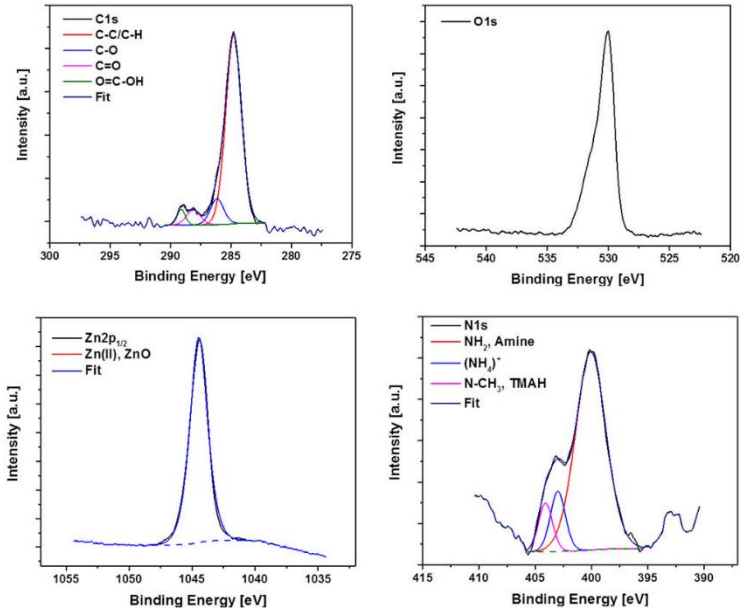


Figure 22: High-Resolution XPS spectra for undoped ZnO NPs.

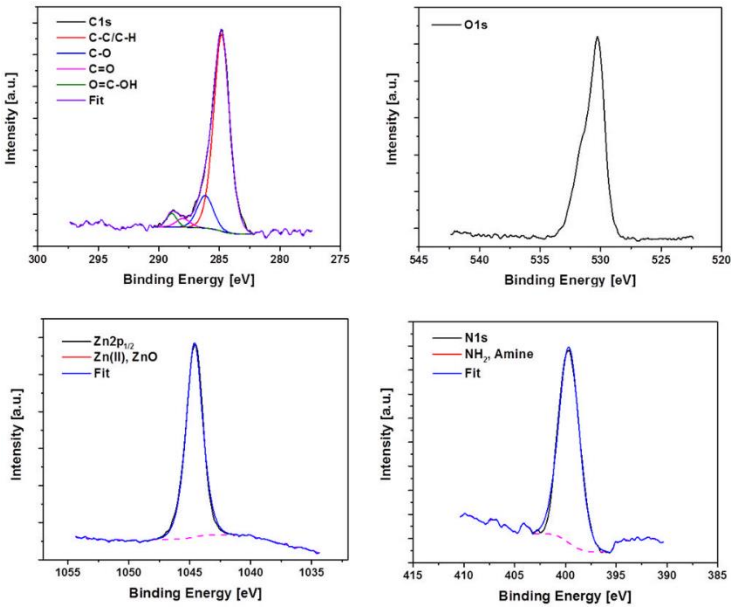


Figure 23: High-Resolution XPS spectra for Fe6:ZnO NPs.

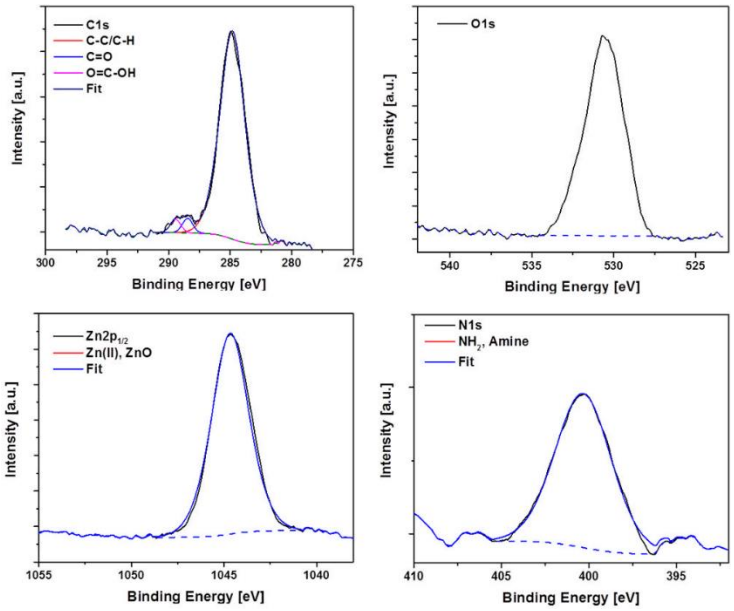


Figure 24: High-Resolution XPS spectra for Fe12:ZnO NPs.

**Table 5**: Relative atomic concentration for ZnO and Fe:ZnO nanoparticles estimated from HR-XPS analysis.

| Sample | C [at. %] | Zn [at. %] | O [at. %] | N [at. %] | Fe [at. %] |
|---|---|---|---|---|---|
| ZnO | 14.8 ± 0.5 | 39.3 ± 0.4 | 43.7 ± 0.4 | 2.2 ± 0.4 | - |
| Fe6:ZnO | 24.3 ± 0.5 | 29.8 ± 0.3 | 41.8 ± 0.4 | 2.3 ± 0.3 | 1.8 ± 0.3 |
| Fe12:ZnO | 28.1 ± 0.6 | 27.8 ± 0.3 | 38.8 ± 0.4 | 2.8 ± 0.4 | 2.5 ± 0.4 |

The local chemical environment of Fe dopant was further analyzed by collecting the high-resolution (HR) XPS spectrum of Fe2p, which is shown in Figure 25. The presence of multiple peak splits of Fe2p into separate components $Fe2p_{3/2}$ and $Fe2p_{1/2}$ is observed, which are centered at about 711 eV and 723 eV, respectively. Additional satellites in the 715-719 eV and 730-735 eV regions are also present and suggest the existence of multiple Fe oxidation states.

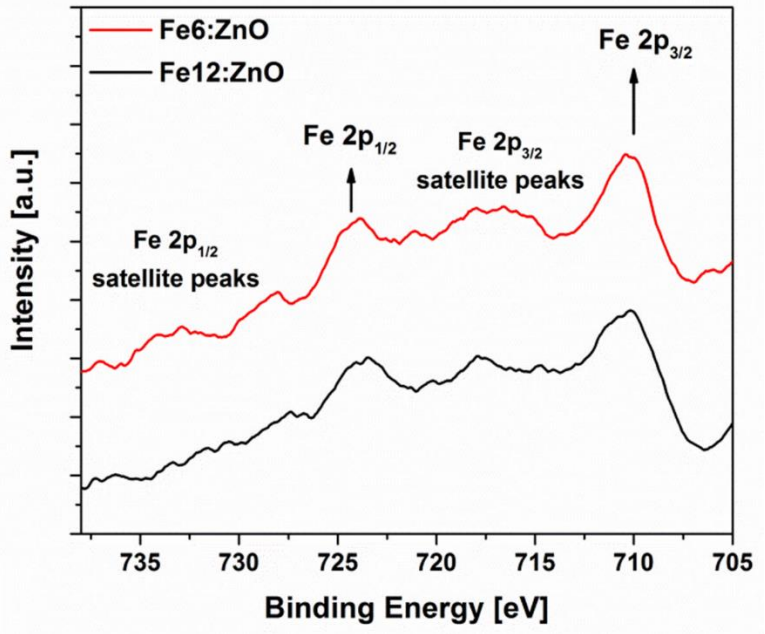


Figure 25: High-resolution XPS spectra of Fe2p for Fe:ZnO NPs doped at different Fe concentrations.

HR $Fe2p_{3/2}$ spectra deconvolution is shown in Figure 26. Each spectrum could be fitted with separate components associated to Fe-O bonds involved into FeO and

$Fe_2O_3$, respectively[304]. This aspect evidences the coexistence of $Fe^{3+}$ and $Fe^{2+}$ valence states for Fe dopant in both families of the doped samples. If the area % under each component is considered (Table 6), a preponderance of $Fe^{3+}$ ions relative to $Fe^{2+}$ can be highlighted for the sample Fe6:ZnO. On the contrary, $Fe^{2+}$ ions are predominant for sample Fe12:ZnO. By increasing the amount of Fe dopant, an increase of $Fe^{2+}$ fraction at the expense of $Fe^{3+}$ is then observed, similarly to what reported in other works[131,305,306].

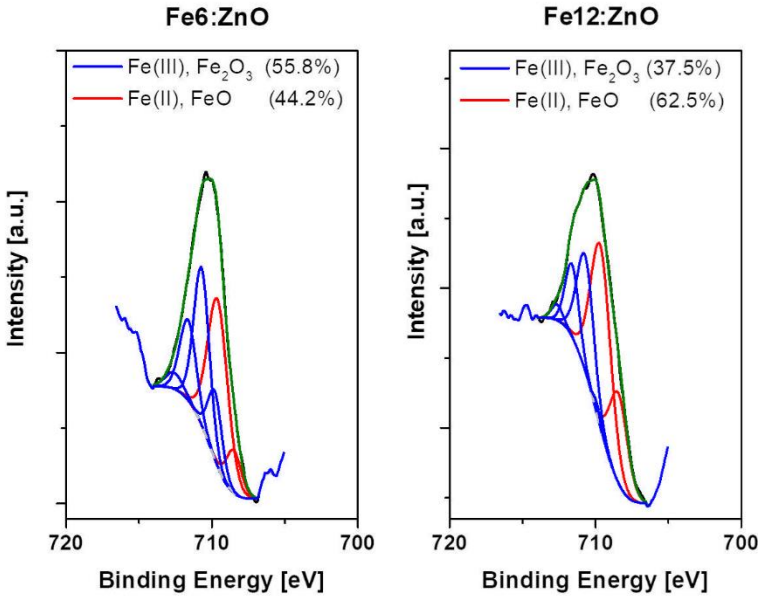


Figure 26: Curve fitted $Fe2p_{3/2}$ spectrum for Fe:ZnO nanoparticles.

**Table 6**: FeO and $Fe_2O_3$ peak components (binding energy and % area) obtained by deconvolution of HR $Fe2p_{3/2}$ XPS spectrum.

| Sample | Fe (II), FeO | | Fe (III), $Fe_2O_3$ | |
|---|---|---|---|---|
| | Binding Energy [eV] | Area [%] | Binding Energy, [eV] | Area [%] |
| Fe6:ZnO | 708.5 | 7.1 | 709.8 | 10.6 |
| | 709.6 | 37.1 | 710.7 | 27.4 |
| | | | 711.6 | 14.7 |

| | | | | |
|---|---|---|---|---|
| | | | 712.6 | 3.1 |
| | | **44.2** | | **55.8** |
| Fe12:ZnO | 708.4 | 19.2 | 709.9 | 0.9 |
| | 709.6 | 43.3 | 710.7 | 22.9 |
| | | | 711.6 | 11.6 |
| | | | 712.7 | 2.1 |
| | | **62.5** | | **37.5** |

The crystallinity of the ZnO and Fe:ZnO nanoparticles has been evaluated through X-ray diffraction. The resulting patterns are reported in Figure 27. Despite the broadening due to the small dimensions of the particles, the peaks belonging to the wurtzitic structure of ZnO can be identified in all the three cases according to JCPDS-ICDD (card n. 89-1397) and witness that all the prepared NPs are crystalline. In particular, the most intense ones can be assigned to (100), (002) and (101) ZnO crystallographic directions.

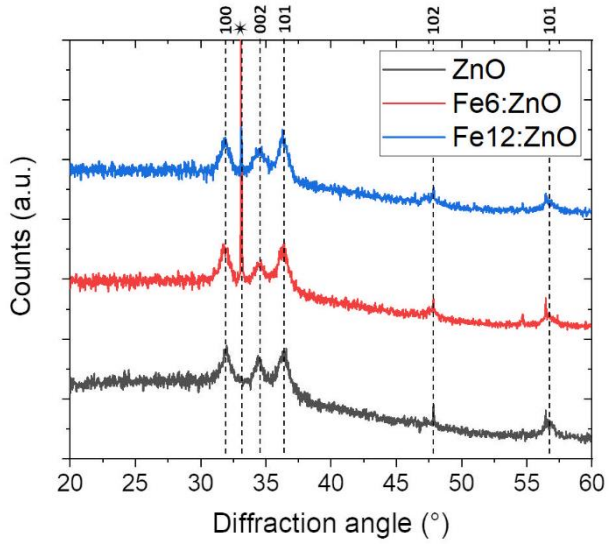


Figure 27: X-ray diffraction patterns of ZnO, Fe6:ZnO and Fe12:ZnO NPs. * refers to the silicon wafer used as substrate.

No additional diffraction peaks belonging to metallic Fe or Fe oxide phases are observed within the detection limit of XRD instrument, suggesting that additional Fe-related crystalline phases neither nucleate and grow during the synthesis, nor is detrimental for the crystalline wurtzitic structure of the nanoparticle.

As a further information about the level of crystallinity, the dimension of the crystallites forming the nanoparticles has been evaluated according to Debye-Scherrer formula. The results are summarized in Table 7 for the functionalized NPs. The crystallites dimension agrees with FESEM results, which showed that the particles dimension ranged between 4 and 10 nm. This allows to state that our nanoparticles are single ZnO nanocrystals as also demonstrated by TEM images, for both the undoped and doped case. Moreover, the crystallite dimension is even increased with doping, indicating that the introduction of Fe ions may induce a slight increase of crystalline structure of the nanoparticle.

**Table 7**: Crystallite dimension evaluated through the Debye Scherrer equation for the (100) plane for the ZnO and Fe:ZnO NPs.

| Sample | (100) |
|---|---|
| ZnO | 6.0 nm |
| Fe6:ZnO | 8.3 nm |
| Fe12:ZnO | 12 nm |

The introduction of doping atoms in the host ZnO crystal is indeed expected to induce a distortion in the lattice structure which can be also evaluated by considering the shift of the 2θ peak positions measured by the XRD pattern.

In Table 8, the shift measured by comparing the 2θ angles corresponding to the three main reflections of ZnO and Fe:ZnO NPs are reported. The main variations are along the (001) and the (002) planes and suggest a slight modification of the lattice parameters due to the difference in ionic radii between $Zn^{2+}$ (0.74 Å) and $Fe^{2+}/Fe^{3+}$ dopant (0.78/0.64 Å, respectively).

**Table 8**: Diffraction angle shifts on the peaks corresponding to the (100), (002) and (101) planes with respect to the ZnO NPs. $\Delta\theta = \theta Fe:ZnO - \theta ZnO$.

| Sample | ΔΘ (100) | ΔΘ (002) | ΔΘ (101) |
|---|---|---|---|
| Fe6:ZnO | -0.121° | +0.061° | +0.020° |
| Fe12:ZnO | -0.088° | +0.114° | -0.032° |

In conclusion, both XRD and XPS results state that Fe was successfully included in the host ZnO lattice structure. This aspect is of particular interest especially in view of the magnetic and electromechanical behavior of the doped NPs, which are discussed in the next sections.

The functionalized NPs were analyzed through dynamic light scattering (DLS) in two different solvents: ethanol and water.

Table 8 summarizes the results for the amino functionalized particles (whose graphs are reported in Figure 28). The polydispersity index (PDI) in both water and ethanol never exceeds the 0.160 value and confirms the narrow size distribution already highlighted with FESEM analysis. Therefore, it can be stated that the population of the considered NPs is substantially monodisperse[69].

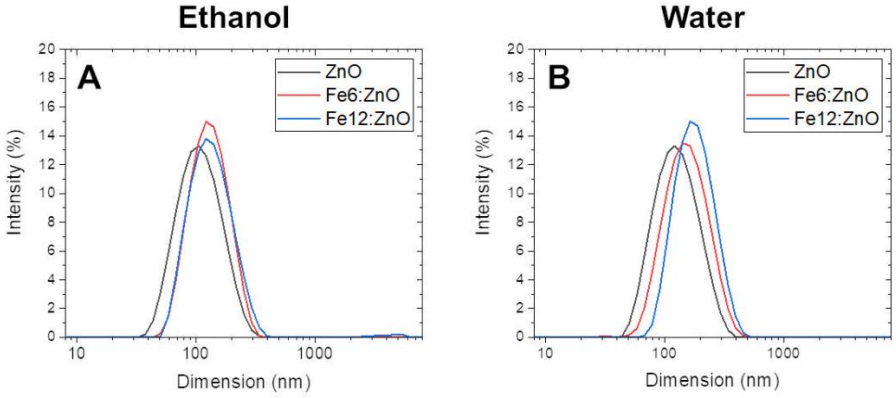


Figure 28: Size distribution from Dynamic light scattering obtained for the NPs. The graphs shows the intensity of the signal expressed in percentage of ZnO and Fe:ZnO NPs in ethanol (A) and water (B).

**Table 9**: Relative atomic concentration for ZnO and Fe:ZnO nanoparticles estimated from HR-XPS analysis. Dynamic light scattering results for Fe:ZnO NPs. The hydrodynamic diameter (DH) and the polydispersity index (PDI) are expressed as mean values ± standard deviation of three measurements.

| Sample | $D_H$ in ethanol | PDI in ethanol | $D_H$ in water | PDI in water |
|---|---|---|---|---|
| ZnO | 98.5± 0.2 nm | 0.154±0.019 | 116.2±0.4 nm | 0.148±0.011 |
| Fe6:ZnO | 120.4±0.2 nm | 0.133±0.010 | 139.0±1.8 nm | 0.138±0.025 |
| Fe12:ZnO | 124.4±0.4 nm | 0.144±0.021 | 167.6±1.7 nm | 0.121±0.003 |

It must be observed that the hydrodynamic diameter found from DLS measurements is well above the dimensions found with electron microscopy analysis. In fact, the smallest value is found for undoped ZnO is close to 100 nm (Table 8), thus 10 times higher than the NPs size estimated by electron microscopy (Figure 16). This phenomenon can be attributed both to the presence of chemical

groups on the particles surface which increase the hydrodynamic diameter of the particle as well as the adsorption of ions at the NP surface or even to the formation of NPs aggregates.

The hydrodynamic size of the nanoparticles is increased when the doping level is increased as well, suggesting a higher level of aggregation of doped nanoparticles.

However, the level of monodispersion is still high also in water, where the hydrodynamic diameter is the largest one. This is due also to the surface charge of the nanoparticles which is highly positive, well above +20 mV (Table 9) and in agreement with what found for ZnO NPs after amino functionalization because of the presence of the amino groups[75]. However, the overall result is to have highly positively-charged nanoparticles which repel each other assuring an optimal dispersion.

**Table 9**: Z-potential Fe:ZnO NPs with amino functionalization. The Z-potentials are expressed as mean values ± standard deviation of three measurements.

| Sample | Z-potential after functionalization |
|---|---|
| 0 at.% | 22.7±0.9 mV |
| 6 at.% | 26.4±0.4 mV |
| 12 at.% | 25.5±0.5 mV |

## 2.3.2 Optical, magnetic and piezoelectric characterization

The absorption spectra recorded for ZnO and Fe:ZnO NPs are shown in Figure 29A. From the optical standpoint, a strong absorption in the ultraviolet (UV) region is observed for all the three samples, as represented by the absorption peak at $\lambda$ = 348 nm. The UV absorption intensity is more pronounced for Fe:ZnO NPs and in particular for the mostly doped ones (Fe12:ZnO NPs). All these aspects make the prepared NPs good UV-absorber materials and promising candidates for a lot of applications in which a good UV absorption is required like photodynamic therapy[307,308] or antimicrobial purposes[309,310].

Moreover, it is worth mentioning that Fe:ZnO nanoparticles present a slight absorption in the visible region as well. This behavior is further intensified as the level of doping is increased. This aspect may play a significant role in biomedical applications, since extending the optical activation of the NPs, i.e. for example for

photodynamic therapies, can be beneficial when using lower-energy and thus safer light sources.

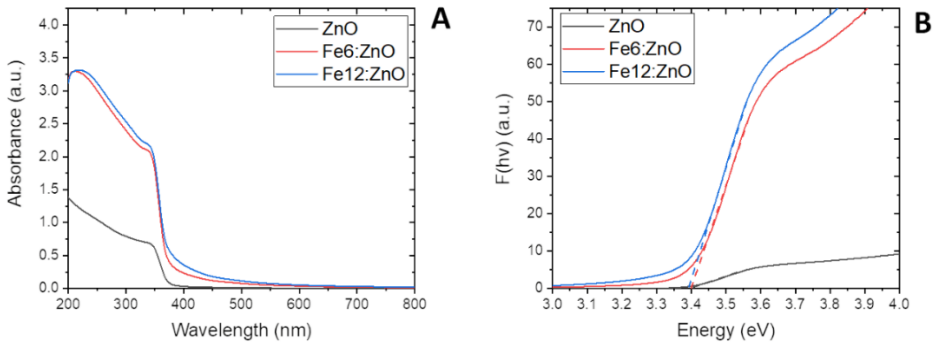


Figure 29: UV-visible spectra (A) and Tauc's plot (B) of ZnO and Fe:ZnO NPs.

From the UV-vis spectra, the optical band-gap of the NPs could be estimated according to Tauc's plot[311], as shown in Figure 29B. The calculated band gap value is around 3.39 eV for all the samples. This value is in agreement to what previously found from some of us on Gd- and Mn-doped ZnO NPs prepared with a similar synthetic technique, where very small band-gap variations among undoped and doped ZnO NPs were found[120].

Doping ZnO typically involves a modification of the electronic structure of the material by the generation of new electronic states. If these electronic states fall in the band gap region, new electronic transitions upon light excitation are allowed, resulting into fluorescence emission[312].

For this reason, the fluorescence spectra of the synthesized Fe:ZnO NPs have been acquired.

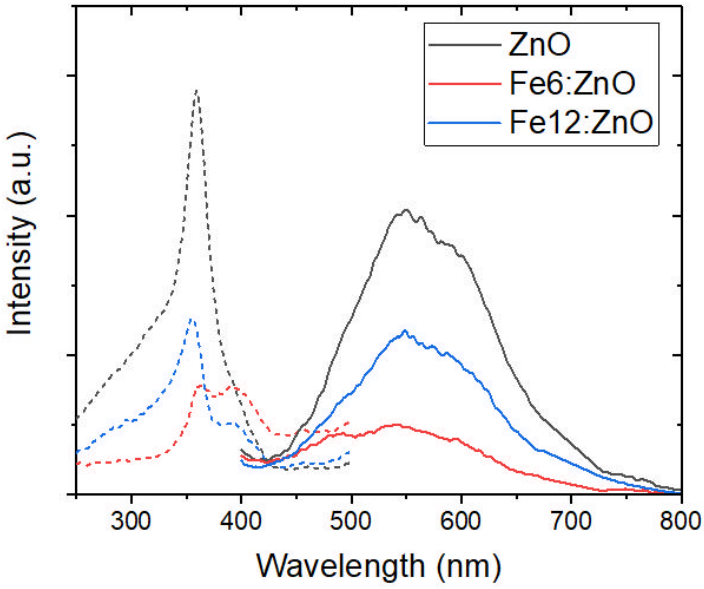


Figure 30: Fluorescence spectra of ZnO and Fe:ZnO NPs. Dashed lines represent the signal retrieved exciting the sample at wavelength below λ=500 nm and collecting the emission at λ=550 nm; solid lines refer to the emission retrieved by exciting the sample at λ=348 nm.

The results are reported in Figure 30 for all the three kinds of nanoparticles. When excited with a UV radiation (here in particular with λ = 348 nm), all the NPs show a broad green light emission (centered at λ=550 nm, see all the solid lines), in agreement to what found for other ZnO nanostructures[313,314]. However, this is typically attributed to oxygen vacancies and related effects rather than on doping[315], for which there is no rising of any additional peak. Moreover, the fluorescent emission of the doped nanoparticles is lower than for the undoped ones. However, when considering the excitation spectra (dotted lines in Figure 30) both iron-doped NPs present a secondary peak of excitation at 400 nm. The presence of this peak is in agreement to what found in the UV-vis spectra where a higher absorption was observed up to λ=400 nm. This feature confirms that the prepared iron-doped NPs are good UV-absorber materials, with a potential use for photodynamic therapy or antimicrobial applications, as highlight above.

Introducing magnetic ions inside a semiconductor may allow the formation of localized magnetic dipoles which can affect the electronic carriers' behavior[316]. This is the case of iron ions, which present an incomplete d electronic shell. When

included in the ZnO crystal structure, the rise of a ferromagnetic behavior is typically observed[132,180]. Moreover, the inclusion of iron ions can also induce the increase of the maximum magnetization that the particles can reach at room temperature under the application of a magnetic field. Figure 31 reports the measurements regarding the DC magnetization of ZnO and Fe:ZnO NPs. As it can be noticed, all the nanoparticles show a paramagnetic behavior, which is however modified in magnitude by increasing the Fe doping. Interestingly, a similar paramagnetic response is found also for the undoped ZnO nanoparticles, for which a diamagnetic behavior was expected. The reason of this behavior may lay in the presence of the oleic acid shielding, which could partially influence the surface electron behavior, changing the magnetic properties of the nanoparticle, as it happens in other ZnO-based systems with a different functionalization[317]. To this purpose, this paramagnetic response for undoped nanoparticles has been found by some of our groups[120] as well, with almost identical magnetization magnitude.

As already mentioned, increasing the amount of doping inside the crystal enhances the maximum magnetization measured applying a magnetic field of 800 kA/m on the sample. In fact, for the Fe12:ZnO NPs a magnetization of 16.7 $Am^2/kg$ is found, against the 9.1 $Am^2/kg$ retrieved in the case of Fe6:ZnO NPs. These values are almost one order of magnitude higher with respect to the maximum magnetization obtained for the undoped nanoparticles (1.5 $Am^2/kg$).

The origin of magnetic properties in Fe-doped ZnO materials is still under debate. Several studies pointed out that it may originate from the formation/precipitation of secondary magnetic phases within the material[318]. Instead, other works showed that the magnetic behavior of Fe:ZnO NPs is due to the existence of mixed Fe valence states allowing the exchange interaction between conductive electrons and local spin polarized electrons[176,319–321].

The noticeable enhancement in the maximum magnetization observed for our Fe:ZnO NPs has to be attributed to the effective incorporation of Fe magnetic atoms in the ZnO crystal structure. XPS and XRD results allow to exclude the formation/precipitation of secondary magnetic phases and point out the co-existence of both $Fe^{2+}$ and $Fe^{3+}$ ions substituting at $Zn^{2+}$ sites. It is also noticed that the dominant Fe valence state ($Fe^{2+}$ or $Fe^{3+}$) changes according to the overall dopant amount. Therefore, the magnetic behavior observed in our Fe:ZnO NPs is more likely due to electron double-exchange mechanism[279,321,322] while the different magnetic behavior among the Fe-doped NPs can be due to the difference in the amount of incorporated Fe dopant, and to the change of the dominant Fe valence state[176,319–321]. This strong paramagnetic behavior of the nanoparticles can be then

successfully exploited for biomedical imaging applications, like magnetic resonance imaging.

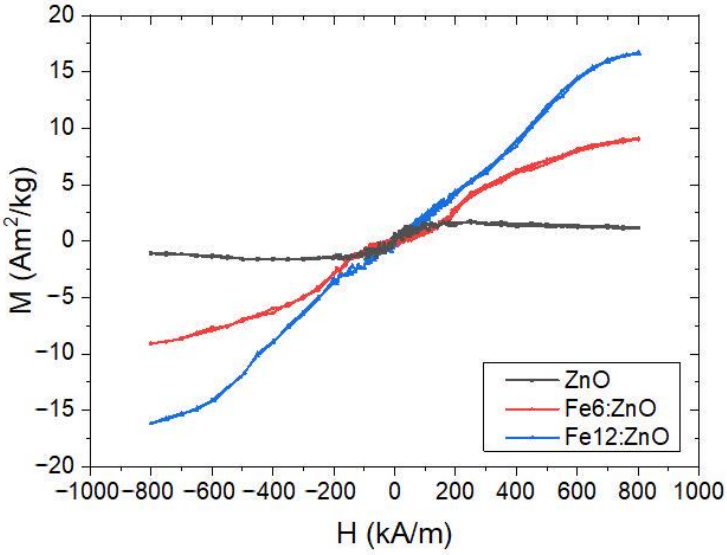


Figure 31: Magnetization-saturation (M-H) curves measured at room temperature of ZnO and Fe:ZnO NPs with different doping levels.

The electromechanical behavior of Fe:ZnO NPs was qualitatively investigated by considering the mechanical displacement experienced by Fe:ZnO NPs nanoparticles films under the application of an external bias voltage (Figure 32). It is found that Fe doping influences the electromechanical response, with Fe:ZnO NPs showing closed-loop curves resembling those reported in the literature for common piezoelectric ceramics (PZT, barium titanate)[323,324] and other doped ZnO materials[99,111]. In particular, Fe6:ZnO NPs show a better electromechanical response than Fe12:ZnO, with an improved peak-to-peak mechanical displacement that changes from around 1 nm for sample Fe12:ZnO to around 3 nm for Fe6:ZnO NPs. Despite showing an electromechanical displacement comparable to Fe6:ZnO NPs, the behavior of undoped ZnO NPs is slightly different; the D-V curve shows a negligible hysteretic behavior, suggesting the absence of a ferroelectric domains structure, in accordance with the literature[61]. It is worth mentioning that the remarkable mechanical displacements measured in this work could be biased also by the bending of the substrate, which cannot be neglected with the used measurement apparatus[325]. Therefore, a quantitative estimation of the piezoelectric

constant for the tested NPs cannot be obtained, as it would be overestimated due to the above-mentioned effect superimposed to the piezoelectric one.

The improved electromechanical response due to Fe doping can be related to the different valence states of the Fe ions incorporated in the ZnO crystal. Both XPS and XRD analyses pointed out that Fe dopant was correctly incorporated in the host ZnO crystal structure, with $Fe^{3+}/Fe^{2+}$ ions substituting at $Zn^{2+}$ sites. The fraction of $Fe^{3+}/Fe^{2+}$ ions is changed according to the dopant amount. In particular, the smallest $Fe^{3+}$ is the dominant valence in sample Fe6:ZnO. By increasing the nominal doping level up to 12 at.%, the biggest $Fe^{2+}$ ions become the predominant ones. Among others, the electromechanical response of wurtzitic ZnO is governed by the ease rotation/bending of bonds in the crystal-line cell. The substitution of $Zn^{2+}$ sites with smaller $Fe^{3+}$ having also a higher positive charge promotes an easy bending/rotation of bonds under the application of an external electric field, making easier the alignment of electric dipoles along the c-axis direction, i.e. the polarization direction of ZnO, and finally improving the overall piezoelectric mechanical displacement of the material[131] [43]. On the other hand, the substitution of $Zn^{2+}$ with bigger $Fe^{2+}$ ions makes this rotation/bending more difficult. $Fe^{2+}$ is the predominant valence for Fe doping in the sample Fe12:ZnO. Therefore, in this case it is found that Fe doping could somehow limit the electromechanical response. Finally, it can be also concluded that a proper modulation of chemical state for Fe dopant must be foreseen if the enhancement in the electromechanical response of Fe:ZnO NPs wants to be pursued. Furthermore, the enhanced electromechanical response provided by iron doping could represent an interesting tool for therapeutic purposes, because the possibility to induce a tunable electric potential on the treated cells may also disrupt cell ions homeostasis and induce anti-cancer drug sensitization[300].

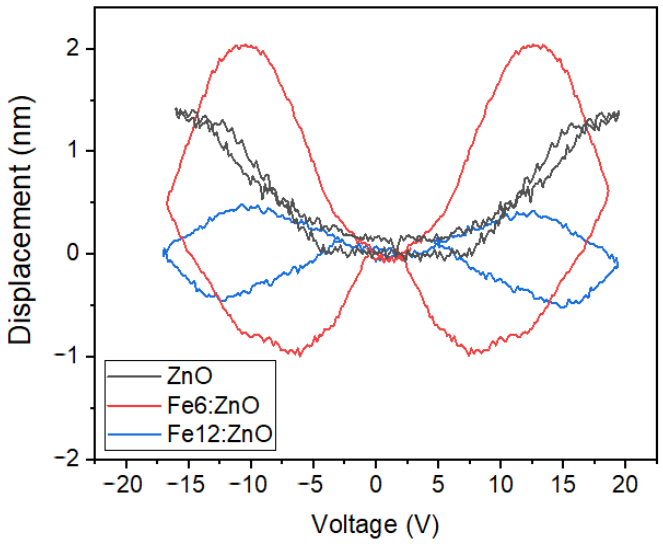


Figure 32: Electromechanical displacement vs. applied bias voltage, measured for ZnO and Fe:ZnO NPs with different doping levels

### 2.3.3 Conclusions

In this work, iron-doped ZnO NPs were developed to obtain a versatile theranostic material to be used in cancer therapies.

NPs with a diameter between 4 and 10 nm were synthesized with different level of iron doping, and pure ZnO nanoparticles were used as control. The spherical morphology of the nanoparticles was not affected by doping. EDS and XPS analyses revealed that iron doping incorporation within the NPs was consistent with the synthesis protocol. XRD, TEM and XPS analyses showed that NPs were single-phase wurtzitic crystals and confirmed the correct inclusion of iron ions in the host ZnO crystal lattice. With the increase of doping, $Fe^{2+}$ was found the predominant oxidation state, despite both $Fe^{2+}$ and $Fe^{3+}$ ones being present in all the doped particles.

The optical behavior of the NPs changed with doping. Indeed, despite all the ZnO NPs still being strong UV absorbers, the inclusion of iron in the NPs enlarged the light absorption spectral range of the system toward visible light, paving the way to biomedical applications, i.e. therapeutic activation by light as in photodynamic therapy.

Both ZnO and Fe:ZnO NPs showed a paramagnetic behavior. However, the inclusion of iron magnetic moments inside the crystal elicits a noticeable enhancement of the maximum magnetization, with consequent potential uses of Fe:ZnO NPs as contrast agent in magnetic resonance imaging.

An increased electromechanical response was found for the doped NPs. The rising of a hysteresis in the corresponding D-V curve is attributed to the distortion that the iron ions may induce in the ZnO crystal, while the difference in the electromechanical response between doped NPs is attributed to the different ratio of $Fe^{2+}$ and $Fe^{3+}$ species, which may lead to a different distortion of the lattice because of ions radii. The enhanced electromechanical response suggests the use of the iron doped nanoparticles also as therapeutic agent, where the electric potential generated remotely by an external mechanical stimulation may alter specific cell behaviors to the point of promoting healthy cells proliferation or even inducing tumoral cells death.

As a conclusion, Fe:ZnO NPs showed very promising optical, magnetic and electro-mechanical properties that could be effectively used in nanomedicine. In particular, Fe6:ZnO NPs showed to have the best trade-off between enhanced magnetic and electromechanical functionalities, suggesting their use as a powerful theranostic agent for cancer treatment.

# Chapter 3

# Fe:ZnO NPs as a nanodevice against pancreatic cancer cells

Part of this chapter has been taken from the publication from "Carofiglio M., Conte M., Racca L., Cauda V. *Synergistic Phenomena between Iron-Doped ZnO Nanoparticles and Shock Waves Exploited against Pancreatic Cancer Cells*. ACS Applied Nanomaterials"[326].

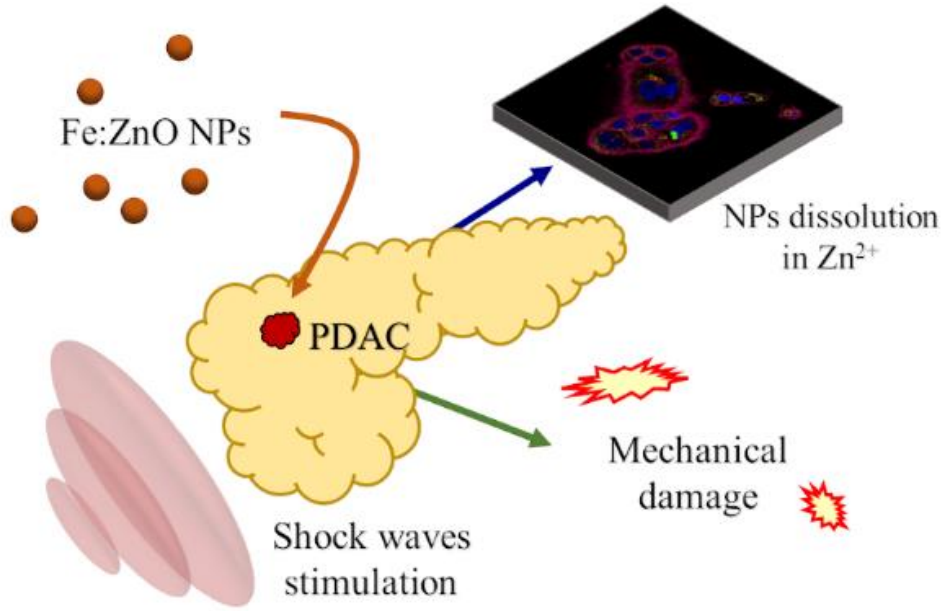


Figure 33: Graphical summary of the chapter. Fe:ZnO NPs were tested on an adenocarcinoma pancreatic cancer cell line to assess the therapeutic efficacy of the developed nanoparticle when coupled to an external mechanical stimulation.

## 3.1 Introduction on pancreatic cancer

Theranostic nanosystems are acquiring more and more relevance in nanomedicine[327]. The potential advantages offered by the administration of a site-specific therapy while constantly monitoring the patient conditions are actually enormous in the context of cancer, as for all other diseases which are very difficult to treat[289,328]. Several prototypes of smart nano-sized devices able to perform both these tasks can be found in the literature[329–331]. One of the major trends includes the use of nanosystems incorporating imaging moieties and carrying antitumoral drugs[25], such as polymeric nanoparticles (NPs) [332–335], liposomes[336–338] or mesoporous silica NPs[339,340]. However, a main drawback of these devices is the inability to precisely control their release location, or to remotely activate them, leading to an unwanted leakage of their cargo before reaching the tumor environment.

New approaches feature NPs which can be activated to perform the therapy only once they have reached the site of interest. Recent advancements are going toward smart nanomaterials able to react to different physical and chemical stimulations. Examples includes pH-sensitive materials capable of releasing anti-tumoral drugs only in the acidic tumor environment[341,342] or magnetic nanoparticles, like iron oxide nanoparticles[343,344], which can be remotely directed and excited to induce hyperthermia once inside the cancer tissues[292,345,346]. Other classes of stimuli-responsive nanomaterials are NPs aimed at photothermal[347–349] (PTT) and photodynamic[350] (PDT) therapies. The underlying concept is to excite such nanoparticles with a light source, in order to induce toxic phenomena in nearby tissues. PTT consists in the excitation of optically responsive materials, i.e. metal nanoparticles, with an electromagnetic radiation, typically in the infrared region of the light spectrum. Once the light is absorbed, the excited material converts this energy into heat, which can ablate the tumor tissue and eventually cause cell death. Due to the electronic quantum confinement given by the nano-scale, gold nanoparticles result extremely suitable for this purpose, as widely demonstrated by the large amount of related works in the literature[351–354]. On the other hand, most of PDT approaches rely on the generation of reactive oxygen species (ROS) upon light irradiation. ROS production is expected to induce toxicity on the diseased cells[355]. Thus, whatever the energy sources used or the mechanism involved, the advantage of these remotely-controlled NPs is their ability to activate the toxic phenomenon, provoking cell death exclusively on cancer cells, only once the therapeutic moiety has effectively reached its target[356].

The use of remotely-controlled NP approaches can face some drawbacks too. Indeed, the visible light possesses a quite low tissue penetration, while UV radiations may damage healthy tissues with side effects potentially overwhelming the benefits of the therapy[357]. Alternate magnetic field, if too much intense, can provoke damages to normal tissues and create undesired eddy currents[358].

Tissue penetration becomes a very important parameter to consider when treating deep-seated tumors, like pancreas. Pancreatic cancer and in particular the most common form of this disease, namely pancreatic ductal adenocarcinoma (PDAC) [359], is very difficult to treat due to the characteristics of its development, which provide it with resistance toward standard cancer treatments[360,361]. Therapeutic approaches like PDT could successfully address the difficult task of reducing tumor growth. However, the location of the pancreas inside the human body does not allow an effective stimulation with light. Different remote stimulations have been proposed as possible alternatives. An example is represented by the stimulation with periodic pressure waves, like ultrasounds (US) or shock waves, these last being sharp discontinuities, i.e. compressive and tensile waves, involving a sudden and strong change in pressure and density in a medium[293,362]. Indeed, US represents a valuable alternative to light because pressure waves can penetrate deeper in the organic tissues interposed between the stimulation source and the target, while preserving a good level of safety on normal tissues when low irradiation powers are employed. Several molecules have been proposed as enhancers of this phenomenon, and are referred to as sonosensitizers, i.e. systems able to induce hyperthermia or ROS generation only upon US stimulation so as to localize the therapy performed on the system[363]. In this perspective, nanoparticles such as gold[364,365], titanium oxide[366,367] and zinc oxide[90,94,368] have been suggested as sonosensitizing agents and have shown a great potential in this field. The superiority of NPs with respect to organic sonosensitizer molecules appears clear and is currently extensively debated in literature[369]. NPs are able to better disperse in biological water-based media than organic molecules, can be biocompatible, and can accumulate in the tumor mass thanks to the enhanced permeation and retention (EPR) effect or, even better, exploiting functional biomolecules at their surface for active targeting[370]. Furthermore, NPs can be designed to act both as theranostic tools and to be fully biodegradable at the end of their mission in the biological environment.

In this chapter we propose the use of the Fe6:ZnO NPs, as also shown in the previous chapter (henceforth Fe:ZnO) , and we take advantages of their imaging and therapeutic potentialities. We prove their effectiveness as sonosensitizing

agent, by reducing pancreatic cancer viability in vitro when coupled with a remote mechanical stimulation, i.e. shock waves.

The target of this first proof-of-concept test is a PDAC cell line (BxPC-3). Actually, PDAC can only be reached with a deep stimulation and displays innate and acquired drug resistance. It therefore urgently requires more effective therapeutic approaches, as the one here proposed. Fe:ZnO NPs are thus tested first in terms of their cytocompatibility, cellular uptake and NPs dissolution in cell culture media in comparison to undoped ZnO NPs. The obtained results aim to increase the understanding of the Fe:ZnO NPs fate inside the cell, when their administration is not coupled with a remote physical stimulation, and to evaluate the final and safe biodegradation. The coupling of the NPs with a mechanical stimulation, i.e. pressure shock waves, is exploited to induce cell death only on demand, to achieve a remotely-controlled and safe therapy. Therefore, BxPC-3 viability is assessed with the coupled treatment and then the cell fate is observed to determine the cell death mechanism and other possible aspects that could be improved in view of a future clinical translation.

## 3.2 Materials and methods

The synthesis and functionalization of Fe:ZnO NPs follows the same procedure described for ZnO and Fe6:ZnO in Chapter 2.

### 3.2.1 Cell culture, viability, and internalization assays

Fe:ZnO and ZnO NPs were tested on a PDAC cell line, i.e. BxPC-3 (ATCC CRL-1687). For daily cell culture, cells were cultured at 37 °C and 5% of $CO_2$ in RPMI 1640 medium (ATCC) supplemented with 10%v of previously heat-inactivated fetal bovine serum (FBS, ATCC), 100 µg/mL of streptomycin and 100 units/mL of penicillin (Sigma-Aldrich).

Cytotoxicity tests were performed in 96-well plates (TC-treated, Corning) with the WST-1 proliferation assay (Roche). More in detail, 2500 cells dispersed in 100 µL of cell culture medium were seeded in each well and let adhere on the bottom of the well. After 24 h of incubation, Fe:ZnO and ZnO NPs directly taken from the ethanolic stock solution (2 mg/mL and 1 mg/mL for Fe:ZnO and ZnO NPs respectively) were dispersed at different concentrations in fresh culture medium (10, 15, 20 and 25 µg/mL of NPs). The NPs dispersions were then administered to cells by simple cell culture medium substitution.

The cytotoxicity was evaluated at different times of incubation (24, 48 and 72 h). In particular, 10 µL of WST-1 reagent were added to each well 2 hours before the expiration of the incubation time step in question. A plate reader (Multiskan GO microplate spectrophotometer, Thermo-Fisher Scientific) was exploited for the measurements. More in detail, the absorbance of the samples was evaluated at 450 nm ($A_{450}$), while the one at 620 nm ($A_{620}$) was used as reference. For all the samples, the absorbance value obtained by the cell culture medium with no cultured cells ($BK_{450}$-$BK_{620}$) was subtracted from the actual measure; the resulting value was then divided by the absorbance of the control cells ($CT_{450}$-$CT_{620}$), in order to obtain a percentage value as reported in other works[94,366]. More explicitly, the formula leading to cell viability percentage evaluation ($C_{\%}$) is:

$$C_{\%} = 100 \cdot \frac{(A_{450} - A_{620}) - (BK_{450} - BK_{620})}{(CT_{450} - CT_{620}) - (BK_{450} - BK_{620})}$$

The tests were repeated on a non-cancerous cell line (i.e. HPDE-H6c7, human pancreatic duct epithelial cells, Kerafast, Inc., Boston, MA) in order to assess the safety of the fabricated particles on healthy cells. The procedure followed for the tests was exactly the same as the one used for the BxPC-3 cell line.

The internalization of Fe:ZnO and ZnO NPs in BxPC-3 cells was evaluated through flow cytofluorimetry. To do so, $3\times10^5$ cells were seeded in a 24-well plate (TC treated, Thermo Fisher) with 500 µL of cell culture medium. After 24 h from cell plating, the medium was replaced with cell culture medium containing NPs (10 µg/mL for pure ZnO NPs, 10 and 15 µg/mL for Fe:ZnO NPs). The NPs had been previously labelled with ATTO647-NHS ester, as described in a previous work[91], and their uptake by BxPC-3 cell line was evaluated after 5 and 24 h. The aim was to determine the timing at which the majority of BxPC-3 was able to internalize the administered NPs, so as to maximize the effects of further treatments. At the end of the incubation time, the cells were washed twice with PBS to remove non-internalized NPs and then detached through trypsinization. Once collected, cells were centrifuged (130 g for 5 minutes) and resuspended in 300 µL of PBS. The cell suspension was analyzed through a Guava Easycyte 6-2L flow cytometer (Merk Millipore), following the same procedure already described elsewhere[94]. The analysis of the results was performed with Incyte Software (Merk Millipore).

All biological tests were performed at least in triplicates and ANOVA tests were performed with the software Origin (OriginLab).

The internalization of Fe:ZnO NPs inside BxPC-3 cells was also analyzed through spinning-disk confocal fluorescence microscopy (Ti2 Nikon equipped with Crest Large FOV laser and 60x PlanAPO objective, NA = 1.40) to locate the position of the NPs inside the cell. To do so, $1\times10^4$ cells were seeded into 8-well chamber slides (Nunc Lab-Tek II CC2 Chamber Slide System, Thermo Fisher Scientific) with 250 µL of complete cell culture medium. ATTO647-NHS labelled Fe:ZnO NPs were then administered to cells (15 µg/mL) 24 h from seeding. 24 h later, cells were fixed by replacing cell culture medium with 150 µL of Image-IT fixative solution (Thermo Fisher). After 10 minutes at room temperature, cells were washed twice with phosphate-buffered saline (PBS) solution and their membranes were stained by incubating them with 250 µL of PBS containing Wheat Germ Agglutinin conjugated with an Alexa Fluor 488 dye (WGA-488, Thermo Fisher) at a concentration of 2.5 µg/mL for 10 minutes in normal cell culture conditions. After this time, cells were washed twice with PBS and then Hoechst (Thermo Fisher) at a concentration of 0.3 µg/mL in PBS was administered to cells for nuclei staining. After 5 minutes at 37°C, cells were washed twice with PBS and Live Cell Imaging (LCI, Molecular Probes) solution was finally added. The samples were immediately analyzed following staining.

### 3.2.2 Shock wave treatment

The behavior of BxPC-3 cells subjected to mechanical stimulation coupled with the administration of a safe dose of Fe:ZnO NPs was analyzed. Cells were seeded in a 96-well plate adopting the same procedure previously described, following a specific plate layout designed in order to avoid cross-mechanical stimulation, i.e. leaving at least one well without cells between two nearby samples.

Cells were treated with the highest safe dose of Fe:ZnO NPs (15 µg/mL) and, after 24 h from NPs administration, they were mechanically stimulated with the $PW^2$ shock waves generator. The same power conditions and stimulation times exploited during ROS generation analysis were here employed (0.04 $mJ/mm^2$, 500 shots, 4 shots/s). In particular, three main stimulation typologies were set. In the first one, cells were only treated with the shock waves, without any NPs administration, to assess the toxicity of the SW treatment itself. The second typology consisted in the stimulation of cells that were first treated with Fe:ZnO NPs and then deprived of non-internalized NPs by means of a double washing with PBS and its replacement with freshly prepared cell culture medium just before the

SW treatment (Fe:ZnO Int). Finally, the third typology considered the stimulation of cells that were treated with Fe:ZnO and mechanically stimulated after 24 h from the NPs administration without any washing steps (Fe:ZnO Int+Ext). This last sample aimed at the exploitation of both intracellular and extracellular NPs for cells killing.

BxPC-3 cell viability was assessed with the WST-1 assay 24 h after the mechanical stimulation and compared to that of untreated cells, set as 100 % of viability.

### 3.2.3 Mechanisms of cell death

Fe:ZnO NPs were investigated in terms of reactive oxygen species (ROS) generation under remote mechanical stimulation using Electron Paramagnetic Resonance (EPR) spectroscopy coupled with the spin-trapping technique. More in detail, 1.5 μg of Fe:ZnO NPs were withdrawn from the ethanolic stock solution and dispersed in 90 μL of water. The dispersion was placed in a 96-well plate for cell culture (TC-Treated, Corning). Then 10 μL of a water solution of a spin trap (5,5-dimethyl-L-pyrroline-N-Oxide, DMPO, Sigma-Aldrich) at a concentration of 100 mM was added to the solution. The final concentration of Fe:ZnO NPs was 15 μg/mL while the DMPO final concentration for each sample was 10 mM. The Fe:ZnO NPs containing well was stimulated from the bottom with a high-energy focalized shock wave (SW) device $PW^2$ (R. Wolf, ELvation Medical) at an energy flux density of 0.04 $mJ/mm^2$ (12.5 MPa as maximum pressure peak) and a number of shots equal to 500 with a frequency of 4 shots/s. The well and the transducer were acoustically coupled with a gel (Stosswellen Gel, ELvation Medical GmbH). After the stimulation, a small volume of the NPs dispersion was withdrawn by means of a quartz capillary and analyzed with an EMXNano X-Band spectrometer (Bruker, center field 3426 G, 10 scans, 60 s sweep time). The spectra were processed with Bruker Xenon software (Bruker).

Dissolution of Fe:ZnO NPs into zinc cations in cell culture medium at 37 °C was also evaluated. Fe:ZnO NPs at a concentration of 1 mg/mL were dispersed in cell culture medium. Then, 70 μL of this dispersion was placed in the cap of a 1.5 mL centrifuge tube, opportunely separated by a dialysis membrane (SnakeSkin dialysis Tubing 3.5K MWCO, 16 mm dry I.D. by Thermofisher Scientific) from the rest of the tube to avoid NPs leakages. Then, 630 μL of cell culture medium was added in the tube, in contact with the NPs solution through the dialysis membrane so as to bring the NPs concentration in the overall solution to 100 μg/mL and to

allow only ions exchange. The tube was placed upside down in an orbital shaker at 37 °C for different incubation time steps (up to 72 h). At the end of each incubation time, the solution contained in the main tube (i.e. without NPs) was withdrawn and stored at 4 °C up to further analysis. The amount of zinc atoms (derived from dissolved zinc cations) was evaluated through Graphite Furnace Atomic Absorption Spectroscopy (GF-AAS) following EPA method 289.1.

An evaluation of the free zinc dissolved intracellularly after NPs internalization and in absence of any mechanical treatment was initially performed. Cells were plated in chamber slides, treated with Fe:ZnO NPs and fixed (see details above). The intracellular free zinc was labelled through FluoZin-3 AM (Thermo Fisher) probe: cells were washed twice with PBS and a 1 μM solution of FluoZin-3 AM fluorescent dye in PBS was administered. After 30 minutes of incubation at 37 °C, the excess of dye was removed by two washing steps with PBS. Then, cells lysosomes were labelled by substituting the PBS with a 1 μM dye solution (LysoTracker Red DND-99, Thermo Fisher) in PBS and incubating the cells for 30 minutes at room temperature. After two further washing steps, cell membranes and cell nuclei were stained with WGA-647 (Thermo Fisher) and Hoechst, following the same procedure reported above, and images were collected with the spinning disk confocal microscope. All the images were taken keeping exposure times and laser powers constant among the different samples. They were then post-processed in the same way, to allow a direct comparison between the samples in terms of free zinc intensity fluorescence too.

To unravel the mechanism of cell death under SW stimulation, cells were plated in clear 96-well plates following the same protocol exploited for cytotoxicity assays. Cells were then treated with Fe:ZnO NPs and shock waves. Free zinc was labelled again with FluoZin3-AM, while the cell membrane integrity was assessed with Propidium Iodine (PI, ThermoFisher) using 100 μL of 1 μM of PI solution in cell culture medium for 5 minutes at 37 °C. Then, cells were washed three times with PBS. The PBS was finally substituted with Live Cell Imaging solution and cells were imaged with a wide-field inverted fluorescence microscope (Eclipse TiE from Nikon) equipped with 40× objective (NA = 0.60).

The kinetics of both cell necrosis and apoptosis was evaluated through the RealTime-Glo Annexin V Apoptosis and Necrosis Assay (Promega) coupled with the microplate reader Glomax (Promega). More in detail, BxPC-3 cells were plated in a black 96-well plate with clear bottom (Corning) and treated with the same protocol exploited for SW treatments in the previous tests. Just before the SW treatment, 100 μL of the 2x Detection Reagent freshly prepared in RPMI 1640

according to the manufacturer indications were added to all the samples. A first measurement was performed before SW treatments. Then, the measurements were repeated immediately after the SW treatment and after 30 minutes, 1 h, 2 h, 4 h, 6 h and 24 h from the treatment.

Both the fluorescence and the luminescence signals retrieved from the measurements were analyzed, as recommended by the manufacturer. In particular, the obtained data were processed as fold induction of the signal obtained from the cells without any NPs and those subject to SW treatment, according to the formula: SampleSignal/ControlSignal.

## 3.3 Results and discussions

### 3.2.1 Cytotoxicity of pure and iron-doped ZnO NPs

Amine functionalized Fe:ZnO and ZnO NPs were administered to BxPC-3 cells in order to assess their cytotoxicity and to understand which dose can be exploited for further treatments with acoustic stimulation. As a general trend, both NPs types show a dose-dependent cytotoxicity which does not vary sensibly depending on the incubation time, as shown in Figure 34. In particular, the undoped ZnO NPs are safe up to 10 μg/mL for all the considered incubation times. In contrast, the toxicity is abruptly increased already at 15 μg/mL, with cell viability close to 20 % compared to the control samples. Moreover, a slight viability increase in time can be observed, with values always below 40 %.

A similar trend is observed for Fe:ZnO NPs, however, the highest safe dose is extended up to 15 μg/mL. The dose-dependent toxicity of ZnO is already well known in the related literature[91,285,371] and has been mainly attributed to two mechanisms: ZnO dissolution into $Zn^{2+}$ ions, able to disrupt the cell homeostasis leading to cell death, and the oxidative stress generated by the nanoparticles due to ROS production. Iron doping has been demonstrated to reduce the dissolution of ZnO nanoparticles providing them with a higher stability in aqueous media[130,207]. This translates into a higher safety of the nanoparticles, which has also been evidenced in this work when Fe:ZnO NPs are compared to their undoped counterparts. A lower toxicity also opens the possibility of administering higher doses of NPs, that are therefore more likely to induce toxic phenomena under external stimulation (i.e., shock waves).

In this particular case the highest safe dose, defined as the amount of NPs that can be administered without significantly damaging cells prior external stimulation,

is increased by 50 % thanks to the iron doping (i.e., from 10 µg/mL to 15 µg/mL). Furthermore, the iron-doped ZnO NPs show magnetic properties, not present in the undoped counterpart, as reported in previous works[176,180,320]. This is also true for the herein analyzed Fe:ZnO NPs, whose maximum magnetization is higher than the one measured for pure ZnO NPs (Figure 31). Such magnetic property is exploitable to employ them as contrast agents under MRI, yet leading to an intrinsically theranostic nanoparticle. For all these reasons, only iron-doped nanoparticles will be investigated henceforth when the mechanical stimulation is considered.

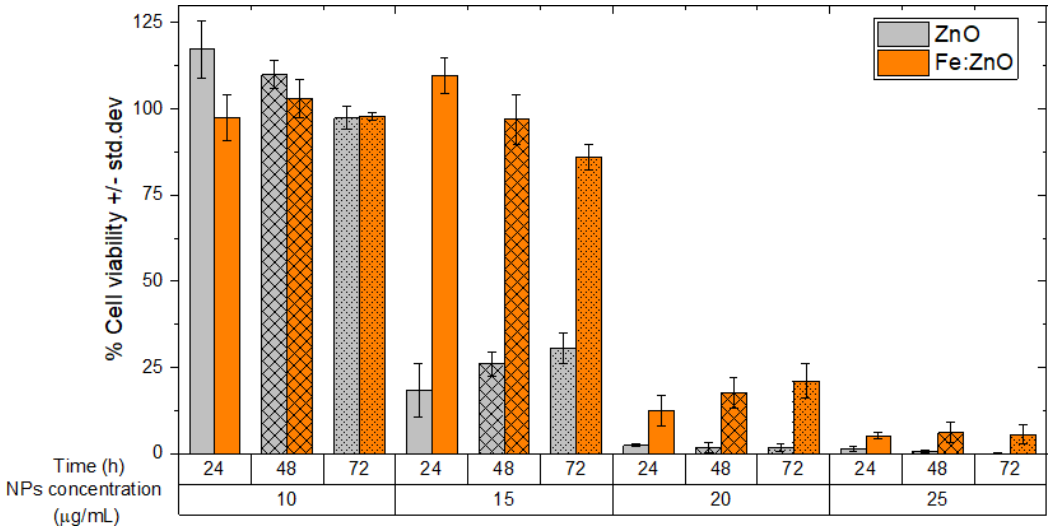


Figure 34: ZnO and Fe:ZnO NPs cytotoxicity on BxPC-3 cells at different incubation times from NPs administration, calculated from the results of the WST-1 assay. The value reported by the bars represents the mean ± std.dev percentage of n ≥ 3 measurements with respect to control cells.

Despite a proper targeting mechanism should be implemented on the highly customizable surface of the NPs in the present study, cytotoxicity tests on non-cancerous cells demonstrated an intrinsic selectivity of the NPs toward cancer cell killing. Figure 35 reports the results of the cytotoxicity experiments held on normal cells (HPDE). As it is clearly visible, with respect to what was found for cancerous cells, a higher dose of both ZnO and Fe:ZnO NPs can be administered to normal cells without affecting normal cell viability. Moreover, Fe:ZnO NPs are confirmed to be less toxic than ZnO NPs for normal cells too, further justifying their use during future treatments.

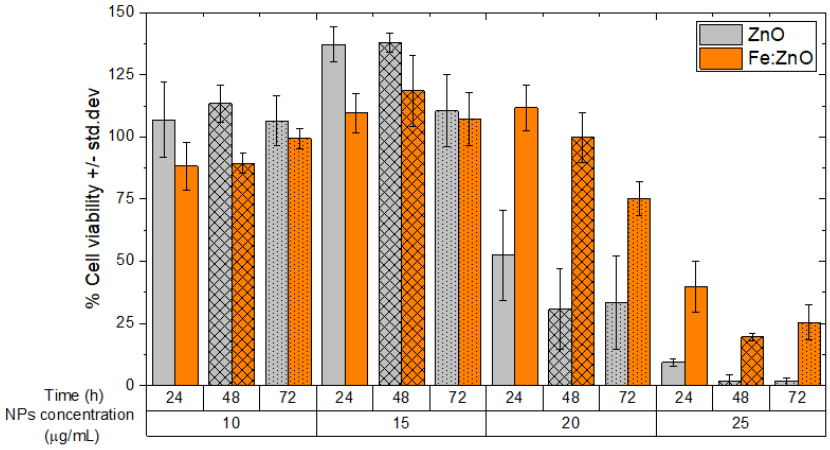


Figure 35: ZnO and Fe:ZnO NPs cytotoxicity on HPDE cells at different incubation times from NPs administration, calculated from the results of the WST-1 assay. The value reported by the bars represents the mean ± std.dev percentage of n ≥ 3 measurements with respect to control cells.

### 3.2.2 Fe:ZnO NPs internalization

ZnO and Fe:ZnO NPs were also investigated from the internalization standpoint. The ability of the BxPC-3 cell line to internalize the administered NPs was analyzed with cytofluorimetry and fluorescence microscopy.

In particular, cytofluorimetric assays (Figure 36) indicate that a higher percentage of cells (positive events) is able to internalize (or adsorb at their surface) the Fe:ZnO NPs when compared to pure ZnO NPs. This behavior was already reported in similar conditions by our group[101]. It has been also reported in the literature that a high positive Z-potential can favor NPs internalization into cells, which typically possess a negatively charged cell membrane[372–374]. Here, the higher Z-potential of iron-doped nanoparticles, together with the larger exploitable dose due to their increased safety, may explain the superior internalization in cells with respect to the undoped ZnO.

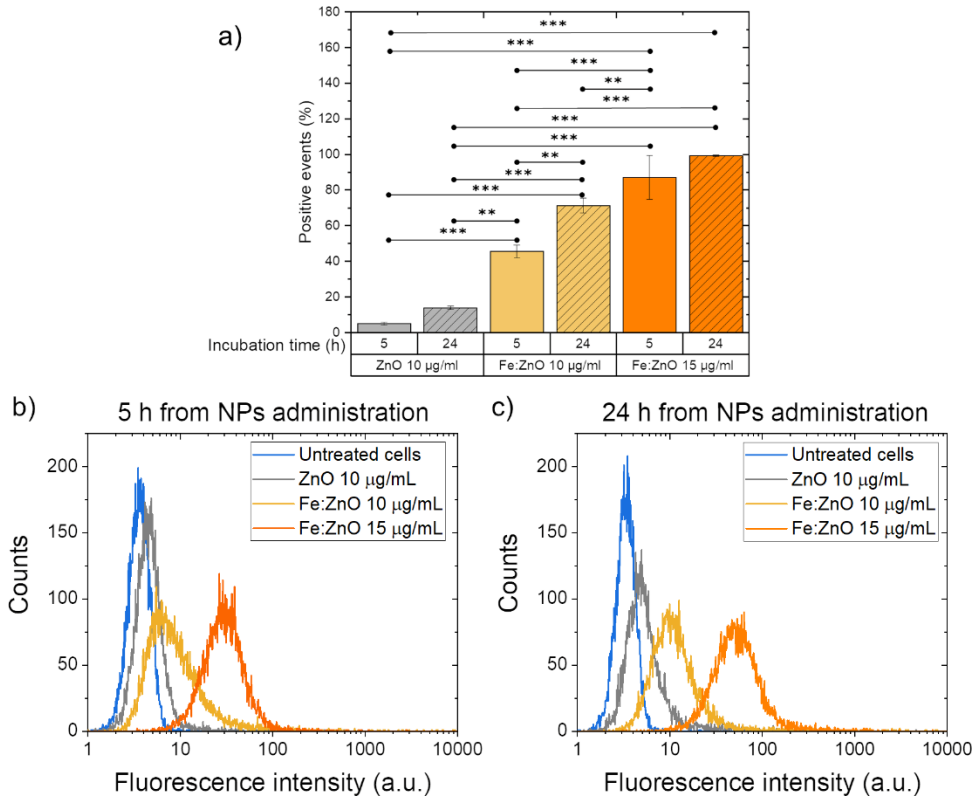


Figure 36: a) BxPC-3 cells measured as positive events due to the internalization or immobilization at the outer cell membrane of ZnO and Fe:ZnO NPs. Data are reported at different incubation times from NPs administration, calculated through cytofluorimetric assays. The values reported by the bars represent the mean ± std.dev. percentage of n = 3 measurements with respect to control cells. The comparisons between the different treatments were performed using two-ways ANOVA. ***$p < 0.001$, **$p < 0.01$ and *$p < 0.05$. Representative histograms of the fluorescence intensity of cells measured through the cytofluorimetric assays exploited to evaluate the NPs internalization at b) 5 h and c) 24 h from NPs administration.

From the results of the cytofluorimetric analysis it can be observed that the percentage of positive events, namely cells with an increased fluorescence, improves with time and dose. In particular, the percentage of cells with a higher fluorescence signal than the control cells approaches 100 % after 24 h from 15 µg/mL Fe:ZnO NPs administration, indicating that all the cells exhibit NPs on their cell membrane or inside of them. This result justifies and supports the use of these NPs dose and incubation time for further mechanical stimulation with shock waves in cells.

Spinning disk confocal fluorescence microscopy was exploited to localize Fe:ZnO NPs inside the cells. Figure 37 reports a representative image of BxPC-3

cells incubated with 15 μg/mL of Fe:ZnO NPs. Despite the nanosized nature of the NPs, which dramatically reduces the possibility to clearly resolve them, it is still possible to locate the presence of some aggregates inside the cells, thus obtaining information about the NPs intracellular location. In particular, the majority of the NPs can be spotted inside the cell membrane but outside the cell nucleus, suggesting that the internalization process allows the permeation of the nanoparticles only inside the cytoplasm.

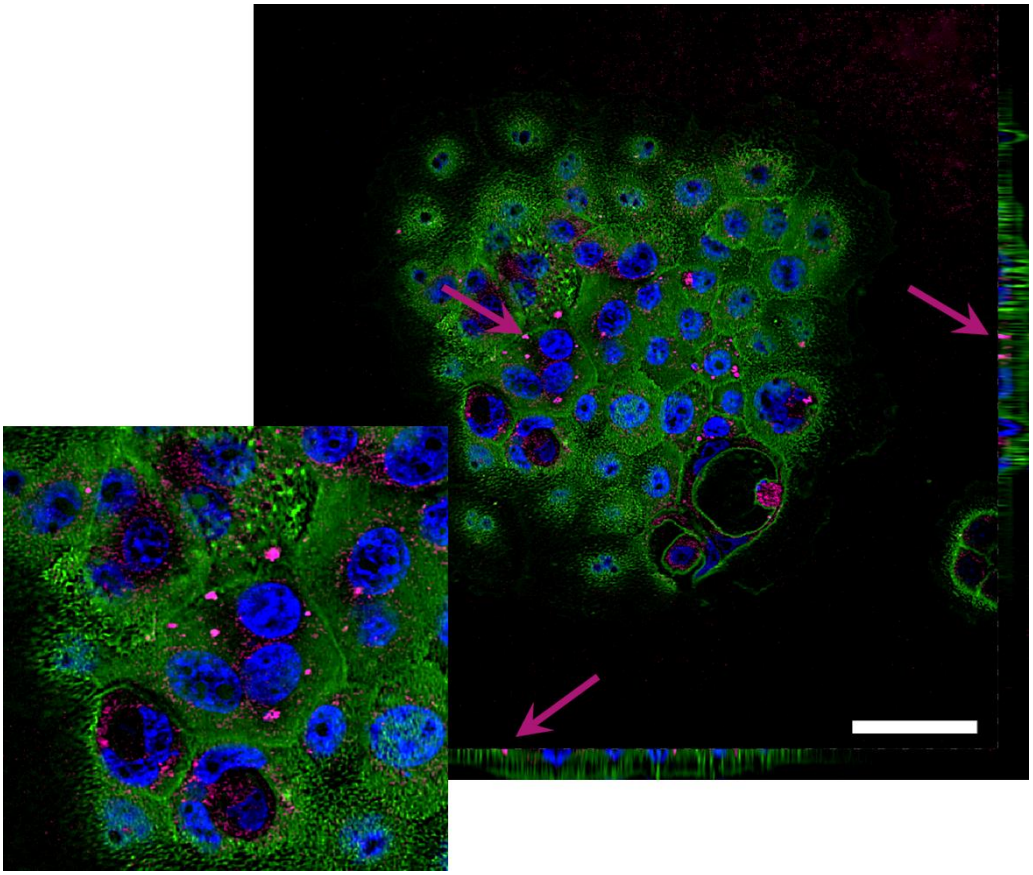

Figure 37: Representative image of Fe:ZnO NPs internalized in BxPC-3 pancreatic cancer cells after 24 h of incubation from NPs administration. Cell membranes (green), nuclei (blue) and Fe:ZnO NPs (purple) are evidenced in the image. Scalebar is 50 μm.

### 3.2.3 Effects of shock waves coupled with Fe:ZnO NPs on pancreatic cancer cells

The final aim of the proposed NPs is to provide a tool that can be externally activated by means of a remote mechanical stimulation, to induce cell death in a diseased tissue. Pancreatic cancer cells were exploited as a tumor model for this purpose. Indeed, the highest safe dose of Fe:ZnO NPs was administered to cells and, after 24 h of incubation, the cells were stimulated with SW in two different conditions: in the presence of NPs internalized in the cells and in the extracellular space, i.e. in cell culture medium (Int+Ext NPs) or with internalized NPs alone (Int NPs).

The cell viability was evaluated after 24 h from NPs incubation and mechanical stimulation (Figure 38). As expected from the cytotoxicity tests, Fe:ZnO NPs are safe when no SWs are co-administered. Furthermore, there is no difference in viability between the cells where only internalized NPs are considered (Fe:ZnO Int) and those where both internalized and non-internalized NPs were retained (Fe:ZnO Int+Ext). Also, the mechanical stimulation with SW does not significantly affect cell viability per se, i.e. when NPs are not administered to cells.

Remarkably, a statistically higher toxicity with respect to the control samples is achieved when the two treatments (i.e., NPs and SW administration) are combined together. In particular, the viability of cells treated with Fe:ZnO Int and SW is 61.8 ± 1.5 % with respect to the untreated cells; furthermore, a statistically relevant difference between this synergistic treatment and either the single NPs administration or the solely SW stimulation is evidenced. When the cells are treated with SW and Fe:ZnO Int+Ext, the viability is 69.6 ± 4.5 % with respect to the control. The difference among the two types of NPs treatments is not statistically significant in terms of cell viability. This result suggests that most of the toxic effects could be attributed to the internalized NPs rather than to the extracellular ones. However, to determine the actual mechanism involved in cell death, further studies are required, as reported below.

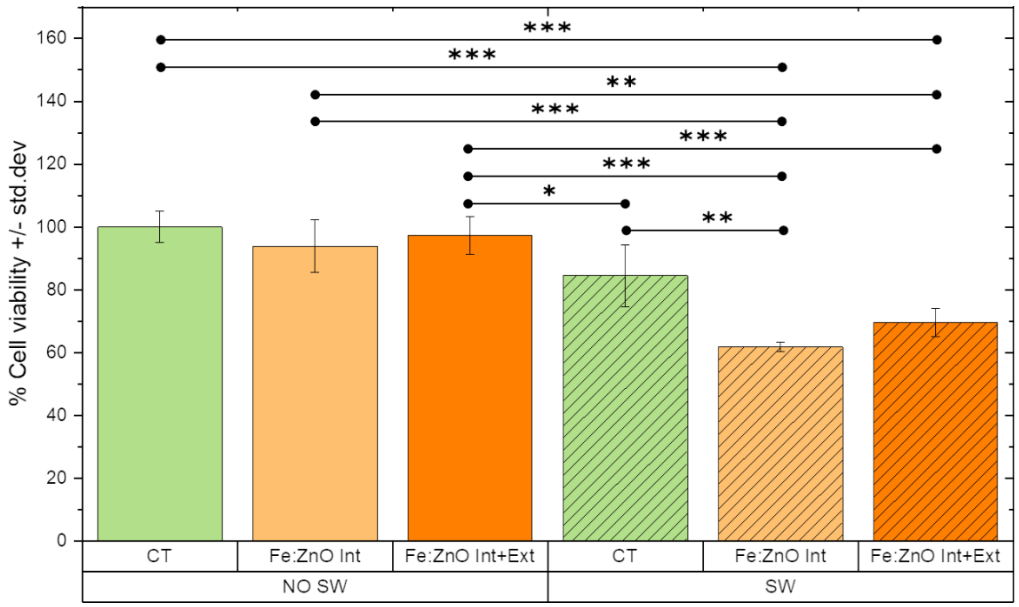


Figure 38: Cell viability percentages with respect to untreated cells of BxPC-3 when treated in presence of Fe:ZnO NPs with SW. The graph shows the difference between Shock Wave-treated (SW in the graph) and untreated (NO SW in the graph) cells and the difference among control cells (CT), cells treated with only internalized NPs (Fe:ZnO Int in the graph) and with NPs both internalized in cells and in the extracellular space (Fe:ZnO Int+Ext in the graph). The values reported by the bars represent the mean ± std.dev percentage of $n \geq 3$ measurements with respect to control cells. The comparisons between the different treatments were performed using three-ways ANOVA. ***$p < 0.001$, **$p < 0.01$ and *$p < 0.05$.

### 3.2.4 Toxicity mechanisms

There are typically three toxicity mechanisms that could be involved in cell death due to the presence of both ZnO NPs and shock waves: (i) ROS generation and consequent oxidative stress; (ii) ZnO dissolution in Zn ions; (iii) mechanical cell membrane disruption due to the mechanical wave and the presence of NPs. Here we have investigated all of them to unravel the mechanism of toxicity due to the combination of NPs and mechanical pressure waves, in the present case SW.

A first analysis was performed to assess the extent of ROS generation contribution to this phenomenon. Ultrasound stimulation has already been reported to induce a high ROS generation due to gas bubble cavitation trapped on the ZnO surface[90]. However, to our knowledge, the effect of repeated shock waves has never been analyzed in these terms. EPR spectroscopy was thus exploited: Fe:ZnO NPs were mechanically stimulated in water and the amount of generated ROS was

analyzed. The results of this measurements (Figure 39) clearly indicate the absence of any signal related to the existence of hydroxyl and alkyl radicals, suggesting that none of these types of ROS are generated due to the SW stimulation, either alone or in combination with NPs. A possible explanation for this phenomenon might be that the frequency of excitation is not suitable to establish any cavitation phenomena, or that the DMPO trap is not sensitive to the specific radicals formed in response to this stimulation. Therefore ROS generation, if potentially present, may not be provoked by the combination of SW and NPs, and thus it is excluded from being the main responsible for cell death.

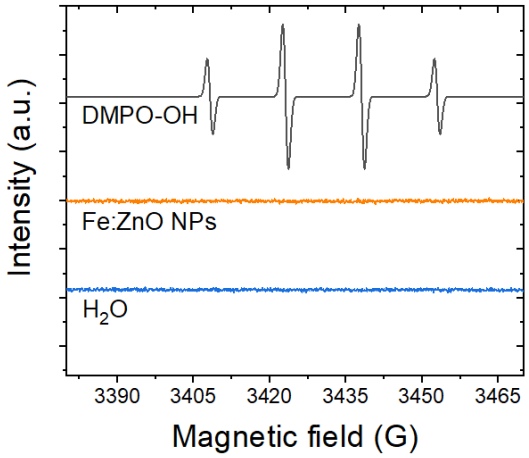


Figure 39: Electron paramagnetic resonance spectroscopy analysis of Fe:ZnO NPs dispersed in water and stimulated with shock waves. The typical spin-adduct of DMPO-OH (an example is reported in the top of the graph) has not been detected both in pure water and in presence of Fe:ZnO NPs (15 μg/ml) after the shock wave stimulation.

A second analysis was performed to evaluate the dissolution of the Fe:ZnO NPs inside cell culture medium, first in absence of SW and then with their mechanical stimulation in the presence of living cells.

Preliminarily, the Zn ions dissolved in RPMI 1640 were measured at different times of incubation at 37 °C, in absence of cells. The results (Figure 40) suggest that the NPs dissolution is almost immediate and approximately corresponding to 60 %, with no relevant differences between the various incubation times. It is therefore assumed that an equilibrium is probably reached very soon in these conditions.

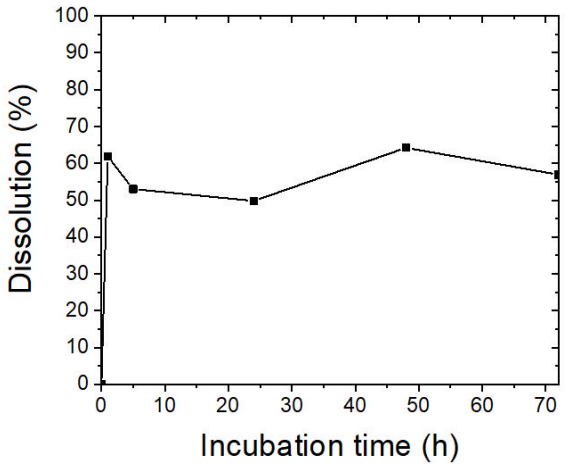


Figure 40: Fe:ZnO NPs dissolution in cell culture medium. The dissolution occurs in the first moments of NPs dispersion in cell culture medium and stabilizes in the first hours of incubation.

Fe:ZnO NPs dissolution and the intracellular permeation of the resulting $Zn^{2+}$ ions were also evaluated through fluorescence microscopy assays. In particular, a fluorescent dye was used to label free zinc inside the cells and another fluorescent dye was exploited to label lysosomes and to determine the location of the retained zinc inside the cell. Figure 41 shows a representative image of a control group of BxPC-3 cells without any NPs treatment, in comparison with Fe:ZnO NPs treated cells. As it can be noticed, the control group already presents a fluorescence signal in the green channel, indicating that Zn ions are physiologically present inside the cells. This is expected from previous literature evidence, being Zn ions important in a series of physiological signalling pathways[375–377], and therefore this fluorescence signal should be considered as a basal level.

When cells are treated with Fe:ZnO NPs, the obtained fluorescence signal corresponding to zinc ions is brighter than the control one. It is clear that Zn ions are released by the nanoparticles and permeate the cells, probably affecting the intracellular homeostasis equilibrium and, in case of an excessive dose, eventually inducing cell death. Another aspect emerged from this analysis is the increase in intensity of the signal related to the lysosomes. Indeed, when cells are treated with NPs, the lysosomes are present in a larger number than in the control cells. If the NPs are trapped in an acid environment as the one distinctive of lysosomes[378–380] they might dissolve because of the well-known instability of ZnO in a low pH solution[75,381]. This phenomenon can explain the partial co-localization of the

lysosome tracker with the zinc related signal. After NPs dissolution, it is very likely that Zn ions diffuse throughout the cell, altering the cell homeostasis and to some extent explaining the partial absence of colocalization between the Zn related signal and the lysosomes' one.

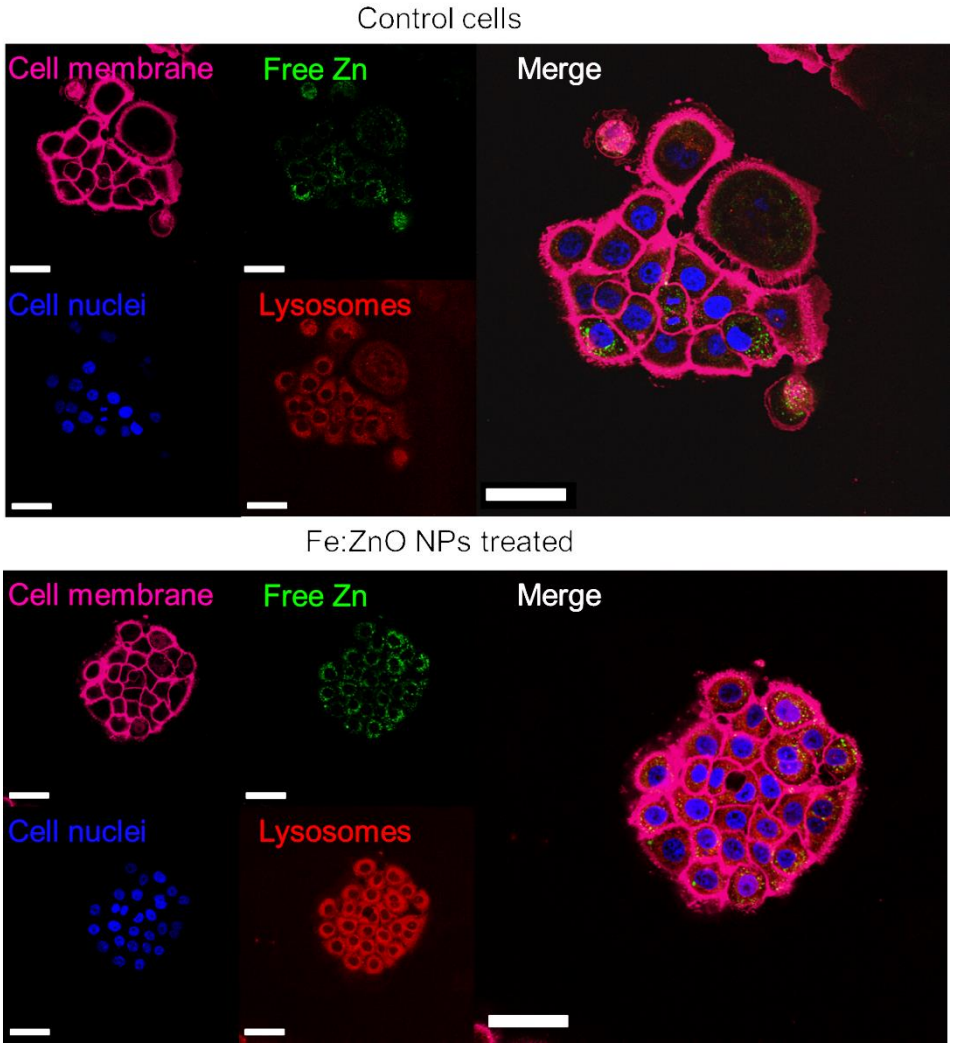


Figure 41: Representative fluorescence microscopy images of BxPC-3 cells treated with Fe:ZnO NPs and control ones. In the images, membranes (purple), nuclei (blue), lysosomes (red) and free zinc inside the cells (green) are referred. Scalebar is 50 μm.

Further information about the fate of cells after the two synergistic treatments can also be obtained by staining cells with both the Zn ions probe and propidium iodide (PI) under fluorescence microscopy (Figure 42). The PI is a cell impermeant

dye, able to emit fluorescence when bound to the DNA. Therefore, it is detectable only when the cell membrane is compromised, therefore allowing the dye to permeate it.

As expected, when no treatments are administered to cells, the signals related to both Zn ions and cell membrane disruption are completely absent. Cells are well adherent to the substrate and viable. The treatment with Fe:ZnO NPs induces an increase in free Zn ions inside the cells, as already noticed in the previous microscopy analyses, but no changes in viability and in cell morphology are observed in this case. The PI signal is completely absent, indicating that the cell membrane is intact, and that cells are not severely suffering for the treatment.

When only the SW are administered to the cells, PI and Zn ions probe signals are also absent. However, the morphology of cells seems slightly rounder than the one observed in the control samples. Anyway, the absence of PI signal indicates that the cell membrane is still intact and therefore cells could be still considered viable.

When both treatments are applied to the cells, the situation dramatically changes. First, it becomes very difficult to find a sufficient number of cells in the field of view. This is due to the pronounced cell death, which causes their removal during the washing steps performed during the staining procedure. The few remaining cells present both the PI and Zn ions related signals. It is therefore possible to suppose that in this case cells are suffering for the treatment. Probably, the Zn ions released by the Fe:ZnO NPs weaken the cell, which in turn becomes more susceptible to the mechanical stimulation. The final result is cell membrane disruption and the resulting cell detachment, which turns to cell death shortly afterwards.

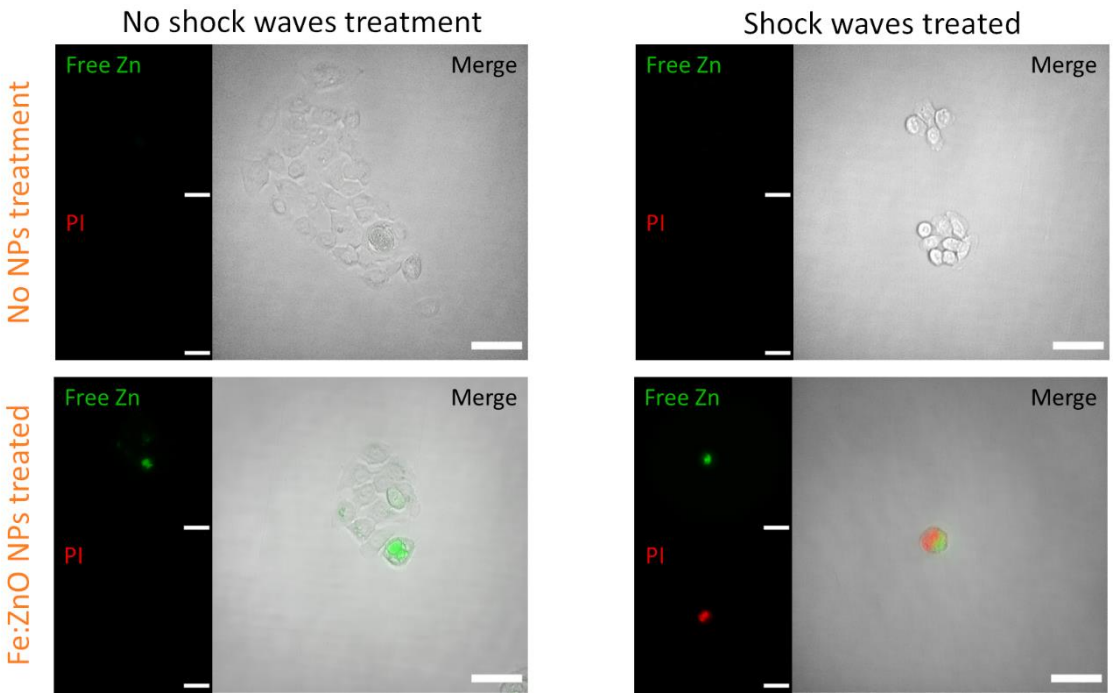


Figure 42: Representative microscopy images of BxPC-3 cells treated with shock waves and Fe:ZnO NPs. The images highlight the phenomena occurring after the treatment with Fe:ZnO NPs and the shock waves in terms of free zinc present in the cells (green) and membrane integrity (red, PI). Only when both the treatments are applied to cells the two signals are clearly visible. Scalebar is 50 μm

A qualitative kinetic analysis of cell death was carried out throughout 24 h of incubation starting from the SW stimulation, evaluating two signals, i.e. luminescence and fluorescence. The results are reported in Figure 43. The luminescence signal is related to the exposure of phosphatidylserine outside the cell membrane, which is reported in the literature to indicate apoptosis[382,383]. Conversely, the fluoresce signal is associated to the secondary necrosis, being it based on a cell-impermeant profluorescent DNA dye which can emit a fluorescence only when cell membrane is broken[94]. This assay allows us to determine cells' death mechanism by the detection of one, both or none of the above-mentioned signals. In the case under analysis in Figure 43, the signals are all referred to the untreated cells' one. As shown, the luminescence signals of cells treated with only Fe:ZnO NPs (orange curves in Figure 43) are slightly higher than the control one. This indicates that cells are not particularly suffering for the NPs administration, being the signal almost constant all along the measurement time. However, the fluorescence signal is lower than the control for all the considered time steps,

excluding the occurrence of necrosis during the incubation time. It is therefore fair to suppose that the cell death mechanism in response to the iron-doped ZnO NPs administration is apoptosis. When cells are treated with SWs alone (blue curves in Figure 43), the situation is slightly different. Indeed, as soon as the SW treatment is completed, both fluorescence and luminescence signals increase with respect to the basal one. This means that there are cells that are going toward alternative forms of cell death, e.g. necrosis, immediately during the treatment. Anyway, despite the luminescence signal remains constant during the 24 hours of analysis, the fluorescence signal initially decreases and raises again only in the last hours of incubation. The reason of this behavior may be attributed to the occurrence of both apoptosis and necrosis at the beginning. Then, the early apoptotic cells undergo late apoptosis, with the consequent secondary increase of the fluorescence signal.

A similar behavior is found for the cells treated with both SW and internalized Fe:ZnO NPs (red curve), which display the increase of both luminescence and fluorescence signals with respect to the basal one. In particular, a slightly enhanced fluorescence signal is reported, qualitatively indicating a higher level of secondary necrosis.

More relevant differences can be found when cells are treated with both SW and Fe:ZnO NPs (both extracellular and intracellular ones), as shown by the violet curves. Indeed, as in the case of SW alone, there is an increase of the luminescence signal just after the SW treatment. However, the increase is notably higher and continues over the first 30 minutes. The signal decreases over time but still indicates a considerable level of apoptotic events. The fluorescence signal is visible from the very beginning and does not underlie differences with respect to the cells treated with SW alone or with SW in the presence of internalized NPs.

In summary, these analyses allow us to hypothesize that a combination of both apoptosis and necrosis mechanisms is occurring in the first 24 hours of NPs incubation after the SW treatment.

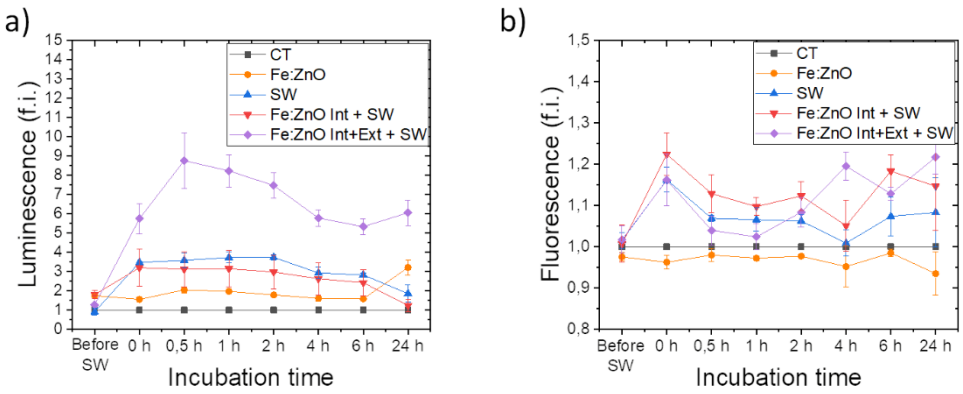


Figure 43: Cell death kinetics after SW treatment, obtained through the apoptosis-necrosis assay. In panel (a), the luminescence is reported as fold induction (f.i.) of the control sample, while panel (b) reports the fluorescence as fold induction of the respective control. Cells belonging to the control sample (CT) were not treated either with Fe:ZnO NPs or SW. BxPC-3 cells were analyzed when incubated with Fe:ZnO NPs (Fe:ZnO sample) without any further treatment, without NPs but treated with SW (SW), treated with SW after a washing aimed at removing the non-internalized NPs that were administered 24 h before (Fe:ZnO Int +SW) and treated with SW after 24 h from Fe:ZnO NPs administration.

Combining all the collected data, it can be assumed that cells die within the first 24 hours due to the synergistic combination of SW and Fe:ZnO NPs. The most important outlined damages could be attributed to cell membrane rupture and ZnO dissolution into cytotoxic Zn cations, whose presence seems to lead to a conspicuous level of cell death.

## 3.4 Conclusions

In the present thesis we report on the use of biocompatible and biodegradable iron-doped ZnO nanoparticles having bioimaging capabilities as magnetic NPs and a pronounced cytotoxic effect when combined with mechanical pressure waves, i.e. shock waves. Both Fe:ZnO NPs and undoped ZnO are chemically synthesized with a sol-gel approach, being capped by oleic acid and functionalized with amino-propyl groups. Actually, these iron-doped NPs show superior features than the undoped ones, having better cytocompatibility and higher internalization rate than the pristine ZnO NPs once tested in an in-vitro model of PDAC. These features

allow their use in a synergistic treatment with SW. In details, two different settings are tested, having the NPs incubated with BxPC-3 cells for 24 hours and evaluating their combination with SW only in the presence of internalized NPs or with both internalized and extracellular nanoparticles. The cytotoxicity results allow us to argue that the most important cytotoxic effects are given by internalized NPs once combined with SW treatment. To better unravel the death mechanisms, different tests point out that Fe:ZnO NPs are prone to dissolve into zinc cations once internalized, inducing the formation of lysosomes and the release of $Zn^{2+}$ ions. On the other hand, shock waves are able to destabilize the cell membrane, inducing its permeation. No ROS detection is however observed, implying that mainly mechanical effects are involved when using SW. Ad hoc cell death analysis further allow us to point out the pronounced apoptotic and necrotic mechanisms of BxPC-3 cell death, ones these cells are exposed to the combination of Fe:ZnO NPs and shock waves for 24 hours.

The obtained proof-of-concept results pave the way for a deeper study towards clinical translation. The advantages of the proposed synergistic activity rely on the use of potentially theranostic NPs having magnetic properties and of an on-demand therapeutic activity once activated by shock waves. In addition, SW allow the ease treatment of deep-seated tumor masses, like pancreatic cancer, opening new perspectives in its therapeutic approach while monitoring the state of the disease. Further improvements are also envisioned to render the proposed NPs even more biomimetic with an organic coating and actively targeting the diseased tissue and its microenvironment, with the final aim of overcoming the high interstitial pressure of this specific tumor mass.

# Chapter 4

# Conclusions and future perspectives

## 4.1 Summary and conclusions

In this PhD thesis the development of a multifunctional theranostic nanosystem is reported from its design to the application in vitro against cancer cells. The final result is an iron doped ZnO nanoparticle with interesting magnetic properties and an in vitro validated therapeutic activity against pancreatic cancer.

The thesis comprehends a first section that highlights the various doping possibilities already present in the literature. In the first Chapter the works reporting various typologies of both doped and undoped ZnO are reviewed and analyzed. In this way, the advantages of doping are highlighted. The theme of the doping element is also deeply considered, and the features gathered by the various doping listed. The final result of the literature review allowed a critical and reasoned choice of the material exploited in this thesis, i.e. iron doped ZnO NPs.

The second Chapter opens to the development of the Fe:ZnO NPs. In this Chapter the synthesis of Fe:ZnO NPs is reported and two levels of doping are compared to the pure ZnO NPs counterparts in terms of physical and chemical properties. The resulting nanomaterials were found to be monocrystalline, spherical nanoparticles in which iron was correctly included in the ZnO crystalline structure. An oleic acid capping was provided on the NP surfaces during the synthesis to increase the stability of the NPs while a post-synthesis functionalization with amino-propyl groups was introduced in the preparation protocol to provide functional groups where dye labelling can be performed in view of in vitro cell culture tests. XPS and EDS analyses were exploited to determine the level of doping of the NPs and iron oxidation state: Iron was successfully included in the ZnO crystal without the formation of any iron clusters, as confirmed by XRD measurements, with a doping level in agreement to the amount of precursors included in the synthesis procedure. Inside the crystal, iron ions assumed both the oxidation states, with a preponderance of one with respect to the other that depends on the doping level. FT-IR spectroscopy was instead exploited to confirm the

success of the functionalization protocol, while DLS and Z-potential measurements were used to determine hydrodynamic radius and surface potential of the NPs in liquid media. Apart from the morphological, crystallographic and chemical features of the three different NPs analyzed, the novel properties gathered by doping were analyzed as well. In view of the diagnosis potentialities of the developed particles, the optical behavior was firstly analyzed. Doping enlarges the light spectral region absorbed by the nanoparticles, including in the absorption spectrum a portion of visible light, with potential applications in photocatalysis. However, the most interesting imaging potentiality rises from the magnetic characterization. As a matter of fact, the presence of the magnetic dipoles included in the crystal with iron doping induces novel magnetic responsiveness to the nanoparticles which could potentially be used for magnetic resonance imaging. From the therapeutic point of view, doping induces an augmented electro-mechanical response which could be efficiently used when the NPs are coupled with a remote mechanical stimulation. The most electro-mechanically responsive NP resulted to be the one with an intermediate level of doping (6 at.% of nominal doping, Fe6:ZnO NPs).

In the third Chapter the application of Fe:ZnO NPs is shown. Pancreatic cancer has been chosen as target for these theranositc NPs because difficulties in the treatment of such a disease requires novel therapeutic approaches. The idea proved in this chapter is to couple Fe:ZnO NPs with shock waves in order to kill cancer cells only when the two treatments are applied together. A pancreatic adenocarcinoma cell line (BxPC-3) has been cultured in vitro and tested with undoped and iron-doped NPs. Preliminary cytotoxicity tests suggested a higher tolerance of the BxPC-3 to Fe:ZnO NPs when compared to pure ZnO NPs, allowing the use of larger doses in view of the coupling of NPs treatment with shock waves. Furthermore, the cytotoxicity tests were also repeated with a non-cancerous cell line, showing a lower toxicity of the developed NPs and in particular of Fe:ZnO NPs toward normal cells. This also indicate a potential intrinsic selectivity of the treatment toward cancer cells killing which enhances the potential of the system for clinical application.

Fe:ZnO NPs internalization studies were also performed on BxPC-3 cells before the application of the mechanical treatment. The results evidences that Fe:ZnO NPs not only can be used in higher doses but also have a greater tendency to be internalized by all cells, expanding the potential effects of further treatments. Fluorescence microscopy studies also highlighted the location of the NPs which were found inside the cell membrane.

The chapter continues with the exploitation of the combined treatment composed of both the administration of the developed NPs and of a mechanical stimulation represented by shock waves. Shock waves are high-energy mechanical pressure waves that are currently used in medicine and that can propagate in depth throughout the human body, representing a valuable tool for remote stimulation of NPs. Therefore, cells were firstly treated with Fe:ZnO NPs and then with SW. Viability tests indicates that a synergistic effect is induced when both the treatments are administered, with a consequent higher percentage of cell death in presence of both NPs and SWs.

This result demonstrates the effectiveness of the Fe:ZnO NPs as a tool against cancer, however the mechanism leading to cell death has also been investigated. Electron paramagnetic resonance spectroscopy analyses allowed to exclude reactive oxygen generation as the main cause leading cell death, therefore the killing mechanisms could be limited to release of $Zn^{2+}$ cations after NPs dissolution in cell culture medium or mechanical damages to the cell membranes due to the Fe:ZnO NPs-SWs treatment. Cell death analysis further allowed to point out the pronounced apoptotic and necrotic mechanisms of BxPC-3 cell death, when the Fe:ZnO NPs-SWs treatment is applied.

As a summary, the developed Fe:ZnO NPs present promising imaging (enhanced magnetic and optical response) and proved therapeutic properties which could be used in several nanomedicine applications. As a proof-of-concept application, the coupling of Fe:ZnO NPs with a remote mechanical stimulation against pancreatic cancer cells has been proved in vitro, paving the way for an actual application in nanomedicine.

## 6.2 Future perspectives

The PhD thesis work here presented shows the development of the NPs from the synthesis to a first validation in cells with in vitro studies. The natural evolution of this work is represented by the application of these NPs in in vivo studies and, after their hopeful success, their application in future clinical studies. Biodistribution studies, effectiveness of magnetic resonance imaging and of course of the synergy between NPs and SWs in vivo would help understand the effects of the NPs on a complete living being. A preliminary step toward in vivo tests could be the administration of Fe:ZnO NPs to 3D cell cultures, in order to deepen the

understanding of the effect of the mechanical stimulation on the cells and the synergy between NPs and SWs.

Still, this work proved the potential efficacy of this kind of therapy but could take advantage of further functionalization that could improve even more the safety and the efficacy of the system. An example could be the coating of the nanoparticles with a lipidic shell which could enhance the biostability of the nanoconstuct, leading to the possibility of increasing the dose exploited and potentially its therapeutic effect.

Moreover, despite an intrinsic selectivity in killing cancerous cells rather than normal cells, a more precise targeting mechanism could result in a safer and efficient device. For this reason, in future, NPs could be functionalized with targeting peptides or antibody having as target some specific overexpressed protein in cancer cell membranes.

Finally, even if not explicitly analyzed in this thesis, the enhanced electro-mechanical response of the iron-doped ZnO NPs could be exploited in tissue engineering where the electric potential generated by the NPs upon mechanical stimulation could excite and induce tissue growth or differentiation in electrically sensitive tissues like bone, muscular or nervous cells.

# References


(1) Carofiglio, M.; Barui, S.; Cauda, V.; Laurenti, M. Doped Zinc Oxide Nanoparticles: Synthesis, Characterization and Potential Use in Nanomedicine. *Applied Sciences* **2020**, *10* (15), 5194. https://doi.org/10.3390/app10155194.

(2) Genchi, G. G.; Marino, A.; Tapeinos, C.; Ciofani, G. Smart Materials Meet Multifunctional Biomedical Devices: Current and Prospective Implications for Nanomedicine. *Frontiers in Bioengineering and Biotechnology* **2017**, *5*.

(3) Patra, J. K.; Das, G.; Fraceto, L. F.; Campos, E. V. R.; Rodriguez-Torres, M. del P.; Acosta-Torres, L. S.; Diaz-Torres, L. A.; Grillo, R.; Swamy, M. K.; Sharma, S.; Habtemariam, S.; Shin, H.-S. Nano Based Drug Delivery Systems: Recent Developments and Future Prospects. *Journal of Nanobiotechnology* **2018**, *16* (1), 71. https://doi.org/10.1186/s12951-018-0392-8.

(4) Singh, R.; Lillard, J. W. Nanoparticle-Based Targeted Drug Delivery. *Experimental and Molecular Pathology* **2009**, *86* (3), 215–223. https://doi.org/10.1016/j.yexmp.2008.12.004.

(5) He, X.; Li, J.; An, S.; Jiang, C. PH-Sensitive Drug-Delivery Systems for Tumor Targeting. *Therapeutic Delivery* **2013**, *4* (12), 1499–1510. https://doi.org/10.4155/tde.13.120.

(6) Raza, A.; Hayat, U.; Rasheed, T.; Bilal, M.; Iqbal, H. M. N. "Smart" Materials-Based near-Infrared Light-Responsive Drug Delivery Systems for Cancer Treatment: A Review. *Journal of Materials Research and Technology* **2019**, *8* (1), 1497–1509. https://doi.org/10.1016/j.jmrt.2018.03.007.

(7) Boissenot, T.; Bordat, A.; Fattal, E.; Tsapis, N. Ultrasound-Triggered Drug Delivery for Cancer Treatment Using Drug Delivery Systems: From Theoretical Considerations to Practical Applications. *Journal of Controlled Release* **2016**, *241*, 144–163. https://doi.org/10.1016/j.jconrel.2016.09.026.

(8) Huh, A. J.; Kwon, Y. J. "Nanoantibiotics": A New Paradigm for Treating Infectious Diseases Using Nanomaterials in the Antibiotics Resistant Era. *Journal of Controlled Release* **2011**, *156* (2), 128–145. https://doi.org/10.1016/j.jconrel.2011.07.002.

(9) Lee, N.-Y.; Ko, W.-C.; Hsueh, P.-R. Nanoparticles in the Treatment of Infections Caused by Multidrug-Resistant Organisms. *Frontiers in Pharmacology* **2019**, *10*.

(10) Aghebati-Maleki, A.; Dolati, S.; Ahmadi, M.; Baghbanzhadeh, A.; Asadi, M.; Fotouhi, A.; Yousefi, M.; Aghebati-Maleki, L. Nanoparticles and Cancer Therapy: Perspectives for Application of Nanoparticles in the Treatment of Cancers. *Journal of Cellular Physiology* **2020**, *235* (3), 1962–1972. https://doi.org/10.1002/jcp.29126.

(11) Wang, Y.-F.; Liu, L.; Xue, X.; Liang, X.-J. Nanoparticle-Based Drug Delivery Systems: What Can They Really Do *in Vivo*? F1000Research May 16, 2017. https://doi.org/10.12688/f1000research.9690.1.

(12) Laurenti, M.; Stassi, S.; Canavese, G.; Cauda, V. Surface Engineering of Nanostructured ZnO Surfaces. *Advanced Materials Interfaces* **2017**, *4* (2), 1600758. https://doi.org/10.1002/admi.201600758.

(13) Mout, R.; Moyano, D. F.; Rana, S.; Rotello, V. M. Surface Functionalization of Nanoparticles for Nanomedicine. *Chem. Soc. Rev.* **2012**, *41* (7), 2539–2544. https://doi.org/10.1039/C2CS15294K.

(14) Su, Y.-L.; Hu, S.-H. Functional Nanoparticles for Tumor Penetration of Therapeutics. *Pharmaceutics* **2018**, *10* (4), 193. https://doi.org/10.3390/pharmaceutics10040193.

(15) Wang, M.; Thanou, M. Targeting Nanoparticles to Cancer. *Pharmacological Research* **2010**, *62* (2), 90–99. https://doi.org/10.1016/j.phrs.2010.03.005.

(16) Sunoqrot, S.; Bugno, J.; Lantvit, D.; Burdette, J. E.; Hong, S. Prolonged Blood Circulation and Enhanced Tumor Accumulation of Folate-Targeted Dendrimer-Polymer Hybrid Nanoparticles. *Journal of Controlled Release* **2014**, *191*, 115–122. https://doi.org/10.1016/j.jconrel.2014.05.006.

(17) Larsen, E. K. U.; Nielsen, T.; Wittenborn, T.; Birkedal, H.; Vorup-Jensen, T.; Jakobsen, M. H.; Østergaard, L.; Horsman, M. R.; Besenbacher, F.; Howard, K. A.; Kjems, J. Size-Dependent Accumulation of PEGylated Silane-Coated Magnetic Iron Oxide Nanoparticles in Murine Tumors. *ACS Nano* **2009**, *3* (7), 1947–1951. https://doi.org/10.1021/nn900330m.

(18) Hans, M. L.; Lowman, A. M. Biodegradable Nanoparticles for Drug Delivery and Targeting. *Current Opinion in Solid State and Materials Science* **2002**, *6* (4), 319–327. https://doi.org/10.1016/S1359-0286(02)00117-1.

(19) Shargh, V. H.; Hondermarck, H.; Liang, M. Antibody-Targeted Biodegradable Nanoparticles for Cancer Therapy. *Nanomedicine* **2016**, *11* (1), 63–79. https://doi.org/10.2217/nnm.15.186.

(20) Nune, S. K.; Gunda, P.; Thallapally, P. K.; Lin, Y.-Y.; Laird Forrest, M.; Berkland, C. J. Nanoparticles for Biomedical Imaging. *Expert Opinion on Drug*

*Delivery* **2009**, *6* (11), 1175–1194. https://doi.org/10.1517/17425240903229031.

(21) Wolfbeis, O. S. An Overview of Nanoparticles Commonly Used in Fluorescent Bioimaging. *Chem. Soc. Rev.* **2015**, *44* (14), 4743–4768. https://doi.org/10.1039/C4CS00392F.

(22) Boschi, F.; Sanctis, F. D. Overview of the Optical Properties of Fluorescent Nanoparticles for Optical Imaging. *European Journal of Histochemistry* **2017**, *61* (3). https://doi.org/10.4081/ejh.2017.2830.

(23) Sun, C.; Lee, J. S. H.; Zhang, M. Magnetic Nanoparticles in MR Imaging and Drug Delivery. *Advanced Drug Delivery Reviews* **2008**, *60* (11), 1252–1265. https://doi.org/10.1016/j.addr.2008.03.018.

(24) Varna, M.; Xuan, H. V.; Fort, E. Gold Nanoparticles in Cardiovascular Imaging. *WIREs Nanomedicine and Nanobiotechnology* **2018**, *10* (1), e1470. https://doi.org/10.1002/wnan.1470.

(25) Xie, J.; Lee, S.; Chen, X. Nanoparticle-Based Theranostic Agents. *Advanced Drug Delivery Reviews* **2010**, *62* (11), 1064–1079. https://doi.org/10.1016/j.addr.2010.07.009.

(26) Akhter, S.; Ahmad, M. Z.; Ahmad, F. J.; Storm, G.; Kok, R. J. Gold Nanoparticles in Theranostic Oncology: Current State-of-the-Art. *Expert Opinion on Drug Delivery* **2012**, *9* (10), 1225–1243. https://doi.org/10.1517/17425247.2012.716824.

(27) Janib, S. M.; Moses, A. S.; MacKay, J. A. Imaging and Drug Delivery Using Theranostic Nanoparticles. *Advanced Drug Delivery Reviews* **2010**, *62* (11), 1052–1063. https://doi.org/10.1016/j.addr.2010.08.004.

(28) Gharatape, A.; Salehi, R. Recent Progress in Theranostic Applications of Hybrid Gold Nanoparticles. *European Journal of Medicinal Chemistry* **2017**, *138*, 221–233. https://doi.org/10.1016/j.ejmech.2017.06.034.

(29) Singh, A.; Sahoo, S. K. Magnetic Nanoparticles: A Novel Platform for Cancer Theranostics. *Drug Discovery Today* **2014**, *19* (4), 474–481. https://doi.org/10.1016/j.drudis.2013.10.005.

(30) Yoo, D.; Lee, J.-H.; Shin, T.-H.; Cheon, J. Theranostic Magnetic Nanoparticles. *Acc. Chem. Res.* **2011**, *44* (10), 863–874. https://doi.org/10.1021/ar200085c.

(31) Ren, X.; Chen, H.; Yang, V.; Sun, D. Iron Oxide Nanoparticle-Based Theranostics for Cancer Imaging and Therapy. *Front. Chem. Sci. Eng.* **2014**, *8* (3), 253–264. https://doi.org/10.1007/s11705-014-1425-y.

(32) Martín-Saavedra, F. M.; Ruíz-Hernández, E.; Boré, A.; Arcos, D.; Vallet-Regí, M.; Vilaboa, N. Magnetic Mesoporous Silica Spheres for Hyperthermia

Therapy. *Acta Biomaterialia* **2010**, *6* (12), 4522–4531. https://doi.org/10.1016/j.actbio.2010.06.030.

(33) Yao, X.; Niu, X.; Ma, K.; Huang, P.; Grothe, J.; Kaskel, S.; Zhu, Y. Graphene Quantum Dots-Capped Magnetic Mesoporous Silica Nanoparticles as a Multifunctional Platform for Controlled Drug Delivery, Magnetic Hyperthermia, and Photothermal Therapy. *Small* **2017**, *13* (2), 1602225. https://doi.org/10.1002/smll.201602225.

(34) Tian, Z.; Yu, X.; Ruan, Z.; Zhu, M.; Zhu, Y.; Hanagata, N. Magnetic Mesoporous Silica Nanoparticles Coated with Thermo-Responsive Copolymer for Potential Chemo- and Magnetic Hyperthermia Therapy. *Microporous and Mesoporous Materials* **2018**, *256*, 1–9. https://doi.org/10.1016/j.micromeso.2017.07.053.

(35) Elbialy, N. S.; Fathy, M. M.; AL-Wafi, R.; Darwesh, R.; Abdel-dayem, U. A.; Aldhahri, M.; Noorwali, A.; AL-ghamdi, A. A. Multifunctional Magnetic-Gold Nanoparticles for Efficient Combined Targeted Drug Delivery and Interstitial Photothermal Therapy. *International Journal of Pharmaceutics* **2019**, *554*, 256–263. https://doi.org/10.1016/j.ijpharm.2018.11.021.

(36) Jia, T.; Xu, J.; Dong, S.; He, F.; Zhong, C.; Yang, G.; Bi, H.; Xu, M.; Hu, Y.; Yang, D.; Yang, P.; Lin, J. Mesoporous Cerium Oxide-Coated Upconversion Nanoparticles for Tumor-Responsive Chemo-Photodynamic Therapy and Bioimaging. *Chem. Sci.* **2019**, *10* (37), 8618–8633. https://doi.org/10.1039/C9SC01615E.

(37) Amirshaghaghi, A.; Yan, L.; Miller, J.; Daniel, Y.; Stein, J. M.; Busch, T. M.; Cheng, Z.; Tsourkas, A. Chlorin E6-Coated Superparamagnetic Iron Oxide Nanoparticle (SPION) Nanoclusters as a Theranostic Agent for Dual-Mode Imaging and Photodynamic Therapy. *Sci Rep* **2019**, *9* (1), 2613. https://doi.org/10.1038/s41598-019-39036-1.

(38) Zhang, L.; Webster, T. J. Nanotechnology and Nanomaterials: Promises for Improved Tissue Regeneration. *Nano Today* **2009**, *4* (1), 66–80. https://doi.org/10.1016/j.nantod.2008.10.014.

(39) Armentano, I.; Dottori, M.; Fortunati, E.; Mattioli, S.; Kenny, J. M. Biodegradable Polymer Matrix Nanocomposites for Tissue Engineering: A Review. *Polymer Degradation and Stability* **2010**, *95* (11), 2126–2146. https://doi.org/10.1016/j.polymdegradstab.2010.06.007.

(40) Ku, S. H.; Lee, M.; Park, C. B. Carbon-Based Nanomaterials for Tissue Engineering. *Advanced Healthcare Materials* **2013**, *2* (2), 244–260. https://doi.org/10.1002/adhm.201200307.

(41) Goenka, S.; Sant, V.; Sant, S. Graphene-Based Nanomaterials for Drug Delivery and Tissue Engineering. *Journal of Controlled Release* **2014**, *173*, 75–88. https://doi.org/10.1016/j.jconrel.2013.10.017.

(42) Rosenholm, J. M.; Zhang, J.; Linden, M.; Sahlgren, C. Mesoporous Silica Nanoparticles in Tissue Engineering – a Perspective. *Nanomedicine* **2016**, *11* (4), 391–402. https://doi.org/10.2217/nnm.15.212.

(43) Kumar, V. V.; Anthony, S. P. Chapter 9 - Antimicrobial Studies of Metal and Metal Oxide Nanoparticles. In *Surface Chemistry of Nanobiomaterials*; Grumezescu, A. M., Ed.; William Andrew Publishing, 2016; pp 265–300. https://doi.org/10.1016/B978-0-323-42861-3.00009-1.

(44) Marino, A.; Genchi, G. G.; Mattoli, V.; Ciofani, G. Piezoelectric Nanotransducers: The Future of Neural Stimulation. *Nano Today* **2017**, *14*, 9–12. https://doi.org/10.1016/j.nantod.2016.12.005.

(45) Murillo, G.; Blanquer, A.; Vargas-Estevez, C.; Barrios, L.; Ibáñez, E.; Nogués, C.; Esteve, J. Electromechanical Nanogenerator–Cell Interaction Modulates Cell Activity. *Advanced Materials* **2017**, *29* (24), 1605048. https://doi.org/10.1002/adma.201605048.

(46) Zwi-Dantsis, L.; Wang, B.; Marijon, C.; Zonetti, S.; Ferrini, A.; Massi, L.; Stuckey, D. J.; Terracciano, C. M.; Stevens, M. M. Remote Magnetic Nanoparticle Manipulation Enables the Dynamic Patterning of Cardiac Tissues. *Advanced Materials* **2020**, *32* (6), 1904598. https://doi.org/10.1002/adma.201904598.

(47) Vallet-Regí, M.; Colilla, M.; Izquierdo-Barba, I.; Manzano, M. Mesoporous Silica Nanoparticles for Drug Delivery: Current Insights. *Molecules* **2018**, *23* (1), 47. https://doi.org/10.3390/molecules23010047.

(48) Wu, S.-H.; Hung, Y.; Mou, C.-Y. Mesoporous Silica Nanoparticles as Nanocarriers. *Chem. Commun.* **2011**, *47* (36), 9972–9985. https://doi.org/10.1039/C1CC11760B.

(49) Vallet-Regí, M. Ordered Mesoporous Materials in the Context of Drug Delivery Systems and Bone Tissue Engineering. *Chemistry – A European Journal* **2006**, *12* (23), 5934–5943. https://doi.org/10.1002/chem.200600226.

(50) Das, S.; Dowding, J. M.; Klump, K. E.; McGinnis, J. F.; Self, W.; Seal, S. Cerium Oxide Nanoparticles: Applications and Prospects in Nanomedicine. *Nanomedicine* **2013**, *8* (9), 1483–1508. https://doi.org/10.2217/nnm.13.133.

(51) Hirst, S. M.; Karakoti, A. S.; Tyler, R. D.; Sriranganathan, N.; Seal, S.; Reilly, C. M. Anti-Inflammatory Properties of Cerium Oxide Nanoparticles. *Small* **2009**, *5* (24), 2848–2856. https://doi.org/10.1002/smll.200901048.

(52) Rajeshkumar, S.; Naik, P. Synthesis and Biomedical Applications of Cerium Oxide Nanoparticles – A Review. *Biotechnology Reports* **2018**, *17*, 1–5. https://doi.org/10.1016/j.btre.2017.11.008.

(53) Rosen, J. E.; Chan, L.; Shieh, D.-B.; Gu, F. X. Iron Oxide Nanoparticles for Targeted Cancer Imaging and Diagnostics. *Nanomedicine: Nanotechnology, Biology and Medicine* **2012**, *8* (3), 275–290. https://doi.org/10.1016/j.nano.2011.08.017.

(54) El-Boubbou, K. Magnetic Iron Oxide Nanoparticles as Drug Carriers: Clinical Relevance. *Nanomedicine* **2018**, *13* (8), 953–971. https://doi.org/10.2217/nnm-2017-0336.

(55) Hilger, I.; Kaiser, W. A. Iron Oxide-Based Nanostructures for MRI and Magnetic Hyperthermia. *Nanomedicine* **2012**, *7* (9), 1443–1459. https://doi.org/10.2217/nnm.12.112.

(56) Racca, L.; Canta, M.; Dumontel, B.; Ancona, A.; Limongi, T.; Garino, N.; Laurenti, M.; Canavese, G.; Cauda, V. 12 - Zinc Oxide Nanostructures in Biomedicine. In *Smart Nanoparticles for Biomedicine*; Ciofani, G., Ed.; Micro and Nano Technologies; Elsevier, 2018; pp 171–187. https://doi.org/10.1016/B978-0-12-814156-4.00012-4.

(57) Espitia, P. J. P.; Otoni, C. G.; Soares, N. F. F. Chapter 34 - Zinc Oxide Nanoparticles for Food Packaging Applications. In *Antimicrobial Food Packaging*; Barros-Velázquez, J., Ed.; Academic Press: San Diego, 2016; pp 425–431. https://doi.org/10.1016/B978-0-12-800723-5.00034-6.

(58) Lee, K. M.; Lai, C. W.; Ngai, K. S.; Juan, J. C. Recent Developments of Zinc Oxide Based Photocatalyst in Water Treatment Technology: A Review. *Water Research* **2016**, *88*, 428–448. https://doi.org/10.1016/j.watres.2015.09.045.

(59) Laurenti, M.; Garino, N.; Canavese, G.; Hernandéz, S.; Cauda, V. Piezo- and Photocatalytic Activity of Ferroelectric ZnO:Sb Thin Films for the Efficient Degradation of Rhodamine-β Dye Pollutant. *ACS Appl. Mater. Interfaces* **2020**, *12* (23), 25798–25808. https://doi.org/10.1021/acsami.0c03787.

(60) Lops, C.; Ancona, A.; Di Cesare, K.; Dumontel, B.; Garino, N.; Canavese, G.; Hérnandez, S.; Cauda, V. Sonophotocatalytic Degradation Mechanisms of Rhodamine B Dye via Radicals Generation by Micro- and Nano-Particles of ZnO. *Applied Catalysis B: Environmental* **2019**, *243*, 629–640. https://doi.org/10.1016/j.apcatb.2018.10.078.

(61) Laurenti, M.; Stassi, S.; Lorenzoni, M.; Fontana, M.; Canavese, G.; Cauda, V.; Pirri, C. F. Evaluation of the Piezoelectric Properties and Voltage

Generation of Flexible Zinc Oxide Thin Films. *Nanotechnology* **2015**, *26* (21), 215704. https://doi.org/10.1088/0957-4484/26/21/215704.

(62) Laurenti, M.; Canavese, G.; Stassi, S.; Fontana, M.; Castellino, M.; Pirri, C. F.; Cauda, V. A Porous Nanobranched Structure: An Effective Way to Improve Piezoelectricity in Sputtered ZnO Thin Films. *RSC Adv.* **2016**, *6* (80), 76996–77004. https://doi.org/10.1039/C6RA17319E.

(63) Liu, J.; Fernández-Serra, M. V.; Allen, P. B. First-Principles Study of Pyroelectricity in GaN and ZnO. *Phys. Rev. B* **2016**, *93* (8), 081205. https://doi.org/10.1103/PhysRevB.93.081205.

(64) Marco Laurenti; Valentina Cauda. Porous Zinc Oxide Thin Films: Synthesis Approaches and Applications. *Coatings* **2018**, *8* (2), 67. https://doi.org/10.3390/coatings8020067.

(65) Znaidi, L. Sol–Gel-Deposited ZnO Thin Films: A Review. *Materials Science and Engineering: B* **2010**, *174* (1), 18–30. https://doi.org/10.1016/j.mseb.2010.07.001.

(66) Bagga, S.; Akhtar, J.; Mishra, S. Synthesis and Applications of ZnO Nanowire: A Review. *AIP Conference Proceedings* **2018**, *1989* (1), 020004. https://doi.org/10.1063/1.5047680.

(67) Yi, G.-C.; Wang, C.; Park, W. I. ZnO Nanorods: Synthesis, Characterization and Applications. *Semicond. Sci. Technol.* **2005**, *20* (4), S22–S34. https://doi.org/10.1088/0268-1242/20/4/003.

(68) Li, Y. B.; Bando, Y.; Sato, T.; Kurashima, K. ZnO Nanobelts Grown on Si Substrate. *Appl. Phys. Lett.* **2002**, *81* (1), 144–146. https://doi.org/10.1063/1.1492008.

(69) Garino, N.; Limongi, T.; Dumontel, B.; Canta, M.; Racca, L.; Laurenti, M.; Castellino, M.; Casu, A.; Falqui, A.; Cauda, V. A Microwave-Assisted Synthesis of Zinc Oxide Nanocrystals Finely Tuned for Biological Applications. *Nanomaterials* **2019**, *9* (2), 212. https://doi.org/10.3390/nano9020212.

(70) Cauda, V.; Pugliese, D.; Garino, N.; Sacco, A.; Bianco, S.; Bella, F.; Lamberti, A.; Gerbaldi, C. Multi-Functional Energy Conversion and Storage Electrodes Using Flower-like Zinc Oxide Nanostructures. *Energy* **2014**, *65*, 639–646. https://doi.org/10.1016/j.energy.2013.12.025.

(71) Laurenti, M.; Cauda, V. ZnO Nanostructures for Tissue Engineering Applications. *Nanomaterials* **2017**, *7* (11), 374. https://doi.org/10.3390/nano7110374.

(72) Ciofani, G.; Genchi, G. G.; Mattoli, V. ZnO Nanowire Arrays as Substrates for Cell Proliferation and Differentiation. *Materials Science and Engineering: C* **2012**, *32* (2), 341–347. https://doi.org/10.1016/j.msec.2011.11.001.

(73) Lee, J.; Kang, B. S.; Hicks, B.; Chancellor, T. F.; Chu, B. H.; Wang, H.-T.; Keselowsky, B. G.; Ren, F.; Lele, T. P. The Control of Cell Adhesion and Viability by Zinc Oxide Nanorods. *Biomaterials* **2008**, *29* (27), 3743–3749. https://doi.org/10.1016/j.biomaterials.2008.05.029.

(74) Park, J. K.; Kim, Y.-J.; Yeom, J.; Jeon, J. H.; Yi, G.-C.; Je, J. H.; Hahn, S. K. The Topographic Effect of Zinc Oxide Nanoflowers on Osteoblast Growth and Osseointegration. *Advanced Materials* **2010**, *22* (43), 4857–4861. https://doi.org/10.1002/adma.201002255.

(75) Dumontel, B.; Canta, M.; Engelke, H.; Chiodoni, A.; Racca, L.; Ancona, A.; Limongi, T.; Canavese, G.; Cauda, V. Enhanced Biostability and Cellular Uptake of Zinc Oxide Nanocrystals Shielded with a Phospholipid Bilayer. *J. Mater. Chem. B* **2017**, *5* (44), 8799–8813. https://doi.org/10.1039/C7TB02229H.

(76) Ahtzaz, S.; Nasir, M.; Shahzadi, L.; Amir, W.; Anjum, A.; Arshad, R.; Iqbal, F.; Chaudhry, A. A.; Yar, M.; Rehman, I. ur. A Study on the Effect of Zinc Oxide and Zinc Peroxide Nanoparticles to Enhance Angiogenesis-pro-Angiogenic Grafts for Tissue Regeneration Applications. *Materials & Design* **2017**, *132*, 409–418. https://doi.org/10.1016/j.matdes.2017.07.023.

(77) Garino, N.; Sanvitale, P.; Dumontel, B.; Laurenti, M.; Colilla, M.; Izquierdo-Barba, I.; Cauda, V.; Vallet-Regì, M. Zinc Oxide Nanocrystals as a Nanoantibiotic and Osteoinductive Agent. *RSC Adv.* **2019**, *9* (20), 11312–11321. https://doi.org/10.1039/C8RA10236H.

(78) Marco Laurenti; Valentina Cauda. Gentamicin-Releasing Mesoporous ZnO Structures. *Materials* **2018**, *11* (2), 314. https://doi.org/10.3390/ma11020314.

(79) Laurenti, M.; Lamberti, A.; Genchi, G. G.; Roppolo, I.; Canavese, G.; Vitale-Brovarone, C.; Ciofani, G.; Cauda, V. Graphene Oxide Finely Tunes the Bioactivity and Drug Delivery of Mesoporous ZnO Scaffolds. *ACS Appl. Mater. Interfaces* **2019**, *11* (1), 449–456. https://doi.org/10.1021/acsami.8b20728.

(80) Xiong, H.-M. ZnO Nanoparticles Applied to Bioimaging and Drug Delivery. *Advanced Materials* **2013**, *25* (37), 5329–5335. https://doi.org/10.1002/adma.201301732.

(81) Muhammad, F.; Guo, M.; Qi, W.; Sun, F.; Wang, A.; Guo, Y.; Zhu, G. PH-Triggered Controlled Drug Release from Mesoporous Silica Nanoparticles via Intracelluar Dissolution of ZnO Nanolids. *J. Am. Chem. Soc.* **2011**, *133* (23), 8778–8781. https://doi.org/10.1021/ja200328s.

(82) Bakrudeen, H. B.; Tsibouklis, J.; Reddy, B. S. R. Facile Fabrication of Mesoporous ZnO Nanospheres for the Controlled Delivery of Captopril. *J Nanopart Res* **2013**, *15* (3), 1505. https://doi.org/10.1007/s11051-013-1505-9.

(83) Kumar, V. B.; Kumar, K.; Gedanken, A.; Paik, P. Facile Synthesis of Self-Assembled Spherical and Mesoporous Dandelion Capsules of ZnO: Efficient Carrier for DNA and Anti-Cancer Drugs. *J. Mater. Chem. B* **2014**, *2* (25), 3956–3964. https://doi.org/10.1039/C4TB00416G.

(84) Patra, P.; Mitra, S.; Das Gupta, A.; Pradhan, S.; Bhattacharya, S.; Ahir, M.; Mukherjee, S.; Sarkar, S.; Roy, S.; Chattopadhyay, S.; Adhikary, A.; Goswami, A.; Chattopadhyay, D. Simple Synthesis of Biocompatible Biotinylated Porous Hexagonal ZnO Nanodisc for Targeted Doxorubicin Delivery against Breast Cancer Cell: In Vitro and in Vivo Cytotoxic Potential. *Colloids and Surfaces B: Biointerfaces* **2015**, *133*, 88–98. https://doi.org/10.1016/j.colsurfb.2015.05.052.

(85) Hsu, S.; Lin, Y. Y.; Huang, S.; Lem, K. W.; Nguyen, D. H.; Lee, D. S. Synthesis of Water-Dispersible Zinc Oxide Quantum Dots with Antibacterial Activity and Low Cytotoxicity for Cell Labeling. *Nanotechnology* **2013**, *24* (47), 475102. https://doi.org/10.1088/0957-4484/24/47/475102.

(86) Ma, Y.-Y.; Ding, H.; Xiong, H.-M. Folic Acid Functionalized ZnO Quantum Dots for Targeted Cancer Cell Imaging. *Nanotechnology* **2015**, *26* (30), 305702. https://doi.org/10.1088/0957-4484/26/30/305702.

(87) Chen, H.; Zhang, M.; Li, B.; Chen, D.; Dong, X.; Wang, Y.; Gu, Y. Versatile Antimicrobial Peptide-Based ZnO Quantum Dots for in Vivo Bacteria Diagnosis and Treatment with High Specificity. *Biomaterials* **2015**, *53*, 532–544. https://doi.org/10.1016/j.biomaterials.2015.02.105.

(88) Bisht, G.; Rayamajhi, S. ZnO Nanoparticles: A Promising Anticancer Agent. *Nanobiomedicine* **2016**, *3*, 9. https://doi.org/10.5772/63437.

(89) Wang, J.; Lee, J. S.; Kim, D.; Zhu, L. Exploration of Zinc Oxide Nanoparticles as a Multitarget and Multifunctional Anticancer Nanomedicine. *ACS Appl. Mater. Interfaces* **2017**, *9* (46), 39971–39984. https://doi.org/10.1021/acsami.7b11219.

(90) Vighetto, V.; Ancona, A.; Racca, L.; Limongi, T.; Troia, A.; Canavese, G.; Cauda, V. The Synergistic Effect of Nanocrystals Combined With Ultrasound in the Generation of Reactive Oxygen Species for Biomedical Applications. *Front. Bioeng. Biotechnol.* **2019**, *7*, 374. https://doi.org/10.3389/fbioe.2019.00374.

(91) Dumontel, B.; Susa, F.; Limongi, T.; Canta, M.; Racca, L.; Chiodoni, A.; Garino, N.; Chiabotto, G.; Centomo, M. L.; Pignochino, Y.; Cauda, V. ZnO Nanocrystals Shuttled by Extracellular Vesicles as Effective Trojan Nano-

Horses against Cancer Cells. *Nanomedicine* **2019**, *14* (21), 2815–2833. https://doi.org/10.2217/nnm-2019-0231.

(92) Moon, S.-H.; Choi, W. J.; Choi, S.-W.; Kim, E. H.; Kim, J.; Lee, J.-O.; Kim, S. H. Anti-Cancer Activity of ZnO Chips by Sustained Zinc Ion Release. *Toxicology Reports* **2016**, *3*, 430–438. https://doi.org/10.1016/j.toxrep.2016.03.008.

(93) Ancona, A.; Dumontel, B.; Garino, N.; Demarco, B.; Chatzitheodoridou, D.; Fazzini, W.; Engelke, H.; Cauda, V. Lipid-Coated Zinc Oxide Nanoparticles as Innovative ROS-Generators for Photodynamic Therapy in Cancer Cells. *Nanomaterials* **2018**, *8* (3), 143. https://doi.org/10.3390/nano8030143.

(94) Racca, L.; Limongi, T.; Vighetto, V.; Dumontel, B.; Ancona, A.; Canta, M.; Canavese, G.; Garino, N.; Cauda, V. Zinc Oxide Nanocrystals and High-Energy Shock Waves: A New Synergy for the Treatment of Cancer Cells. *Front. Bioeng. Biotechnol.* **2020**, *8*. https://doi.org/10.3389/fbioe.2020.00577.

(95) Vandebriel, R. J.; Jong, W. H. D. A Review of Mammalian Toxicity of ZnO Nanoparticles. *NSA* **2012**, *5*, 61–71. https://doi.org/10.2147/NSA.S23932.

(96) Pandurangan, M.; Kim, D. H. In Vitro Toxicity of Zinc Oxide Nanoparticles: A Review. *J Nanopart Res* **2015**, *17* (3), 158. https://doi.org/10.1007/s11051-015-2958-9.

(97) Kayani, Z. N.; Bashir, H.; Riaz, S.; Naseem, S. Optical Properties and Antibacterial Activity of V Doped ZnO Used in Solar Cells and Biomedical Applications. *Materials Research Bulletin* **2019**, *115*, 121–129. https://doi.org/10.1016/j.materresbull.2019.03.016.

(98) Han, C.; Duan, L.; Zhao, X.; Hu, Z.; Niu, Y.; Geng, W. Effect of Fe Doping on Structural and Optical Properties of ZnO Films and Nanorods. *Journal of Alloys and Compounds* **2019**, *770*, 854–863. https://doi.org/10.1016/j.jallcom.2018.08.217.

(99) Laurenti, M.; Castellino, M.; Perrone, D.; Asvarov, A.; Canavese, G.; Chiolerio, A. Lead-Free Piezoelectrics: V 3+ to V 5+ Ion Conversion Promoting the Performances of V-Doped Zinc Oxide. *Scientific Reports* **2017**, *7* (1), 41957. https://doi.org/10.1038/srep41957.

(100) Laurenti, M.; Canavese, G.; Sacco, A.; Fontana, M.; Bejtka, K.; Castellino, M.; Pirri, C. F.; Cauda, V. Nanobranched ZnO Structure: P-Type Doping Induces Piezoelectric Voltage Generation and Ferroelectric–Photovoltaic Effect. *Advanced Materials* **2015**, *27* (28), 4218–4223. https://doi.org/10.1002/adma.201501594.

(101) Carofiglio, M.; Laurenti, M.; Vighetto, V.; Racca, L.; Barui, S.; Garino, N.; Gerbaldo, R.; Laviano, F.; Cauda, V. Iron-Doped ZnO Nanoparticles as

Multifunctional Nanoplatforms for Theranostics. *Nanomaterials* **2021**, *11* (10), 2628. https://doi.org/10.3390/nano11102628.

(102) Malik, R.; Tomer, V. K.; Mishra, Y. K.; Lin, L. Functional Gas Sensing Nanomaterials: A Panoramic View. *Applied Physics Reviews* **2020**, *7* (2), 021301. https://doi.org/10.1063/1.5123479.

(103) Rivera, V. F.; Auras, F.; Motto, P.; Stassi, S.; Canavese, G.; Celasco, E.; Bein, T.; Onida, B.; Cauda, V. Length-Dependent Charge Generation from Vertical Arrays of High-Aspect-Ratio ZnO Nanowires. *Chemistry – A European Journal* **2013**, *19* (43), 14665–14674. https://doi.org/10.1002/chem.201204429.

(104) Cauda, V.; Stassi, S.; Lamberti, A.; Morello, M.; Fabrizio Pirri, C.; Canavese, G. Leveraging ZnO Morphologies in Piezoelectric Composites for Mechanical Energy Harvesting. *Nano Energy* **2015**, *18*, 212–221. https://doi.org/10.1016/j.nanoen.2015.10.021.

(105) Stassi, S.; Cauda, V.; Ottone, C.; Chiodoni, A.; Pirri, C. F.; Canavese, G. Flexible Piezoelectric Energy Nanogenerator Based on ZnO Nanotubes Hosted in a Polycarbonate Membrane. *Nano Energy* **2015**, *13*, 474–481. https://doi.org/10.1016/j.nanoen.2015.03.024.

(106) Zhang, Y.; Nayak, T.; Hong, H.; Cai, W. Biomedical Applications of Zinc Oxide Nanomaterials. *CMM* **2013**, *13* (10), 1633–1645. https://doi.org/10.2174/15665240136661311111130058.

(107) Lee, H.-J.; Jeong, S.-Y.; Cho, C. R.; Park, C. H. Study of Diluted Magnetic Semiconductor: Co-Doped ZnO. *Appl. Phys. Lett.* **2002**, *81* (21), 4020–4022. https://doi.org/10.1063/1.1517405.

(108) Fukumura, T.; Jin, Z.; Ohtomo, A.; Koinuma, H.; Kawasaki, M. An Oxide-Diluted Magnetic Semiconductor: Mn-Doped ZnO. *Appl. Phys. Lett.* **1999**, *75* (21), 3366–3368. https://doi.org/10.1063/1.125353.

(109) Sato, K.; Katayama-Yoshida, H. First Principles Materials Design for Semiconductor Spintronics. *Semicond. Sci. Technol.* **2002**, *17* (4), 367. https://doi.org/10.1088/0268-1242/17/4/309.

(110) Xiao, J.; Kuc, A.; Pokhrel, S.; Schowalter, M.; Parlapalli, S.; Rosenauer, A.; Frauenheim, T.; Mädler, L.; Pettersson, L. G. M.; Heine, T. Evidence for Fe2+ in Wurtzite Coordination: Iron Doping Stabilizes ZnO Nanoparticles. *Small* **2011**, *7* (20), 2879–2886. https://doi.org/10.1002/smll.201100963.

(111) Pan, F.; Luo, J.; Yang, Y.; Wang, X.; Zeng, F. Giant Piezoresponse and Promising Application of Environmental Friendly Small-Ion-Doped ZnO. *Sci. China Technol. Sci.* **2012**, *55* (2), 421–436. https://doi.org/10.1007/s11431-011-4682-8.

(112) Samadi, M.; Zirak, M.; Naseri, A.; Khorashadizade, E.; Moshfegh, A. Z. Recent Progress on Doped ZnO Nanostructures for Visible-Light Photocatalysis. *Thin Solid Films* **2016**, *605*, 2–19. https://doi.org/10.1016/j.tsf.2015.12.064.

(113) Cerrato, E.; Gionco, C.; Berruti, I.; Sordello, F.; Calza, P.; Paganini, M. C. Rare Earth Ions Doped ZnO: Synthesis, Characterization and Preliminary Photoactivity Assessment. *Journal of Solid State Chemistry* **2018**, *264*, 42–47. https://doi.org/10.1016/j.jssc.2018.05.001.

(114) Faisal, M.; Ismail, A. A.; Ibrahim, A. A.; Bouzid, H.; Al-Sayari, S. A. Highly Efficient Photocatalyst Based on Ce Doped ZnO Nanorods: Controllable Synthesis and Enhanced Photocatalytic Activity. *Chemical Engineering Journal* **2013**, *229*, 225–233. https://doi.org/10.1016/j.cej.2013.06.004.

(115) Kumar, V.; Ntwaeaborwa, O. M.; Soga, T.; Dutta, V.; Swart, H. C. Rare Earth Doped Zinc Oxide Nanophosphor Powder: A Future Material for Solid State Lighting and Solar Cells. *ACS Photonics* **2017**, *4* (11), 2613–2637. https://doi.org/10.1021/acsphotonics.7b00777.

(116) Zhao, S.; Wang, L.; Yang, L.; Wang, Z. Synthesis and Luminescence Properties of ZnO:Tb3+ Nanotube Arrays via Electrodeposited Method. *Physica B: Condensed Matter* **2010**, *405* (15), 3200–3204. https://doi.org/10.1016/j.physb.2010.04.049.

(117) Christman, J. A.; Woolcott, R. R.; Kingon, A. I.; Nemanich, R. J. Piezoelectric Measurements with Atomic Force Microscopy. *Appl. Phys. Lett.* **1998**, *73* (26), 3851–3853. https://doi.org/10.1063/1.122914.

(118) Goel, S.; Sinha, N.; Yadav, H.; Joseph, A. J.; Kumar, B. Experimental Investigation on the Structural, Dielectric, Ferroelectric and Piezoelectric Properties of La Doped ZnO Nanoparticles and Their Application in Dye-Sensitized Solar Cells. *Physica E: Low-dimensional Systems and Nanostructures* **2017**, *91*, 72–81. https://doi.org/10.1016/j.physe.2017.04.010.

(119) Dakhel, A. A.; El-Hilo, M. Ferromagnetic Nanocrystalline Gd-Doped ZnO Powder Synthesized by Coprecipitation. *Journal of Applied Physics* **2010**, *107* (12), 123905. https://doi.org/10.1063/1.3448026.

(120) Barui, S.; Gerbaldo, R.; Garino, N.; Brescia, R.; Laviano, F.; Cauda, V. Facile Chemical Synthesis of Doped ZnO Nanocrystals Exploiting Oleic Acid. *Nanomaterials* **2020**, *10* (6), 1150. https://doi.org/10.3390/nano10061150.

(121) Murmu, P. P.; Kennedy, J.; Ruck, B. J.; Markwitz, A.; Williams, G. V. M.; Rubanov, S. Structural and Magnetic Properties of Low-Energy Gd Implanted ZnO Single Crystals. *Nuclear Instruments and Methods in Physics Research*

*Section B: Beam Interactions with Materials and Atoms* **2012**, *272*, 100–103. https://doi.org/10.1016/j.nimb.2011.01.041.

(122) Djerdj, I.; Jaglicić, Z.; Arcon, D.; Niederberger, M. Co-Doped ZnO Nanoparticles: Minireview. *Nanoscale* **2010**, *2* (7), 1096–1104. https://doi.org/10.1039/c0nr00148a.

(123) Yang, Y. C.; Song, C.; Wang, X. H.; Zeng, F.; Pan, F. Cr-Substitution-Induced Ferroelectric and Improved Piezoelectric Properties of Zn1−xCrxO Films. *Journal of Applied Physics* **2008**, *103* (7), 074107. https://doi.org/10.1063/1.2903152.

(124) Li, M.; Pokhrel, S.; Jin, X.; Mädler, L.; Damoiseaux, R.; Hoek, E. M. V. Stability, Bioavailability, and Bacterial Toxicity of ZnO and Iron-Doped ZnO Nanoparticles in Aquatic Media. *Environ. Sci. Technol.* **2011**, *45* (2), 755–761. https://doi.org/10.1021/es102266g.

(125) Yang, S.; Zhang, Y. Structural, Optical and Magnetic Properties of Mn-Doped ZnO Thin Films Prepared by Sol–Gel Method. *Journal of Magnetism and Magnetic Materials* **2013**, *334*, 52–58. https://doi.org/10.1016/j.jmmm.2013.01.026.

(126) Hassan, I. A.; Sathasivam, S.; Nair, S. P.; Carmalt, C. J. Antimicrobial Properties of Copper-Doped ZnO Coatings under Darkness and White Light Illumination. *ACS Omega* **2017**, *2* (8), 4556–4562. https://doi.org/10.1021/acsomega.7b00759.

(127) Dietl, T. A Ten-Year Perspective on Dilute Magnetic Semiconductors and Oxides. *Nature Mater* **2010**, *9* (12), 965–974. https://doi.org/10.1038/nmat2898.

(128) Omri, K.; El Ghoul, J.; Lemine, O. M.; Bououdina, M.; Zhang, B.; El Mir, L. Magnetic and Optical Properties of Manganese Doped ZnO Nanoparticles Synthesized by Sol–Gel Technique. *Superlattices and Microstructures* **2013**, *60*, 139–147. https://doi.org/10.1016/j.spmi.2013.04.029.

(129) Dabir, F.; Esfahani, H.; Bakhtiargonbadi, F.; Khodadadi, Z. Study on Microstructural and Electro-Optical Properties of Sol–Gel Derived Pure and Al/Cu-Doped ZnO Thin Films. *J Sol-Gel Sci Technol* **2020**, *96* (3), 529–538. https://doi.org/10.1007/s10971-020-05269-0.

(130) George, S.; Pokhrel, S.; Xia, T.; Gilbert, B.; Ji, Z.; Schowalter, M.; Rosenauer, A.; Damoiseaux, R.; Bradley, K. A.; Mädler, L.; Nel, A. E. Use of a Rapid Cytotoxicity Screening Approach To Engineer a Safer Zinc Oxide Nanoparticle through Iron Doping. *ACS Nano* **2010**, *4* (1), 15–29. https://doi.org/10.1021/nn901503q.

(131) Luo, J. T.; Yang, Y. C.; Zhu, X. Y.; Chen, G.; Zeng, F.; Pan, F. Enhanced Electromechanical Response of Fe-Doped ZnO Films by Modulating the Chemical State and Ionic Size of the Fe Dopant. *Phys. Rev. B* **2010**, *82* (1), 014116. https://doi.org/10.1103/PhysRevB.82.014116.

(132) Srinivasulu, T.; Saritha, K.; Reddy, K. T. R. Synthesis and Characterization of Fe-Doped ZnO Thin Films Deposited by Chemical Spray Pyrolysis. *Modern Electronic Materials* **2017**, *3* (2), 76–85. https://doi.org/10.1016/j.moem.2017.07.001.

(133) Young Ahn, G.; Park, S.-I.; Sung Kim, C. Enhanced Ferromagnetic Properties of Diluted Fe Doped ZnO with Hydrogen Treatment. *Journal of Magnetism and Magnetic Materials* **2006**, *303* (2), e329–e331. https://doi.org/10.1016/j.jmmm.2006.01.100.

(134) Kayani, Z. N.; Shah, I.; Riaz, S.; Naseem, S. Effect of Co Doping on the Physical Properties of Co-Doped ZnO Nanoparticles. *J Mater Sci: Mater Electron* **2017**, *28* (8), 5953–5961. https://doi.org/10.1007/s10854-016-6269-4.

(135) Ouarez, L.; Chelouche, A.; Touam, T.; Mahiou, R.; Djouadi, D.; Potdevin, A. Au-Doped ZnO Sol-Gel Thin Films: An Experimental Investigation on Physical and Photoluminescence Properties. *Journal of Luminescence* **2018**, *203*, 222–229. https://doi.org/10.1016/j.jlumin.2018.06.049.

(136) Pathak, T. K.; Kroon, R. E.; Swart, H. C. Photocatalytic and Biological Applications of Ag and Au Doped ZnO Nanomaterial Synthesized by Combustion. *Vacuum* **2018**, *157*, 508–513. https://doi.org/10.1016/j.vacuum.2018.09.020.

(137) Swati; Verma, R.; Chauhan, A.; Shandilya, M.; Li, X.; Kumar, R.; Kulshrestha, S. Antimicrobial Potential of Ag-Doped ZnO Nanostructure Synthesized by the Green Method Using Moringa Oleifera Extract. *Journal of Environmental Chemical Engineering* **2020**, *8* (3), 103730. https://doi.org/10.1016/j.jece.2020.103730.

(138) Namgung, G.; Ta, Q. T. H.; Yang, W.; Noh, J.-S. Diffusion-Driven Al-Doping of ZnO Nanorods and Stretchable Gas Sensors Made of Doped ZnO Nanorods/Ag Nanowires Bilayers. *ACS Appl. Mater. Interfaces* **2019**, *11* (1), 1411–1419. https://doi.org/10.1021/acsami.8b17336.

(139) Tsai, Y.-T.; Chang, S.-J.; Ji, L.-W.; Hsiao, Y.-J.; Tang, I.-T. Fast Detection and Flexible Microfluidic PH Sensors Based on Al-Doped ZnO Nanosheets with a Novel Morphology. *ACS Omega* **2019**, *4* (22), 19847–19855. https://doi.org/10.1021/acsomega.9b02778.

(140) Pradeev raj, K.; Sadaiyandi, K.; Kennedy, A.; Sagadevan, S.; Chowdhury, Z. Z.; Johan, Mohd. R. B.; Aziz, F. A.; Rafique, R. F.; Thamiz Selvi, R.; Rathina bala, R. Influence of Mg Doping on ZnO Nanoparticles for Enhanced

Photocatalytic Evaluation and Antibacterial Analysis. *Nanoscale Research Letters* **2018**, *13* (1), 229. https://doi.org/10.1186/s11671-018-2643-x.

(141) Chen, Y. J.; Brahma, S.; Liu, C. P.; Huang, J.-L. Enhancement of the Piezoelectric Coefficient in Hexagonal MgxZn1-XO Films at Lower Mg Compositions. *Journal of Alloys and Compounds* **2017**, *728*, 1248–1253. https://doi.org/10.1016/j.jallcom.2017.08.278.

(142) Gref, R.; Lück, M.; Quellec, P.; Marchand, M.; Dellacherie, E.; Harnisch, S.; Blunk, T.; Müller, R. H. 'Stealth' Corona-Core Nanoparticles Surface Modified by Polyethylene Glycol (PEG): Influences of the Corona (PEG Chain Length and Surface Density) and of the Core Composition on Phagocytic Uptake and Plasma Protein Adsorption. *Colloids and Surfaces B: Biointerfaces* **2000**, *18* (3), 301–313. https://doi.org/10.1016/S0927-7765(99)00156-3.

(143) Liu, C.; Yu, A.; Peng, M.; Song, M.; Liu, W.; Zhang, Y.; Zhai, J. Improvement in the Piezoelectric Performance of a ZnO Nanogenerator by a Combination of Chemical Doping and Interfacial Modification. *J. Phys. Chem. C* **2016**, *120* (13), 6971–6977. https://doi.org/10.1021/acs.jpcc.6b00069.

(144) Yang, Y.; Pradel, K. C.; Jing, Q.; Wu, J. M.; Zhang, F.; Zhou, Y.; Zhang, Y.; Wang, Z. L. Thermoelectric Nanogenerators Based on Single Sb-Doped ZnO Micro/Nanobelts. *ACS Nano* **2012**, *6* (8), 6984–6989. https://doi.org/10.1021/nn302481p.

(145) Podporska-Carroll, J.; Myles, A.; Quilty, B.; McCormack, D. E.; Fagan, R.; Hinder, S. J.; Dionysiou, D. D.; Pillai, S. C. Antibacterial Properties of F-Doped ZnO Visible Light Photocatalyst. *Journal of Hazardous Materials* **2017**, *324*, 39–47. https://doi.org/10.1016/j.jhazmat.2015.12.038.

(146) Martínez Julca, M. A.; Rivera, I.; Perales-Pérez, O.; Bailón, S.; Pérez, M. Li-Doped ZnO Nanoparticles as Novel Direct Generator of Singlet Oxygen for Potential Photodynamic Therapy Applications. *MRS Online Proceedings Library* **2015**, *1784* (1), 15213656501. https://doi.org/10.1557/opl.2015.625.

(147) Shi, R.; Yang, P.; Wang, J.; Zhang, A.; Zhu, Y.; Cao, Y.; Ma, Q. Growth of Flower-like ZnO via Surfactant-Free Hydrothermal Synthesis on ITO Substrate at Low Temperature. *CrystEngComm* **2012**, *14* (18), 5996–6003. https://doi.org/10.1039/C2CE25606A.

(148) Gao, T.; Wang, T. H. Synthesis and Properties of Multipod-Shaped ZnO Nanorods for Gas-Sensor Applications. *Appl. Phys. A* **2005**, *80* (7), 1451–1454. https://doi.org/10.1007/s00339-004-3075-2.

(149) Djurišić, A. B.; Leung, Y. H.; Choy, W. C. H.; Cheah, K. W.; Chan, W. K. Visible Photoluminescence in ZnO Tetrapod and Multipod Structures. *Appl. Phys. Lett.* **2004**, *84* (14), 2635–2637. https://doi.org/10.1063/1.1695633.

(150) Vayssieres, L. Growth of Arrayed Nanorods and Nanowires of ZnO from Aqueous Solutions. *Advanced Materials* **2003**, *15* (5), 464–466. https://doi.org/10.1002/adma.200390108.

(151) Jiang, C. Y.; Sun, X. W.; Lo, G. Q.; Kwong, D. L.; Wang, J. X. Improved Dye-Sensitized Solar Cells with a ZnO-Nanoflower Photoanode. *Appl. Phys. Lett.* **2007**, *90* (26), 263501. https://doi.org/10.1063/1.2751588.

(152) Yadav, H.; Sinha, N.; Goel, S.; Kumar, B. Eu-Doped ZnO Nanoparticles for Dielectric, Ferroelectric and Piezoelectric Applications. *Journal of Alloys and Compounds* **2016**, *689*, 333–341. https://doi.org/10.1016/j.jallcom.2016.07.329.

(153) Xiong, Y.; Yi, W. Y.; Yang, G. W.; Yang, Y. H. Elongated Hexagonal ZnO Micro-Fence Optical Resonator. *Current Applied Physics* **2019**, *19* (9), 984–986. https://doi.org/10.1016/j.cap.2019.05.014.

(154) Abinaya, C.; Marikkannan, M.; Manikandan, M.; Mayandi, J.; Suresh, P.; Shanmugaiah, V.; Ekstrum, C.; Pearce, J. M. Structural and Optical Characterization and Efficacy of Hydrothermal Synthesized Cu and Ag Doped Zinc Oxide Nanoplate Bactericides. *Materials Chemistry and Physics* **2016**, *184*, 172–182. https://doi.org/10.1016/j.matchemphys.2016.09.039.

(155) Gong, H.; Hu, J. Q.; Wang, J. H.; Ong, C. H.; Zhu, F. R. Nano-Crystalline Cu-Doped ZnO Thin Film Gas Sensor for CO. *Sensors and Actuators B: Chemical* **2006**, *115* (1), 247–251. https://doi.org/10.1016/j.snb.2005.09.008.

(156) Opel, M.; Nielsen, K.-W.; Bauer, S.; Goennenwein, S. T. B.; Cezar, J. C.; Schmeisser, D.; Simon, J.; Mader, W.; Gross, R. Nanosized Superparamagnetic Precipitates in Cobalt-Doped ZnO. *Eur. Phys. J. B* **2008**, *63* (4), 437. https://doi.org/10.1140/epjb/e2008-00252-4.

(157) Samanta, A.; Goswami, M. N.; Mahapatra, P. K. Fe-Doped ZnO Nanoparticles as Novel Photonic and Multiferroic Semiconductor. *Materials Chemistry and Physics* **2020**, *240*, 122180. https://doi.org/10.1016/j.matchemphys.2019.122180.

(158) Pascariu, P.; Tudose, I. V.; Suchea, M.; Koudoumas, E.; Fifere, N.; Airinei, A. Preparation and Characterization of Ni, Co Doped ZnO Nanoparticles for Photocatalytic Applications. *Applied Surface Science* **2018**, *448*, 481–488. https://doi.org/10.1016/j.apsusc.2018.04.124.

(159) Isik, M.; Gasanly, N. M. Gd-Doped ZnO Nanoparticles: Synthesis, Structural and Thermoluminescence Properties. *Journal of Luminescence* **2019**, *207*, 220–225. https://doi.org/10.1016/j.jlumin.2018.11.022.

(160) Panwar, A.; Yadav, K. L. A Novel One-Pot Synthesis of Hierarchical Europium Doped ZnO Nanoflowers. *Materials Letters* **2015**, *142*, 30–34. https://doi.org/10.1016/j.matlet.2014.11.143.

(161) Iqbal, J.; Wang, B.; Liu, X.; Yu, D.; He, B.; Yu, R. Oxygen-Vacancy-Induced Green Emission and Room-Temperature Ferromagnetism in Ni-Doped ZnO Nanorods. *New J. Phys.* **2009**, *11* (6), 063009. https://doi.org/10.1088/1367-2630/11/6/063009.

(162) Sinha, N.; Goel, S.; Joseph, A. J.; Yadav, H.; Batra, K.; Gupta, M. K.; Kumar, B. Y-Doped ZnO Nanosheets: Gigantic Piezoelectric Response for an Ultra-Sensitive Flexible Piezoelectric Nanogenerator. *Ceramics International* **2018**, *44* (7), 8582–8590. https://doi.org/10.1016/j.ceramint.2018.02.066.

(163) Goel, S.; Sinha, N.; Yadav, H.; Godara, S.; Joseph, A. J.; Kumar, B. Ferroelectric Gd-Doped ZnO Nanostructures: Enhanced Dielectric, Ferroelectric and Piezoelectric Properties. *Materials Chemistry and Physics* **2017**, *202*, 56–64. https://doi.org/10.1016/j.matchemphys.2017.08.067.

(164) Sharma, N.; Jandaik, S.; Kumar, S.; Chitkara, M.; Sandhu, I. S. Synthesis, Characterisation and Antimicrobial Activity of Manganese- and Iron-Doped Zinc Oxide Nanoparticles. *Journal of Experimental Nanoscience* **2016**, *11* (1), 54–71. https://doi.org/10.1080/17458080.2015.1025302.

(165) Liu, Y.; Ai, K.; Yuan, Q.; Lu, L. Fluorescence-Enhanced Gadolinium-Doped Zinc Oxide Quantum Dots for Magnetic Resonance and Fluorescence Imaging. *Biomaterials* **2011**, *32* (4), 1185–1192. https://doi.org/10.1016/j.biomaterials.2010.10.022.

(166) Ghaemi, B.; Mashinchian, O.; Mousavi, T.; Karimi, R.; Kharrazi, S.; Amani, A. Harnessing the Cancer Radiation Therapy by Lanthanide-Doped Zinc Oxide Based Theranostic Nanoparticles. *ACS Appl. Mater. Interfaces* **2016**, *8* (5), 3123–3134. https://doi.org/10.1021/acsami.5b10056.

(167) Sharma, N.; Kumar, J.; Thakur, S.; Sharma, S.; Shrivastava, V. Antibacterial Study of Silver Doped Zinc Oxide Nanoparticles against Staphylococcus Aureus and Bacillus Subtilis. *Drug Invention Today* **2013**, *5* (1), 50–54. https://doi.org/10.1016/j.dit.2013.03.007.

(168) Chandrasekaran, K.; Varaprasad, K.; Venugopal, S. K.; Arun, L.; Hameed, A. S. H. Synergistic Antibacterial Effect of the Magnesium-Doped ZnO Nanoparticles with Chloramphenicol. *BioNanoSci.* **2020**, *10* (1), 106–111. https://doi.org/10.1007/s12668-019-00696-y.

(169) Sun, G.; Cao, M.; Wang, Y.; Hu, C.; Liu, Y.; Ren, L.; Pu, Z. Anionic Surfactant-Assisted Hydrothermal Synthesis of High-Aspect-Ratio ZnO Nanowires and Their Photoluminescence Property. *Materials Letters* **2006**, *60* (21), 2777–2782. https://doi.org/10.1016/j.matlet.2006.01.088.

(170) Fageria, P.; Gangopadhyay, S.; Pande, S. Synthesis of ZnO/Au and ZnO/Ag Nanoparticles and Their Photocatalytic Application Using UV and Visible Light. *RSC Adv.* **2014**, *4* (48), 24962–24972. https://doi.org/10.1039/C4RA03158J.

(171) Chen, Y.; Zeng, D.; Zhang, K.; Lu, A.; Wang, L.; Peng, D.-L. Au–ZnO Hybrid Nanoflowers, Nanomultipods and Nanopyramids: One-Pot Reaction Synthesis and Photocatalytic Properties. *Nanoscale* **2013**, *6* (2), 874–881. https://doi.org/10.1039/C3NR04558G.

(172) Shannon, R. D. Revised Effective Ionic Radii and Systematic Studies of Interatomic Distances in Halides and Chalcogenides. *Acta Cryst A* **1976**, *32* (5), 751–767. https://doi.org/10.1107/S0567739476001551.

(173) Sinha, N.; Ray, G.; Bhandari, S.; Godara, S.; Kumar, B. Synthesis and Enhanced Properties of Cerium Doped ZnO Nanorods. *Ceramics International* **2014**, *40* (8, Part A), 12337–12342. https://doi.org/10.1016/j.ceramint.2014.04.079.

(174) Batra, K.; Sinha, N.; Goel, S.; Yadav, H.; Joseph, A. J.; Kumar, B. Enhanced Dielectric, Ferroelectric and Piezoelectric Performance of Nd-ZnO Nanorods and Their Application in Flexible Piezoelectric Nanogenerator. *Journal of Alloys and Compounds* **2018**, *767*, 1003–1011. https://doi.org/10.1016/j.jallcom.2018.07.187.

(175) Gazzali, P. M. M.; Rajan, S.; Chandrasekaran, G. Low-Temperature Magnetic Properties of Vanadium-Doped ZnO Nanoparticles. *J Supercond Nov Magn* **2018**, *31* (9), 2817–2828. https://doi.org/10.1007/s10948-017-4537-z.

(176) Lin, Y.; Jiang, D.; Lin, F.; Shi, W.; Ma, X. Fe-Doped ZnO Magnetic Semiconductor by Mechanical Alloying. *Journal of Alloys and Compounds* **2007**, *436* (1), 30–33. https://doi.org/10.1016/j.jallcom.2006.07.011.

(177) Chanda, A.; Gupta, S.; Vasundhara, M.; Joshi, S. R.; Mutta, G. R.; Singh, J. Study of Structural, Optical and Magnetic Properties of Cobalt Doped ZnO Nanorods. *RSC Adv.* **2017**, *7* (80), 50527–50536. https://doi.org/10.1039/C7RA08458G.

(178) Singhal, S.; Kaur, J.; Namgyal, T.; Sharma, R. Cu-Doped ZnO Nanoparticles: Synthesis, Structural and Electrical Properties. *Physica B: Condensed Matter* **2012**, *407* (8), 1223–1226. https://doi.org/10.1016/j.physb.2012.01.103.

(179) Selvaraj, S.; Mohan, M. K.; Navaneethan, M.; Ponnusamy, S.; Muthamizhchelvan, C. Synthesis and Photocatalytic Activity of Gd Doped ZnO Nanoparticles for Enhanced Degradation of Methylene Blue under Visible Light. *Materials Science in Semiconductor Processing* **2019**, *103*, 104622. https://doi.org/10.1016/j.mssp.2019.104622.

(180) Beltrán, J. J.; Barrero, C. A.; Punnoose, A. Understanding the Role of Iron in the Magnetism of Fe Doped ZnO Nanoparticles. *Phys. Chem. Chem. Phys.* **2015**, *17* (23), 15284–15296. https://doi.org/10.1039/C5CP01408E.

(181) Ashraf, R.; Riaz, S.; Kayani, Z. N.; Naseem, S. Structural and Magnetic Properties of Iron Doped ZnO Nanoparticles. *Materials Today: Proceedings* **2015**, *2* (10, Part B), 5384–5389. https://doi.org/10.1016/j.matpr.2015.11.055.

(182) Wu, X.; Wei, Z.; Zhang, L.; Wang, X.; Yang, H.; Jiang, J. Optical and Magnetic Properties of Fe Doped ZnO Nanoparticles Obtained by Hydrothermal Synthesis. *Journal of Nanomaterials* **2014**, *2014*, e792102. https://doi.org/10.1155/2014/792102.

(183) Gilbert, B.; Fakra, S. C.; Xia, T.; Pokhrel, S.; Mädler, L.; Nel, A. E. The Fate of ZnO Nanoparticles Administered to Human Bronchial Epithelial Cells. *ACS Nano* **2012**, *6* (6), 4921–4930. https://doi.org/10.1021/nn300425a.

(184) Mahmoudi Khatir, N.; Abdul-Malek, Z.; Zak, A. K.; Akbari, A.; Sabbagh, F. Sol–Gel Grown Fe-Doped ZnO Nanoparticles: Antibacterial and Structural Behaviors. *J Sol-Gel Sci Technol* **2016**, *78* (1), 91–98. https://doi.org/10.1007/s10971-015-3922-y.

(185) Moontragoon, P.; Pinitsoontorn, S.; Thongbai, P. Mn-Doped ZnO Nanoparticles: Preparation, Characterization, and Calculation of Electronic and Magnetic Properties. *Microelectronic Engineering* **2013**, *108*, 158–162. https://doi.org/10.1016/j.mee.2013.01.061.

(186) Lima, M. K.; Fernandes, D. M.; Silva, M. F.; Baesso, M. L.; Neto, A. M.; de Morais, G. R.; Nakamura, C. V.; de Oliveira Caleare, A.; Hechenleitner, A. A. W.; Pineda, E. A. G. Co-Doped ZnO Nanoparticles Synthesized by an Adapted Sol–Gel Method: Effects on the Structural, Optical, Photocatalytic and Antibacterial Properties. *J Sol-Gel Sci Technol* **2014**, *72* (2), 301–309. https://doi.org/10.1007/s10971-014-3310-z.

(187) Nair, M. G.; Nirmala, M.; Rekha, K.; Anukaliani, A. Structural, Optical, Photo Catalytic and Antibacterial Activity of ZnO and Co Doped ZnO Nanoparticles. *Materials Letters* **2011**, *65* (12), 1797–1800. https://doi.org/10.1016/j.matlet.2011.03.079.

(188) Pal, S.; Tak, Y. K.; Song, J. M. Does the Antibacterial Activity of Silver Nanoparticles Depend on the Shape of the Nanoparticle? A Study of the Gram-Negative Bacterium Escherichia Coli. *Applied and Environmental Microbiology* **2007**, *73* (6), 1712–1720. https://doi.org/10.1128/AEM.02218-06.

(189) Saxena, V.; Pandey, L. M. Synthesis, Characterization and Antibacterial Activity of Aluminum Doped Zinc Oxide. *Materials Today: Proceedings* **2019**, *18*, 1388–1400. https://doi.org/10.1016/j.matpr.2019.06.605.

(190) Li, X.; He, G.; Xiao, G.; Liu, H.; Wang, M. Synthesis and Morphology Control of ZnO Nanostructures in Microemulsions. *Journal of Colloid and Interface Science* **2009**, *333* (2), 465–473. https://doi.org/10.1016/j.jcis.2009.02.029.

(191) Wang, J.; Shi, N.; Qi, Y.; Liu, M. Reverse Micelles Template Assisted Fabrication of ZnO Hollow Nanospheres and Hexagonal Microtubes by a Novel Fast Microemulsion-Based Hydrothermal Method. *J Sol-Gel Sci Technol* **2010**, *53* (1), 101–106. https://doi.org/10.1007/s10971-009-2063-6.

(192) Ishizumi, A.; Takahashi, Y.; Yamamoto, A.; Kanemitsu, Y. Fabrication and Optical Properties of Eu3+-Doped ZnO Nanospheres and Nanorods. *Materials Science and Engineering: B* **2008**, *146* (1), 212–215. https://doi.org/10.1016/j.mseb.2007.07.030.

(193) Ishizumi, A.; Fujita, S.; Yanagi, H. Influence of Atmosphere on Photoluminescence Properties of Eu-Doped ZnO Nanocrystals. *Optical Materials* **2011**, *33* (7), 1116–1119. https://doi.org/10.1016/j.optmat.2010.09.011.

(194) Jayakumar, O. D.; Gopalakrishnan, I. K.; Kadam, R. M.; Vinu, A.; Asthana, A.; Tyagi, A. K. Magnetization and Structural Studies of Mn Doped ZnO Nanoparticles: Prepared by Reverse Micelle Method. *Journal of Crystal Growth* **2007**, *300* (2), 358–363. https://doi.org/10.1016/j.jcrysgro.2006.12.030.

(195) Saif, M.; Hafez, H.; Nabeel, A. I. Photo-Induced Self-Cleaning and Sterilizing Activity of Sm3+ Doped ZnO Nanomaterials. *Chemosphere* **2013**, *90* (2), 840–847. https://doi.org/10.1016/j.chemosphere.2012.09.095.

(196) Singh, N.; Madhav, H.; Yadav, S.; Jaiswar, G. Impact of Vanadium-, Sulfur-, and Dysprosium-Doped Zinc Oxide Nanoparticles on Various Properties of PVDF/Functionalized-PMMA Blend Nanocomposites: Structural, Optical, and Morphological Studies. *Journal of Applied Polymer Science* **2019**, *136* (9), 47116. https://doi.org/10.1002/app.47116.

(197) Mishra, A. K.; Das, D. Investigation on Fe-Doped ZnO Nanostructures Prepared by a Chemical Route. *Materials Science and Engineering: B* **2010**, *171* (1), 5–10. https://doi.org/10.1016/j.mseb.2010.03.045.

(198) Pandiyarajan, T.; Udayabhaskar, R.; Karthikeyan, B. Role of Fe Doping on Structural and Vibrational Properties of ZnO Nanostructures. *Appl. Phys. A* **2012**, *107* (2), 411–419. https://doi.org/10.1007/s00339-011-6755-8.

(199) Varma, A.; Mukasyan, A. S.; Rogachev, A. S.; Manukyan, K. V. Solution Combustion Synthesis of Nanoscale Materials. *Chem. Rev.* **2016**, *116* (23), 14493–14586. https://doi.org/10.1021/acs.chemrev.6b00279.

(200) Vahdat Vasei, H.; Masoudpanah, S. M.; Habibollahzadeh, M. Different Morphologies of ZnO via Solution Combustion Synthesis: The Role of Fuel. *Materials Research Bulletin* **2020**, *125*, 110784. https://doi.org/10.1016/j.materresbull.2020.110784.

(201) Sonali, S.; Jena, I.; Rout, S. K. A Comparative Study of Synthesis of ZnO Nano Particles: Hydrothermal and Modified Combustion Routes. *Materials Today: Proceedings* **2020**, *33*, 4966–4970. https://doi.org/10.1016/j.matpr.2020.02.826.

(202) Silambarasan, M.; Saravanan, S.; Ohtani, N.; Soga, T. Structural and Optical Studies of Pure and Ni-Doped ZnO Nanoparticles Synthesized by Simple Solution Combustion Method. *Jpn. J. Appl. Phys.* **2014**, *53* (5S1), 05FB16. https://doi.org/10.7567/JJAP.53.05FB16.

(203) Jongprateep, O.; Deedit, P.; Puranasamriddhi, R.; Meesombad, K. Synthesis of Nanoparticulate Ti-Doped ZnO by Solution Combustion Technique. *Journal of Metals, Materials and Minerals* **2018**, *28* (1).

(204) Franco, A.; Alves, T. E. P. Room Temperature Ferromagnetism in Combustion Reaction Prepared Iron-Doped Zinc Oxide Nanoparticles. *Materials Science in Semiconductor Processing* **2013**, *16* (6), 1804–1807. https://doi.org/10.1016/j.mssp.2013.07.008.

(205) Teoh, W. Y.; Amal, R.; Mädler, L. Flame Spray Pyrolysis: An Enabling Technology for Nanoparticles Design and Fabrication. *Nanoscale* **2010**, *2* (8), 1324–1347. https://doi.org/10.1039/C0NR00017E.

(206) Manshian, B. B.; Pokhrel, S.; Himmelreich, U.; Tämm, K.; Sikk, L.; Fernández, A.; Rallo, R.; Tamm, T.; Mädler, L.; Soenen, S. J. In Silico Design of Optimal Dissolution Kinetics of Fe-Doped ZnO Nanoparticles Results in Cancer-Specific Toxicity in a Preclinical Rodent Model. *Advanced Healthcare Materials* **2017**, *6* (9), 1601379. https://doi.org/10.1002/adhm.201601379.

(207) Xia, T.; Zhao, Y.; Sager, T.; George, S.; Pokhrel, S.; Li, N.; Schoenfeld, D.; Meng, H.; Lin, S.; Wang, X.; Wang, M.; Ji, Z.; Zink, J. I.; Mädler, L.; Castranova, V.; Lin, S.; Nel, A. E. Decreased Dissolution of ZnO by Iron Doping Yields Nanoparticles with Reduced Toxicity in the Rodent Lung and Zebrafish Embryos. *ACS Nano* **2011**, *5* (2), 1223–1235. https://doi.org/10.1021/nn1028482.

(208) Shuang, D.; Wang, J. B.; Zhong, X. L.; Yan, H. L. Raman Scattering and Cathodoluminescence Properties of Flower-like Manganese Doped ZnO Nanorods. *Materials Science in Semiconductor Processing* **2007**, *10* (2), 97–102. https://doi.org/10.1016/j.mssp.2007.04.002.

(209) Liu, L. Q.; Xiang, B.; Zhang, X. Z.; Zhang, Y.; Yu, D. P. Synthesis and Room Temperature Ferromagnetism of FeCo-Codoped ZnO Nanowires. *Appl. Phys. Lett.* **2006**, *88* (6), 063104. https://doi.org/10.1063/1.2168510.

(210) Bang, J. H.; Suslick, K. S. Applications of Ultrasound to the Synthesis of Nanostructured Materials. *Advanced Materials* **2010**, *22* (10), 1039–1059. https://doi.org/10.1002/adma.200904093.

(211) Karunakaran, C.; Gomathisankar, P.; Manikandan, G. Preparation and Characterization of Antimicrobial Ce-Doped ZnO Nanoparticles for Photocatalytic Detoxification of Cyanide. *Materials Chemistry and Physics* **2010**, *123* (2), 585–594. https://doi.org/10.1016/j.matchemphys.2010.05.019.

(212) Cobianu, C.; Dumbravescu, N.; Serban, B.-C.; Buiu, O.; Romanitan, C.; Comanescu, F.; Danila, M.; Marinescu, R.; Avramescu, V.; Ionescu, O. Sonochemically Synthetized ZnO-Graphene Nanohybrids and Its Characterization. *REVIEWS ON ADVANCED MATERIALS SCIENCE* **2020**, *59* (1), 176–187. https://doi.org/10.1515/rams-2020-0013.

(213) Khataee, A.; Darvishi Cheshmeh Soltani, R.; Hanifehpour, Y.; Safarpour, M.; Gholipour Ranjbar, H.; Joo, S. W. Synthesis and Characterization of Dysprosium-Doped ZnO Nanoparticles for Photocatalysis of a Textile Dye under Visible Light Irradiation. *Ind. Eng. Chem. Res.* **2014**, *53* (5), 1924–1932. https://doi.org/10.1021/ie402743u.

(214) Xiong, H.-M.; Shchukin, D. G.; Möhwald, H.; Xu, Y.; Xia, Y.-Y. Sonochemical Synthesis of Highly Luminescent Zinc Oxide Nanoparticles Doped with Magnesium(II). *Angewandte Chemie* **2009**, *121* (15), 2765–2769. https://doi.org/10.1002/ange.200805590.

(215) Khataee, A.; Karimi, A.; Arefi-Oskoui, S.; Darvishi Cheshmeh Soltani, R.; Hanifehpour, Y.; Soltani, B.; Joo, S. W. Sonochemical Synthesis of Pr-Doped ZnO Nanoparticles for Sonocatalytic Degradation of Acid Red 17. *Ultrasonics Sonochemistry* **2015**, *22*, 371–381. https://doi.org/10.1016/j.ultsonch.2014.05.023.

(216) Ivetić, T. B.; Dimitrievska, M. R.; Finčur, N. L.; Đačanin, Lj. R.; Gúth, I. O.; Abramović, B. F.; Lukić-Petrović, S. R. Effect of Annealing Temperature on Structural and Optical Properties of Mg-Doped ZnO Nanoparticles and Their Photocatalytic Efficiency in Alprazolam Degradation. *Ceramics International* **2014**, *40* (1, Part B), 1545–1552. https://doi.org/10.1016/j.ceramint.2013.07.041.

(217) Ivill, M.; Pearton, S. J.; Rawal, S.; Leu, L.; Sadik, P.; Das, R.; Hebard, A. F.; Chisholm, M.; Budai, J. D.; Norton, D. P. Structure and Magnetism of Cobalt-Doped ZnO Thin Films. *New J. Phys.* **2008**, *10* (6), 065002. https://doi.org/10.1088/1367-2630/10/6/065002.

(218) Sirelkhatim, A.; Mahmud, S.; Seeni, A.; Kaus, N. H. M.; Ann, L. C.; Bakhori, S. K. M.; Hasan, H.; Mohamad, D. Review on Zinc Oxide Nanoparticles: Antibacterial Activity and Toxicity Mechanism. *Nano-Micro Lett.* **2015**, *7* (3), 219–242. https://doi.org/10.1007/s40820-015-0040-x.

(219) Akhtar, M. J.; Ahamed, M.; Kumar, S.; Khan, M. M.; Ahmad, J.; Alrokayan, S. A. Zinc Oxide Nanoparticles Selectively Induce Apoptosis in Human Cancer Cells through Reactive Oxygen Species. *IJN* **2012**, *7*, 845–857. https://doi.org/10.2147/IJN.S29129.

(220) Rasmussen, J. W.; Martinez, E.; Louka, P.; Wingett, D. G. Zinc Oxide Nanoparticles for Selective Destruction of Tumor Cells and Potential for Drug Delivery Applications. *Expert Opinion on Drug Delivery* **2010**, *7* (9), 1063–1077. https://doi.org/10.1517/17425247.2010.502560.

(221) Li, M.; Zhu, L.; Lin, D. Toxicity of ZnO Nanoparticles to Escherichia Coli: Mechanism and the Influence of Medium Components. *Environ. Sci. Technol.* **2011**, *45* (5), 1977–1983. https://doi.org/10.1021/es102624t.

(222) Pasquet, J.; Chevalier, Y.; Couval, E.; Bouvier, D.; Noizet, G.; Morlière, C.; Bolzinger, M.-A. Antimicrobial Activity of Zinc Oxide Particles on Five Micro-Organisms of the Challenge Tests Related to Their Physicochemical Properties. *International Journal of Pharmaceutics* **2014**, *460* (1), 92–100. https://doi.org/10.1016/j.ijpharm.2013.10.031.

(223) Song, W.; Zhang, J.; Guo, J.; Zhang, J.; Ding, F.; Li, L.; Sun, Z. Role of the Dissolved Zinc Ion and Reactive Oxygen Species in Cytotoxicity of ZnO Nanoparticles. *Toxicology Letters* **2010**, *199* (3), 389–397. https://doi.org/10.1016/j.toxlet.2010.10.003.

(224) Wu, Y. L.; Fu, S.; Tok, A. I. Y.; Zeng, X. T.; Lim, C. S.; Kwek, L. C.; Boey, F. C. Y. A Dual-Colored Bio-Marker Made of Doped ZnO Nanocrystals. *Nanotechnology* **2008**, *19* (34), 345605. https://doi.org/10.1088/0957-4484/19/34/345605.

(225) Xia, T.; Kovochich, M.; Liong, M.; Mädler, L.; Gilbert, B.; Shi, H.; Yeh, J. I.; Zink, J. I.; Nel, A. E. Comparison of the Mechanism of Toxicity of Zinc Oxide and Cerium Oxide Nanoparticles Based on Dissolution and Oxidative Stress Properties. *ACS Nano* **2008**, *2* (10), 2121–2134. https://doi.org/10.1021/nn800511k.

(226) Bian, S.-W.; Mudunkotuwa, I. A.; Rupasinghe, T.; Grassian, V. H. Aggregation and Dissolution of 4 Nm ZnO Nanoparticles in Aqueous Environments: Influence of PH, Ionic Strength, Size, and Adsorption of Humic Acid. *Langmuir* **2011**, *27* (10), 6059–6068. https://doi.org/10.1021/la200570n.

(227) Pourbaix, M. *Atlas of Electrochemical Equilibria in Aqueous Solutions,*; Pergamon Press: Oxford; New York, 1966.

(228) Feng, X.; Zhang, S.; Lou, X. Controlling Silica Coating Thickness on TiO2 Nanoparticles for Effective Photodynamic Therapy. *Colloids and Surfaces B: Biointerfaces* **2013**, *107*, 220–226. https://doi.org/10.1016/j.colsurfb.2013.02.007.

(229) Tang, X.; Choo, E. S. G.; Li, L.; Ding, J.; Xue, J. Synthesis of ZnO Nanoparticles with Tunable Emission Colors and Their Cell Labeling Applications. *Chem. Mater.* **2010**, *22* (11), 3383–3388. https://doi.org/10.1021/cm903869r.

(230) Baber, O.; Jang, M.; Barber, D.; Powers, K. Amorphous Silica Coatings on Magnetic Nanoparticles Enhance Stability and Reduce Toxicity to in Vitro BEAS-2B Cells. *Inhalation Toxicology* **2011**, *23* (9), 532–543. https://doi.org/10.3109/08958378.2011.592869.

(231) Bellido, E.; Hidalgo, T.; Lozano, M. V.; Guillevic, M.; Simón-Vázquez, R.; Santander-Ortega, M. J.; González-Fernández, Á.; Serre, C.; Alonso, M. J.; Horcajada, P. Heparin-Engineered Mesoporous Iron Metal-Organic Framework Nanoparticles: Toward Stealth Drug Nanocarriers. *Advanced Healthcare Materials* **2015**, *4* (8), 1246–1257. https://doi.org/10.1002/adhm.201400755.

(232) Brigger, I.; Dubernet, C.; Couvreur, P. Nanoparticles in Cancer Therapy and Diagnosis. *Advanced Drug Delivery Reviews* **2002**, *54* (5), 631–651. https://doi.org/10.1016/S0169-409X(02)00044-3.

(233) Sawai, J.; Kawada, E.; Kanou, F.; Igarashi, H.; Hashimoto, A.; Kokugan, T.; Shimizu, M. Detection of Active Oxygen Generated from Ceramic Powders Having Antibacterial Activity. *Journal of Chemical Engineering of Japan* **1996**, *29* (4), 627–633. https://doi.org/10.1252/jcej.29.627.

(234) Kumar, Rajesh; Umar, Ahmad; Kumar, Girish; Nalwa, H. S. Antimicrobial Properties of ZnO Nanomaterials: A Review. *Ceramics International* **2017**, *43* (5), 3940–3961. https://doi.org/10.1016/j.ceramint.2016.12.062.

(235) Demirel, R.; Suvacı, E.; Şahin, İ.; Dağ, S.; Kılıç, V. Antimicrobial Activity of Designed Undoped and Doped MicNo-ZnO Particles. *Journal of Drug Delivery Science and Technology* **2018**, *47*, 309–321. https://doi.org/10.1016/j.jddst.2018.07.024.

(236) Sawai, J. Quantitative Evaluation of Antibacterial Activities of Metallic Oxide Powders (ZnO, MgO and CaO) by Conductimetric Assay. *Journal of Microbiological Methods* **2003**, *54* (2), 177–182. https://doi.org/10.1016/S0167-7012(03)00037-X.

(237) Amornpitoksuk, P.; Suwanboon, S.; Sangkanu, S.; Sukhoom, A.; Wudtipan, J.; Srijan, K.; Kaewtaro, S. Synthesis, Photocatalytic and Antibacterial Activities of ZnO Particles Modified by Diblock Copolymer. *Powder*

*Technology* **2011**, *212* (3), 432–438. https://doi.org/10.1016/j.powtec.2011.06.028.

(238) Khan, S. A.; Noreen, F.; Kanwal, S.; Iqbal, A.; Hussain, G. Green Synthesis of ZnO and Cu-Doped ZnO Nanoparticles from Leaf Extracts of Abutilon Indicum, Clerodendrum Infortunatum, Clerodendrum Inerme and Investigation of Their Biological and Photocatalytic Activities. *Materials Science and Engineering: C* **2018**, *82*, 46–59. https://doi.org/10.1016/j.msec.2017.08.071.

(239) Cele, Z.; Ndlandla, L.; Somboro, A.; Gyamfi, D.; Balogun, M. Synthesis, Characterization and Antimicrobial Activities of Quaternary Chitosan-Based Materials. *IOP Conf. Ser.: Mater. Sci. Eng.* **2018**, *430*, 012048. https://doi.org/10.1088/1757-899X/430/1/012048.

(240) Daksh, D.; Agrawal, Y. K. Comparative Study of Pure and Ni/Co, Gd3+, and Tb3+ Doped Zinc Oxide Nanoparticles for Photocatalytic Degradation and Antibacterial Activities. *Journal of Advanced Microscopy Research* **2016**, *11* (2), 113–123. https://doi.org/10.1166/jamr.2016.1300.

(241) Lin, H.; Huang, C. P.; Li, W.; Ni, C.; Shah, S. I.; Tseng, Y.-H. Size Dependency of Nanocrystalline TiO2 on Its Optical Property and Photocatalytic Reactivity Exemplified by 2-Chlorophenol. *Applied Catalysis B: Environmental* **2006**, *68* (1), 1–11. https://doi.org/10.1016/j.apcatb.2006.07.018.

(242) Röder, R.; Geburt, S.; Zapf, M.; Franke, D.; Lorke, M.; Frauenheim, T.; da Rosa, A. L.; Ronning, C. Transition Metal and Rare Earth Element Doped Zinc Oxide Nanowires for Optoelectronics. *physica status solidi (b)* **2019**, *256* (4), 1800604. https://doi.org/10.1002/pssb.201800604.

(243) He, L.; Meng, J.; Feng, J.; Yao, F.; Zhang, L.; Zhang, Z.; Liu, X.; Zhang, H. Investigation of 4f-Related Electronic Transitions of Rare-Earth Doped ZnO Luminescent Materials: Insights from First-Principles Calculations. *ChemPhysChem* **2020**, *21* (1), 51–58. https://doi.org/10.1002/cphc.201900981.

(244) Zhang, Z.-Y.; Xiong, H.-M. Photoluminescent ZnO Nanoparticles and Their Biological Applications. *Materials* **2015**, *8* (6), 3101–3127. https://doi.org/10.3390/ma8063101.

(245) Liu, H.; Zhou, P.; Zhang, L.; Liang, Z.; Zhao, H.; Wang, Z. Effects of Oxygen Partial Pressure on the Structural and Optical Properties of Undoped and Cu-Doped ZnO Thin Films Prepared by Magnetron Co-Sputtering. *Materials Letters* **2016**, *164*, 509–512. https://doi.org/10.1016/j.matlet.2015.11.038.

(246) Ning, G.; Zhao, X.; Li, J. Structure and Optical Properties of MgxZn1−xO Nanoparticles Prepared by Sol–Gel Method. *Optical Materials* **2004**, *27* (1), 1–5. https://doi.org/10.1016/j.optmat.2004.01.013.

(247) Dutta, S.; Chattopadhyay, S.; Jana, D.; Banerjee, A.; Manik, S.; Pradhan, S. K.; Sutradhar, M.; Sarkar, A. Annealing Effect on Nano-ZnO Powder Studied from Positron Lifetime and Optical Absorption Spectroscopy. *Journal of Applied Physics* **2006**, *100* (11), 114328. https://doi.org/10.1063/1.2401311.

(248) Viswanatha, R.; Sapra, S.; Sen Gupta, S.; Satpati, B.; Satyam, P. V.; Dev, B. N.; Sarma, D. D. Synthesis and Characterization of Mn-Doped ZnO Nanocrystals. *J. Phys. Chem. B* **2004**, *108* (20), 6303–6310. https://doi.org/10.1021/jp049960o.

(249) Bhuyan, T.; Khanuja, M.; Sharma, R.; Patel, S.; Reddy, M. R.; Anand, S.; Varma, A. A Comparative Study of Pure and Copper (Cu)-Doped ZnO Nanorods for Antibacterial and Photocatalytic Applications with Their Mechanism of Action. *J Nanopart Res* **2015**, *17* (7), 288. https://doi.org/10.1007/s11051-015-3093-3.

(250) Agarwal, D. C.; Singh, U. B.; Gupta, S.; Singhal, R.; Kulriya, P. K.; Singh, F.; Tripathi, A.; Singh, J.; Joshi, U. S.; Avasthi, D. K. Enhanced Room Temperature Ferromagnetism and Green Photoluminescence in Cu Doped ZnO Thin Film Synthesised by Neutral Beam Sputtering. *Sci Rep* **2019**, *9* (1), 6675. https://doi.org/10.1038/s41598-019-43184-9.

(251) Hammad, T. M.; Salem, J. K.; Harrison, R. G.; Hempelmann, R.; Hejazy, N. K. Optical and Magnetic Properties of Cu-Doped ZnO Nanoparticles. *J Mater Sci: Mater Electron* **2013**, *24* (8), 2846–2852. https://doi.org/10.1007/s10854-013-1181-7.

(252) Felipe S. Tupan, L.; Valerio-Cuadros, M. I.; Oliveira, A. A.; Barco, R.; Ivashita, F. F.; Lopes, L. F.; Passamani, E. C.; Paesano, A. Spin-Glass Transitions in Zn1-XFexO Nanoparticles. *Materials* **2020**, *13* (4), 869. https://doi.org/10.3390/ma13040869.

(253) Yılmaz, S.; Parlak, M.; Özcan, Ş.; Altunbaş, M.; McGlynn, E.; Bacaksız, E. Structural, Optical and Magnetic Properties of Cr Doped ZnO Microrods Prepared by Spray Pyrolysis Method. *Applied Surface Science* **2011**, *257* (22), 9293–9298. https://doi.org/10.1016/j.apsusc.2011.05.017.

(254) Tan, T. L.; Lai, C. W.; Abd Hamid, S. B. Tunable Band Gap Energy of Mn-Doped ZnO Nanoparticles Using the Coprecipitation Technique. *Journal of Nanomaterials* **2014**, *2014*, e371720. https://doi.org/10.1155/2014/371720.

(255) DHANALAKSHMI, A.; NATARAJAN, B.; RAMADAS, V.; PALANIMURUGAN, A.; THANIKAIKARASAN, S. Structural, Morphological, Optical and Antibacterial Activity of Rod-Shaped Zinc Oxide and Manganese-Doped Zinc Oxide Nanoparticles. *Pramana - J Phys* **2016**, *87* (4), 57. https://doi.org/10.1007/s12043-016-1248-0.

(256) El-Hilo, M.; Dakhel, A. A. Structural and Magnetic Properties of Mn-Doped ZnO Powders. *Journal of Magnetism and Magnetic Materials* **2011**, *323* (16), 2202–2205. https://doi.org/10.1016/j.jmmm.2011.03.031.

(257) Bououdina, M.; Omri, K.; El-Hilo, M.; El Amiri, A.; Lemine, O. M.; Alyamani, A.; Hlil, E. K.; Lassri, H.; El Mir, L. Structural and Magnetic Properties of Mn-Doped ZnO Nanocrystals. *Physica E: Low-dimensional Systems and Nanostructures* **2014**, *56*, 107–112. https://doi.org/10.1016/j.physe.2013.08.024.

(258) Pal, B.; Sarkar, D.; Giri, P. K. Structural, Optical, and Magnetic Properties of Ni Doped ZnO Nanoparticles: Correlation of Magnetic Moment with Defect Density. *Applied Surface Science* **2015**, *356*, 804–811. https://doi.org/10.1016/j.apsusc.2015.08.163.

(259) Tyona, M.; Osuji, R.; Lokhande, C.; Ezema, F. Photovoltaic Properties of Aluminum Doped Zinc Oxide Electrodes Based on Variation of Aluminum Impurities in the Semiconductor. *Journal of Materials Physics and Chemistry* **2018**, *6*, 9–16. https://doi.org/10.12691/jmpc-6-1-2.

(260) Gao, D.; Zhang, J.; Yang, G.; Zhang, J.; Shi, Z.; Qi, J.; Zhang, Z.; Xue, D. Ferromagnetism in ZnO Nanoparticles Induced by Doping of a Nonmagnetic Element: Al. *J. Phys. Chem. C* **2010**, *114* (32), 13477–13481. https://doi.org/10.1021/jp103458s.

(261) Maru, A.; Kamble, H.; Kalarikkal, A.; Shah, R.; Bhanuse, P.; Pradhan, N. *Mg Doped ZnO Dilute Magnetic Oxides Prepared by Chemical Method. Mg Doped ZnO Dilute Magnetic Oxides Prepared by Chemical Method*; 2015.

(262) Verma, K. C.; Goyal, N.; Kotnala, R. K. Lattice Defect-Formulated Ferromagnetism and UV Photo-Response in Pure and Nd, Sm Substituted ZnO Thin Films. *Phys. Chem. Chem. Phys.* **2019**, *21* (23), 12540–12554. https://doi.org/10.1039/C9CP02285F.

(263) Faraz, M.; Naqvi, F. K.; Shakir, M.; Khare, N. Synthesis of Samarium-Doped Zinc Oxide Nanoparticles with Improved Photocatalytic Performance and Recyclability under Visible Light Irradiation. *New J. Chem.* **2018**, *42* (3), 2295–2305. https://doi.org/10.1039/C7NJ03927A.

(264) Kumar, D. R.; Ranjith, K. S.; Nivedita, L. R.; Kumar, R. T. R. Effect of Samarium Doping on Structural, Optical and Magnetic Properties of Vertically Aligned ZnO Nanorod Arrays. *Journal of Rare Earths* **2017**, *35* (10), 1002–1007. https://doi.org/10.1016/S1002-0721(17)61005-6.

(265) Vinoditha, U.; Sarojini, B. K.; Sandeep, K. M.; Narayana, B.; Maidur, S. R.; Patil, P. S.; Balakrishna, K. M. Defects-Induced Nonlinear Saturable Absorption Mechanism in Europium-Doped ZnO Nanoparticles Synthesized

by Facile Hydrothermal Method. *Appl. Phys. A* **2019**, *125* (6), 436. https://doi.org/10.1007/s00339-019-2732-4.

(266) Yoon, H.; Hua Wu, J.; Hyun Min, J.; Sung Lee, J.; Ju, J.-S.; Keun Kim, Y. Magnetic and Optical Properties of Monosized Eu-Doped ZnO Nanocrystals from Nanoemulsion. *Journal of Applied Physics* **2012**, *111* (7), 07B523. https://doi.org/10.1063/1.3676422.

(267) Aggarwal, N.; Vasishth, A.; Kaur, K.; Verma, N. K. Investigation of Optical, Electrical and Magnetic Properties of Tb-Doped ZnO Nanorods. *J Mater Sci: Mater Electron* **2019**, *30* (5), 4807–4812. https://doi.org/10.1007/s10854-019-00774-7.

(268) Obeid, M. M.; Jappor, H. R.; Al-Marzoki, K.; Al-Hydary, I. A.; Edrees, S. J.; Shukur, M. M. Unraveling the Effect of Gd Doping on the Structural, Optical, and Magnetic Properties of ZnO Based Diluted Magnetic Semiconductor Nanorods. *RSC Adv.* **2019**, *9* (57), 33207–33221. https://doi.org/10.1039/C9RA04750F.

(269) Shally, V. Room Temperature Ferromagnetism of La Doped ZnO Nanorods. **2013**, *4* (11), 3.

(270) Young, S.-L.; Chen, H.-Z.; Kao, M.-C.; Kung, C.-Y.; Lin, C.-C.; Lin, T.-T.; Horng, L.; Shih, Y.-T.; Ou, C.-J.; Lin, C.-H. MAGNETIC PROPERTIES OF La-DOPED AND Cu-DOPED ZnO NANOWIRES FABRICATED BY HYDROTHERMAL METHOD. *Int. J. Mod. Phys. B* **2013**, *27* (15), 1362006. https://doi.org/10.1142/S0217979213620063.

(271) Fifere, N.; Airinei, A.; Timpu, D.; Rotaru, A.; Sacarescu, L.; Ursu, L. New Insights into Structural and Magnetic Properties of Ce Doped ZnO Nanoparticles. *Journal of Alloys and Compounds* **2018**, *757*, 60–69. https://doi.org/10.1016/j.jallcom.2018.05.031.

(272) Jayachandraiah, C.; Krishnaiah, G. Influence of Cerium Dopant on Magnetic and Dielectric Properties of ZnO Nanoparticles. *J Mater Sci* **2017**, *52* (12), 7058–7066. https://doi.org/10.1007/s10853-017-0938-4.

(273) Sinha, S.; Singh, M.; Preet, R.; Singh, R. ZnO Based Diluted Magnetic Semiconductors for Spintronic Device Applications: A Review. **2015**, 2278–9359.

(274) Pearton, S. J.; Norton, D. P.; Ivill, M. P.; Hebard, A. F.; Zavada, J. M.; Chen, W. M.; Buyanova, I. A. Ferromagnetism in Transition-Metal Doped ZnO. *J. Electron. Mater.* **2007**, *36* (4), 462–471. https://doi.org/10.1007/s11664-006-0034-z.

(275) Ip, K.; Frazier, R. M.; Heo, Y. W.; Norton, D. P.; Abernathy, C. R.; Pearton, S. J.; Kelly, J.; Rairigh, R.; Hebard, A. F.; Zavada, J. M.; Wilson, R. G.

Ferromagnetism in Mn- and Co-Implanted ZnO Nanorods. *Journal of Vacuum Science & Technology B: Microelectronics and Nanometer Structures Processing, Measurement, and Phenomena* **2003**, *21* (4), 1476–1481. https://doi.org/10.1116/1.1585069.

(276) Qi, J.; Yang, Y.; Zhang, L.; Chi, J.; Gao, D.; Xue, D. Room-Temperature Ferromagnetism in Er-Doped ZnO Thin Films. *Scripta Materialia* **2009**, *60* (5), 289–292. https://doi.org/10.1016/j.scriptamat.2008.10.015.

(277) Tan, C.; Xu, D.; Zhang, K.; Tian, X.; Cai, W. Electronic and Magnetic Properties of Rare-Earth Metals Doped ZnO Monolayer. *Journal of Nanomaterials* **2015**, *2015*, e329570. https://doi.org/10.1155/2015/329570.

(278) Beltrán, J. J.; Osorio, J. A.; Barrero, C. A.; Hanna, C. B.; Punnoose, A. Magnetic Properties of Fe Doped, Co Doped, and Fe+Co Co-Doped ZnO. *Journal of Applied Physics* **2013**, *113* (17), 17C308. https://doi.org/10.1063/1.4799778.

(279) Liu, H.; Cheng, X.; Liu, H.; Yang, J.; Liu, Y.; Liu, X.; Gao, M.; Wei, M.; Zhang, X.; Jiang, Y. Structural, Optical and Magnetic Properties of Cu and V Co-Doped ZnO Nanoparticles. *Physica E: Low-dimensional Systems and Nanostructures* **2013**, *47*, 1–5. https://doi.org/10.1016/j.physe.2012.09.019.

(280) Xu, M.; Yuan, H.; You, B.; Zhou, P. F.; Dong, C. J.; Duan, M. Y. Structural, Optical, and Magnetic Properties of (Co, Cu)-Codoped ZnO Films with Different Co Concentrations. *Journal of Applied Physics* **2014**, *115* (9), 093503. https://doi.org/10.1063/1.4867399.

(281) Xiao, Y.-D.; Paudel, R.; Liu, J.; Ma, C.; Zhang, Z.-S.; Zhou, S.-K. MRI Contrast Agents: Classification and Application (Review). *International Journal of Molecular Medicine* **2016**, *38* (5), 1319–1326. https://doi.org/10.3892/ijmm.2016.2744.

(282) Nguyen, H.; Tinet, E.; Chauveau, T.; Geinguenaud, F.; Lalatonne, Y.; Michel, A.; Aid-Launais, R.; Journé, C.; Lefèbvre, C.; Simon-Yarza, T.; Motte, L.; Jouini, N.; Tualle, J.-M.; Chaubet, F. Bimodal Fucoidan-Coated Zinc Oxide/Iron Oxide-Based Nanoparticles for the Imaging of Atherothrombosis. *Molecules* **2019**, *24* (5), 962. https://doi.org/10.3390/molecules24050962.

(283) Yin, Q.; Jin, X.; Yang, G.; Jiang, C.; Song, Z.; Sun, G. Biocompatible Folate-Modified Gd3+/Yb3+-Doped ZnO Nanoparticles for Dualmodal MRI/CT Imaging. *RSC Adv.* **2014**, *4* (96), 53561–53569. https://doi.org/10.1039/C4RA08100E.

(284) Chiavacci, L. A.; da Silva, B. L.; Manaia, E. B.; Lepeltier, E.; Benoit, J.-P.; Lemaire, L. ZnO Based Quantum Dots for Magnetic Resonance and Fluorescence Imaging; 2019. https://doi.org/10.11159/icnnfc19.107.

(285) Hanley, C.; Layne, J.; Punnoose, A.; Reddy, K. M.; Coombs, I.; Coombs, A.; Feris, K.; Wingett, D. Preferential Killing of Cancer Cells and Activated Human T Cells Using ZnO Nanoparticles. *Nanotechnology* **2008**, *19* (29), 295103. https://doi.org/10.1088/0957-4484/19/29/295103.

(286) Castano, A. P.; Demidova, T. N.; Hamblin, M. R. Mechanisms in Photodynamic Therapy: Part One—Photosensitizers, Photochemistry and Cellular Localization. *Photodiagnosis and Photodynamic Therapy* **2004**, *1* (4), 279–293. https://doi.org/10.1016/S1572-1000(05)00007-4.

(287) Hackenberg, S.; Scherzed, A.; Kessler, M.; Froelich, K.; Ginzkey, C.; Koehler, C.; Burghartz, M.; Hagen, R.; Kleinsasser, N. Zinc Oxide Nanoparticles Induce Photocatalytic Cell Death in Human Head and Neck Squamous Cell Carcinoma Cell Lines in Vitro. *International Journal of Oncology* **2010**, *37* (6), 1583–1590. https://doi.org/10.3892/ijo_00000812.

(288) Zangeneh, M.; Nedaei, H. A.; Mozdarani, H.; Mahmoudzadeh, A.; Salimi, M. Enhanced Cytotoxic and Genotoxic Effects of Gadolinium-Doped ZnO Nanoparticles on Irradiated Lung Cancer Cells at Megavoltage Radiation Energies. *Materials Science and Engineering: C* **2019**, *103*, 109739. https://doi.org/10.1016/j.msec.2019.109739.

(289) Chen, G.; Qiu, H.; Prasad, P. N.; Chen, X. Upconversion Nanoparticles: Design, Nanochemistry, and Applications in Theranostics. *Chem. Rev.* **2014**, *114* (10), 5161–5214. https://doi.org/10.1021/cr400425h.

(290) Kelkar, S. S.; Reineke, T. M. Theranostics: Combining Imaging and Therapy. *Bioconjugate Chem.* **2011**, *22* (10), 1879–1903. https://doi.org/10.1021/bc200151q.

(291) Slowing, I. I.; Vivero-Escoto, J. L.; Wu, C.-W.; Lin, V. S.-Y. Mesoporous Silica Nanoparticles as Controlled Release Drug Delivery and Gene Transfection Carriers. *Advanced Drug Delivery Reviews* **2008**, *60* (11), 1278–1288. https://doi.org/10.1016/j.addr.2008.03.012.

(292) Gupta, A. K.; Gupta, M. Synthesis and Surface Engineering of Iron Oxide Nanoparticles for Biomedical Applications. *Biomaterials* **2005**, *26* (18), 3995–4021. https://doi.org/10.1016/j.biomaterials.2004.10.012.

(293) Canavese, G.; Ancona, A.; Racca, L.; Canta, M.; Dumontel, B.; Barbaresco, F.; Limongi, T.; Cauda, V. Nanoparticle-Assisted Ultrasound: A Special Focus on Sonodynamic Therapy against Cancer. *Chemical Engineering Journal* **2018**, *340*, 155–172. https://doi.org/10.1016/j.cej.2018.01.060.

(294) Brazzale, C.; Canaparo, R.; Racca, L.; Foglietta, F.; Durando, G.; Fantozzi, R.; Caliceti, P.; Salmaso, S.; Serpe, L. Enhanced Selective Sonosensitizing Efficacy of Ultrasound-Based Anticancer Treatment by Targeted Gold

Nanoparticles. *Nanomedicine* **2016**, *11* (23), 3053–3070. https://doi.org/10.2217/nnm-2016-0293.

(295) Noman, M. T.; Amor, N.; Petru, M. Synthesis and Applications of ZnO Nanostructures (ZONSs): A Review. *Critical Reviews in Solid State and Materials Sciences* **2021**, *0* (0), 1–43. https://doi.org/10.1080/10408436.2021.1886041.

(296) Wojnarowicz, J.; Chudoba, T.; Lojkowski, W. A Review of Microwave Synthesis of Zinc Oxide Nanomaterials: Reactants, Process Parameters and Morphologies. *Nanomaterials* **2020**, *10* (6), 1086. https://doi.org/10.3390/nano10061086.

(297) Bandeira, M.; Giovanela, M.; Roesch-Ely, M.; Devine, D. M.; da Silva Crespo, J. Green Synthesis of Zinc Oxide Nanoparticles: A Review of the Synthesis Methodology and Mechanism of Formation. *Sustainable Chemistry and Pharmacy* **2020**, *15*, 100223. https://doi.org/10.1016/j.scp.2020.100223.

(298) Marino, A.; Arai, S.; Hou, Y.; Sinibaldi, E.; Pellegrino, M.; Chang, Y.-T.; Mazzolai, B.; Mattoli, V.; Suzuki, M.; Ciofani, G. Piezoelectric Nanoparticle-Assisted Wireless Neuronal Stimulation. *ACS Nano* **2015**, *9* (7), 7678–7689. https://doi.org/10.1021/acsnano.5b03162.

(299) Genchi, G. G.; Ceseracciu, L.; Marino, A.; Labardi, M.; Marras, S.; Pignatelli, F.; Bruschini, L.; Mattoli, V.; Ciofani, G. P(VDF-TrFE)/BaTiO3 Nanoparticle Composite Films Mediate Piezoelectric Stimulation and Promote Differentiation of SH-SY5Y Neuroblastoma Cells. *Advanced Healthcare Materials* **2016**, *5* (14), 1808–1820. https://doi.org/10.1002/adhm.201600245.

(300) Marino, A.; Almici, E.; Migliorin, S.; Tapeinos, C.; Battaglini, M.; Cappello, V.; Marchetti, M.; de Vito, G.; Cicchi, R.; Pavone, F. S.; Ciofani, G. Piezoelectric Barium Titanate Nanostimulators for the Treatment of Glioblastoma Multiforme. *Journal of Colloid and Interface Science* **2019**, *538*, 449–461. https://doi.org/10.1016/j.jcis.2018.12.014.

(301) Yoon, J.-K.; Misra, M.; Yu, S. J.; Kim, H. Y.; Bhang, S. H.; Song, S. Y.; Lee, J.-R.; Ryu, S.; Choo, Y. W.; Jeong, G.-J.; Kwon, S. P.; Im, S. G.; Lee, T. I.; Kim, B.-S. Thermosensitive, Stretchable, and Piezoelectric Substrate for Generation of Myogenic Cell Sheet Fragments from Human Mesenchymal Stem Cells for Skeletal Muscle Regeneration. *Advanced Functional Materials* **2017**, *27* (48), 1703853. https://doi.org/10.1002/adfm.201703853.

(302) Patterson, A. L. The Scherrer Formula for X-Ray Particle Size Determination. *Phys. Rev.* **1939**, *56* (10), 978–982. https://doi.org/10.1103/PhysRev.56.978.

(303) Socrates, G. *Infrared and Raman Characteristic Group Frequencies: Tables and Charts*, 3. ed., repr. as paperback.; Wiley: Chichester, 2010.

(304) Biesinger, M. C. Resolving Surface Chemical States in XPS Analysis of First Row Transition Metals, Oxides and Hydroxides: Cr, Mn, Fe, Co and Ni. *Applied Surface Science* **2011**, 14.

(305) Wang, L. M.; Liao, J.-W.; Peng, Z.-A.; Lai, J.-H. Doping Effects on the Characteristics of Fe:ZnO Films: Valence Transition and Hopping Transport. *J. Electrochem. Soc.* **2008**, *156* (2), H138. https://doi.org/10.1149/1.3035825.

(306) Kumar, S.; Kim, Y. J.; Koo, B. H.; Sharma, S. K.; Vargas, J. M.; Knobel, M.; Gautam, S.; Chae, K. H.; Kim, D. K.; Kim, Y. K.; Lee, C. G. Structural and Magnetic Properties of Chemically Synthesized Fe Doped ZnO. *Journal of Applied Physics* **2009**, *105* (7), 07C520. https://doi.org/10.1063/1.3073933.

(307) Zhang, H.; Chen, B.; Jiang, H.; Wang, C.; Wang, H.; Wang, X. A Strategy for ZnO Nanorod Mediated Multi-Mode Cancer Treatment. *Biomaterials* **2011**, *32* (7), 1906–1914. https://doi.org/10.1016/j.biomaterials.2010.11.027.

(308) Li, J.; Guo, D.; Wang, X.; Wang, H.; Jiang, H.; Chen, B. The Photodynamic Effect of Different Size ZnO Nanoparticles on Cancer Cell Proliferation In Vitro. *Nanoscale Res Lett* **2010**, *5* (6), 1063–1071. https://doi.org/10.1007/s11671-010-9603-4.

(309) Adams, L. K.; Lyon, D. Y.; Alvarez, P. J. J. Comparative Eco-Toxicity of Nanoscale TiO2, SiO2, and ZnO Water Suspensions. *Water Research* **2006**, *40* (19), 3527–3532. https://doi.org/10.1016/j.watres.2006.08.004.

(310) Gamage, J.; Zhang, Z. Applications of Photocatalytic Disinfection. *International Journal of Photoenergy* **2010**, *2010*, e764870. https://doi.org/10.1155/2010/764870.

(311) Murphy, A. B. Band-Gap Determination from Diffuse Reflectance Measurements of Semiconductor Films, and Application to Photoelectrochemical Water-Splitting. *Solar Energy Materials and Solar Cells* **2007**, *91* (14), 1326–1337. https://doi.org/10.1016/j.solmat.2007.05.005.

(312) Gaur, L. K.; Gairola, P.; Gairola, S. P.; Mathpal, M. C.; Kumar, P.; Kumar, S.; Kushavah, D.; Agrahari, V.; Aragon, F. F. H.; Soler, M. A. G.; Swart, H. C. Cobalt Doping Induced Shape Transformation and Its Effect on Luminescence in Zinc Oxide Rod-like Nanostructures. *Journal of Alloys and Compounds* **2021**, *868*, 159189. https://doi.org/10.1016/j.jallcom.2021.159189.

(313) Fan, H. J.; Scholz, R.; Kolb, F. M.; Zacharias, M.; Gösele, U.; Heyroth, F.; Eisenschmidt, C.; Hempel, T.; Christen, J. On the Growth Mechanism and Optical Properties of ZnO Multi-Layer Nanosheets. *Appl. Phys. A* **2004**, *79* (8), 1895–1900. https://doi.org/10.1007/s00339-004-2933-2.

(314) Liu, X.; Wu, X.; Cao, H.; Chang, R. P. H. Growth Mechanism and Properties of ZnO Nanorods Synthesized by Plasma-Enhanced Chemical Vapor

Deposition. *Journal of Applied Physics* **2004**, *95* (6), 3141–3147. https://doi.org/10.1063/1.1646440.

(315) Djurišić, A. B.; Leung, Y. H. Optical Properties of ZnO Nanostructures. *Small* **2006**, *2* (8–9), 944–961. https://doi.org/10.1002/smll.200600134.

(316) Liu, C.; Yun, F.; Morkoc, H. Ferromagnetism of ZnO and GaN: A Review. 43.

(317) Garcia, M. A.; Merino, J. M.; Fernández Pinel, E.; Quesada, A.; de la Venta, J.; Ruíz González, M. L.; Castro, G. R.; Crespo, P.; Llopis, J.; González-Calbet, J. M.; Hernando, A. Magnetic Properties of ZnO Nanoparticles. *Nano Lett.* **2007**, *7* (6), 1489–1494. https://doi.org/10.1021/nl070198m.

(318) Wang, D.; Chen, Z. Q.; Wang, D. D.; Gong, J.; Cao, C. Y.; Tang, Z.; Huang, L. R. Effect of Thermal Annealing on the Structure and Magnetism of Fe-Doped ZnO Nanocrystals Synthesized by Solid State Reaction. *Journal of Magnetism and Magnetic Materials* **2010**, *322* (22), 3642–3647. https://doi.org/10.1016/j.jmmm.2010.07.014.

(319) Chen, Z. C.; Zhuge, L. J.; Wu, X. M.; Meng, Y. D. Initial Study on the Structure and Optical Properties of Zn1−xFexO Films. *Thin Solid Films* **2007**, *515* (13), 5462–5465. https://doi.org/10.1016/j.tsf.2007.01.015.

(320) Wang, C.; Chen, Z.; He, Y.; Li, L.; Zhang, D. Structure, Morphology and Properties of Fe-Doped ZnO Films Prepared by Facing-Target Magnetron Sputtering System. *Applied Surface Science* **2009**, *255* (15), 6881–6887. https://doi.org/10.1016/j.apsusc.2009.03.008.

(321) Kumar, K.; Chitkara, M.; Sandhu, I. S.; Mehta, D.; Kumar, S. Photocatalytic, Optical and Magnetic Properties of Fe-Doped ZnO Nanoparticles Prepared by Chemical Route. *Journal of Alloys and Compounds* **2014**, *588*, 681–689. https://doi.org/10.1016/j.jallcom.2013.11.127.

(322) Chattopadhyay, A.; Das Sarma, S.; Millis, A. J. Transition Temperature of Ferromagnetic Semiconductors: A Dynamical Mean Field Study. *Phys. Rev. Lett.* **2001**, *87* (22), 227202. https://doi.org/10.1103/PhysRevLett.87.227202.

(323) Li, Y. W.; Zhou, X. L.; Miao, H. C.; Cai, H. R.; Li, F. X. Mechanism of Crystal-Symmetry Dependent Deformation in Ferroelectric Ceramics: Experiments versus Model. *Journal of Applied Physics* **2013**, *113* (21), 214111. https://doi.org/10.1063/1.4809979.

(324) Acosta, M.; Novak, N.; Rojas, V.; Patel, S.; Vaish, R.; Koruza, J.; Rossetti, G. A.; Rödel, J. BaTiO3-Based Piezoelectrics: Fundamentals, Current Status, and Perspectives. *Applied Physics Reviews* **2017**, *4* (4), 041305. https://doi.org/10.1063/1.4990046.

(325) Laurenti, M.; Verna, A.; Chiolerio, A. Evidence of Negative Capacitance in Piezoelectric ZnO Thin Films Sputtered on Interdigital Electrodes. *ACS Appl. Mater. Interfaces* **2015**, *7* (44), 24470–24479. https://doi.org/10.1021/acsami.5b05336.

(326) Carofiglio, M.; Conte, M.; Racca, L.; Cauda, V. Synergistic Phenomena between Iron-Doped ZnO Nanoparticles and Shock Waves Exploited against Pancreatic Cancer Cells. *ACS Appl. Nano Mater.* **2022**. https://doi.org/10.1021/acsanm.2c04211.

(327) Lammers, T.; Aime, S.; Hennink, W. E.; Storm, G.; Kiessling, F. Theranostic Nanomedicine. *Acc. Chem. Res.* **2011**, *44* (10), 1029–1038. https://doi.org/10.1021/ar200019c.

(328) Jokerst, J. V.; Gambhir, S. S. Molecular Imaging with Theranostic Nanoparticles. *Acc. Chem. Res.* **2011**, *44* (10), 1050–1060. https://doi.org/10.1021/ar200106e.

(329) Li, Z.; Barnes, J. C.; Bosoy, A.; Stoddart, J. F.; Zink, J. I. Mesoporous Silica Nanoparticles in Biomedical Applications. *Chem. Soc. Rev.* **2012**, *41* (7), 2590–2605. https://doi.org/10.1039/C1CS15246G.

(330) Yang, K.; Feng, L.; Shi, X.; Liu, Z. Nano-Graphene in Biomedicine: Theranostic Applications. *Chem. Soc. Rev.* **2012**, *42* (2), 530–547. https://doi.org/10.1039/C2CS35342C.

(331) Liu, Y.; Bhattarai, P.; Dai, Z.; Chen, X. Photothermal Therapy and Photoacoustic Imaging via Nanotheranostics in Fighting Cancer. *Chem. Soc. Rev.* **2019**, *48* (7), 2053–2108. https://doi.org/10.1039/C8CS00618K.

(332) Lammers, T.; Subr, V.; Ulbrich, K.; Peschke, P.; Huber, P. E.; Hennink, W. E.; Storm, G. Simultaneous Delivery of Doxorubicin and Gemcitabine to Tumors in Vivo Using Prototypic Polymeric Drug Carriers. *Biomaterials* **2009**, *30* (20), 3466–3475. https://doi.org/10.1016/j.biomaterials.2009.02.040.

(333) Tyler, B.; Gullotti, D.; Mangraviti, A.; Utsuki, T.; Brem, H. Polylactic Acid (PLA) Controlled Delivery Carriers for Biomedical Applications. *Advanced Drug Delivery Reviews* **2016**, *107*, 163–175. https://doi.org/10.1016/j.addr.2016.06.018.

(334) Banik, B. L.; Fattahi, P.; Brown, J. L. Polymeric Nanoparticles: The Future of Nanomedicine. *WIREs Nanomedicine and Nanobiotechnology* **2016**, *8* (2), 271–299. https://doi.org/10.1002/wnan.1364.

(335) Srikar, R.; Upendran, A.; Kannan, R. Polymeric Nanoparticles for Molecular Imaging. *WIREs Nanomedicine and Nanobiotechnology* **2014**, *6* (3), 245–267. https://doi.org/10.1002/wnan.1259.

(336) Al-Jamal, W. T.; Kostarelos, K. Liposomes: From a Clinically Established Drug Delivery System to a Nanoparticle Platform for Theranostic Nanomedicine. *Acc. Chem. Res.* **2011**, *44* (10), 1094–1104. https://doi.org/10.1021/ar200105p.

(337) Muthu, M. S.; Kulkarni, S. A.; Raju, A.; Feng, S.-S. Theranostic Liposomes of TPGS Coating for Targeted Co-Delivery of Docetaxel and Quantum Dots. *Biomaterials* **2012**, *33* (12), 3494–3501. https://doi.org/10.1016/j.biomaterials.2012.01.036.

(338) Wen, C.-J.; Sung, C. T.; Aljuffali, I. A.; Huang, Y.-J.; Fang, J.-Y. Nanocomposite Liposomes Containing Quantum Dots and Anticancer Drugs for Bioimaging and Therapeutic Delivery: A Comparison of Cationic, PEGylated and Deformable Liposomes. *Nanotechnology* **2013**, *24* (32), 325101. https://doi.org/10.1088/0957-4484/24/32/325101.

(339) Lee, J. E.; Lee, N.; Kim, T.; Kim, J.; Hyeon, T. Multifunctional Mesoporous Silica Nanocomposite Nanoparticles for Theranostic Applications. *Acc. Chem. Res.* **2011**, *44* (10), 893–902. https://doi.org/10.1021/ar2000259.

(340) Cauda, V.; Xu, T. T.; Nunes, I.; Mereu, E.; Villata, S.; Bergaggio, E.; Labrador, M.; Limongi, T.; Susa, F.; Chiodoni, A.; Cumerlato, M.; Rosso, G.; Stefania, R.; Piva, R. Biomimetic Mesoporous Vectors Enabling the Efficient Inhibition of Wild-Type Isocitrate Dehydrogenase in Multiple Myeloma Cells. *Microporous and Mesoporous Materials* **2021**, *325*, 111320. https://doi.org/10.1016/j.micromeso.2021.111320.

(341) Qiu, Y.; Park, K. Environment-Sensitive Hydrogels for Drug Delivery. *Advanced Drug Delivery Reviews* **2001**, *53* (3), 321–339. https://doi.org/10.1016/S0169-409X(01)00203-4.

(342) Schmaljohann, D. Thermo- and PH-Responsive Polymers in Drug Delivery. *Advanced Drug Delivery Reviews* **2006**, *58* (15), 1655–1670. https://doi.org/10.1016/j.addr.2006.09.020.

(343) Kohler, N.; Sun, C.; Fichtenholtz, A.; Gunn, J.; Fang, C.; Zhang, M. Methotrexate-Immobilized Poly(Ethylene Glycol) Magnetic Nanoparticles for MR Imaging and Drug Delivery. *Small* **2006**, *2* (6), 785–792. https://doi.org/10.1002/smll.200600009.

(344) Jain, T. K.; Richey, J.; Strand, M.; Leslie-Pelecky, D. L.; Flask, C. A.; Labhasetwar, V. Magnetic Nanoparticles with Dual Functional Properties: Drug Delivery and Magnetic Resonance Imaging. *Biomaterials* **2008**, *29* (29), 4012–4021. https://doi.org/10.1016/j.biomaterials.2008.07.004.

(345) Pankhurst, Q. A.; Connolly, J.; Jones, S. K.; Dobson, J. Applications of Magnetic Nanoparticles in Biomedicine. *J. Phys. D: Appl. Phys.* **2003**, *36* (13), R167–R181. https://doi.org/10.1088/0022-3727/36/13/201.

(346) Jordan, A.; Scholz, R.; Wust, P.; Fähling, H.; Roland Felix. Magnetic Fluid Hyperthermia (MFH): Cancer Treatment with AC Magnetic Field Induced Excitation of Biocompatible Superparamagnetic Nanoparticles. *Journal of Magnetism and Magnetic Materials* **1999**, *201* (1), 413–419. https://doi.org/10.1016/S0304-8853(99)00088-8.

(347) Huang, X.; El-Sayed, I. H.; Qian, W.; El-Sayed, M. A. Cancer Cell Imaging and Photothermal Therapy in the Near-Infrared Region by Using Gold Nanorods. *J. Am. Chem. Soc.* **2006**, *128* (6), 2115–2120. https://doi.org/10.1021/ja057254a.

(348) Liu, Y.; Ai, K.; Liu, J.; Deng, M.; He, Y.; Lu, L. Dopamine-Melanin Colloidal Nanospheres: An Efficient Near-Infrared Photothermal Therapeutic Agent for In Vivo Cancer Therapy. *Advanced Materials* **2013**, *25* (9), 1353–1359. https://doi.org/10.1002/adma.201204683.

(349) Robinson, J. T.; Tabakman, S. M.; Liang, Y.; Wang, H.; Sanchez Casalongue, H.; Vinh, D.; Dai, H. Ultrasmall Reduced Graphene Oxide with High Near-Infrared Absorbance for Photothermal Therapy. *J. Am. Chem. Soc.* **2011**, *133* (17), 6825–6831. https://doi.org/10.1021/ja2010175.

(350) Lucky, S. S.; Soo, K. C.; Zhang, Y. Nanoparticles in Photodynamic Therapy. *Chem. Rev.* **2015**, *115* (4), 1990–2042. https://doi.org/10.1021/cr5004198.

(351) Chen, Y.-H.; Tsai, C.-Y.; Huang, P.-Y.; Chang, M.-Y.; Cheng, P.-C.; Chou, C.-H.; Chen, D.-H.; Wang, C.-R.; Shiau, A.-L.; Wu, C.-L. Methotrexate Conjugated to Gold Nanoparticles Inhibits Tumor Growth in a Syngeneic Lung Tumor Model. *Mol. Pharmaceutics* **2007**, *4* (5), 713–722. https://doi.org/10.1021/mp060132k.

(352) Bhumkar, D. R.; Joshi, H. M.; Sastry, M.; Pokharkar, V. B. Chitosan Reduced Gold Nanoparticles as Novel Carriers for Transmucosal Delivery of Insulin. *Pharm Res* **2007**, *24* (8), 1415–1426. https://doi.org/10.1007/s11095-007-9257-9.

(353) Cheng, Y.; Samia, A. C.; Meyers, J. D.; Panagopoulos, I.; Fei, B.; Burda, C. Highly Efficient Drug Delivery with Gold Nanoparticle Vectors for in Vivo Photodynamic Therapy of Cancer. *J. Am. Chem. Soc.* **2008**, *130* (32), 10643–10647. https://doi.org/10.1021/ja801631c.

(354) Huang, X.; Jain, P. K.; El-Sayed, I. H.; El-Sayed, M. A. Plasmonic Photothermal Therapy (PPTT) Using Gold Nanoparticles. *Lasers Med Sci* **2007**, *23* (3), 217. https://doi.org/10.1007/s10103-007-0470-x.

(355) Oleinick, N. L.; Morris, R. L.; Belichenko, I. The Role of Apoptosis in Response to Photodynamic Therapy: What, Where, Why, and How.

*Photochem. Photobiol. Sci.* **2002**, *1* (1), 1–21. https://doi.org/10.1039/B108586G.

(356) Racca, L.; Cauda, V. Remotely Activated Nanoparticles for Anticancer Therapy. *Nano-Micro Lett.* **2020**, *13* (1), 11. https://doi.org/10.1007/s40820-020-00537-8.

(357) McKenzie, R. L.; Liley, J. B.; Björn, L. O. UV Radiation: Balancing Risks and Benefits†. *Photochemistry and Photobiology* **2009**, *85* (1), 88–98. https://doi.org/10.1111/j.1751-1097.2008.00400.x.

(358) Ivkov, R.; DeNardo, S. J.; Daum, W.; Foreman, A. R.; Goldstein, R. C.; Nemkov, V. S.; DeNardo, G. L. Application of High Amplitude Alternating Magnetic Fields for Heat Induction of Nanoparticles Localized in Cancer. *Clinical Cancer Research* **2005**, *11* (19), 7093s–7103s. https://doi.org/10.1158/1078-0432.CCR-1004-0016.

(359) Sarantis, P.; Koustas, E.; Papadimitropoulou, A.; Papavassiliou, A. G.; Karamouzis, M. V. Pancreatic Ductal Adenocarcinoma: Treatment Hurdles, Tumor Microenvironment and Immunotherapy. *World J Gastrointest Oncol* **2020**, *12* (2), 173–181. https://doi.org/10.4251/wjgo.v12.i2.173.

(360) Zeng, S.; Pöttler, M.; Lan, B.; Grützmann, R.; Pilarsky, C.; Yang, H. Chemoresistance in Pancreatic Cancer. *International Journal of Molecular Sciences* **2019**, *20* (18), 4504. https://doi.org/10.3390/ijms20184504.

(361) Conte, M.; Cauda, V. Multimodal Therapies against Pancreatic Ductal Adenocarcinoma: A Review on Synergistic Approaches towards Ultimate Nanomedicine Treatments. *Advanced Therapeutics* **2022**. https://doi.org/10.1002/adtp.202200079.

(362) Wan, G.-Y.; Liu, Y.; Chen, B.-W.; Liu, Y.-Y.; Wang, Y.-S.; Zhang, N. Recent Advances of Sonodynamic Therapy in Cancer Treatment. *Cancer Biol Med* **2016**, *13* (3), 325–338. https://doi.org/10.20892/j.issn.2095-3941.2016.0068.

(363) Rosenthal, I.; Sostaric, J. Z.; Riesz, P. Sonodynamic Therapy—a Review of the Synergistic Effects of Drugs and Ultrasound. *Ultrasonics Sonochemistry* **2004**, *11* (6), 349–363. https://doi.org/10.1016/j.ultsonch.2004.03.004.

(364) Sazgarnia, A.; Shanei, A.; Meibodi, N. T.; Eshghi, H.; Nassirli, H. A Novel Nanosonosensitizer for Sonodynamic Therapy. *Journal of Ultrasound in Medicine* **2011**, *30* (10), 1321–1329. https://doi.org/10.7863/jum.2011.30.10.1321.

(365) Brazzale, C.; Canaparo, R.; Racca, L.; Foglietta, F.; Durando, G.; Fantozzi, R.; Caliceti, P.; Salmaso, S.; Serpe, L. Enhanced Selective Sonosensitizing Efficacy of Ultrasound-Based Anticancer Treatment by Targeted Gold

Nanoparticles. *Nanomedicine* **2016**, *11* (23), 3053–3070. https://doi.org/10.2217/nnm-2016-0293.

(366) Vighetto, V.; Racca, L.; Canta, M.; Matos, J. C.; Dumontel, B.; Gonçalves, M. C.; Cauda, V. Smart Shockwave Responsive Titania-Based Nanoparticles for Cancer Treatment. *Pharmaceutics* **2021**, *13* (9), 1423. https://doi.org/10.3390/pharmaceutics13091423.

(367) Matos, J. C.; Laurenti, M.; Vighetto, V.; Pereira, L. C. J.; Waerenborgh, J. C.; Gonçalves, M. C.; Cauda, V. Biomimetic Amorphous Titania Nanoparticles as Ultrasound Responding Agents to Improve Cavitation and ROS Production for Sonodynamic Therapy. *Applied Sciences* **2020**, *10* (23), 8479. https://doi.org/10.3390/app10238479.

(368) Dumontel, B.; Susa, F.; Limongi, T.; Vighetto, V.; Debellis, D.; Canta, M.; Cauda, V. Nanotechnological Engineering of Extracellular Vesicles for the Development of Actively Targeted Hybrid Nanodevices. *Cell & Bioscience* **2022**, *12* (1), 61. https://doi.org/10.1186/s13578-022-00784-9.

(369) Li, D.; Yang, Y.; Li, D.; Pan, J.; Chu, C.; Liu, G. Organic Sonosensitizers for Sonodynamic Therapy: From Small Molecules and Nanoparticles toward Clinical Development. *Small* **2021**, *17* (42), 2101976. https://doi.org/10.1002/smll.202101976.

(370) Costley, D.; Mc Ewan, C.; Fowley, C.; McHale, A. P.; Atchison, J.; Nomikou, N.; Callan, J. F. Treating Cancer with Sonodynamic Therapy: A Review. *International Journal of Hyperthermia* **2015**, *31* (2), 107–117. https://doi.org/10.3109/02656736.2014.992484.

(371) Canta, M.; Cauda, V. The Investigation of the Parameters Affecting the ZnO Nanoparticle Cytotoxicity Behaviour: A Tutorial Review. *Biomater. Sci.* **2020**, *8* (22), 6157–6174. https://doi.org/10.1039/D0BM01086C.

(372) Blanco, E.; Shen, H.; Ferrari, M. Principles of Nanoparticle Design for Overcoming Biological Barriers to Drug Delivery. *Nature Biotechnology* **2015**, *33* (9), 941–951. https://doi.org/10.1038/nbt.3330.

(373) Gratton, S. E. A.; Ropp, P. A.; Pohlhaus, P. D.; Luft, J. C.; Madden, V. J.; Napier, M. E.; DeSimone, J. M. The Effect of Particle Design on Cellular Internalization Pathways. *Proceedings of the National Academy of Sciences* **2008**, *105* (33), 11613–11618. https://doi.org/10.1073/pnas.0801763105.

(374) Miller, C. R.; Bondurant, B.; McLean, S. D.; McGovern, K. A.; O'Brien, D. F. Liposome−Cell Interactions in Vitro: Effect of Liposome Surface Charge on the Binding and Endocytosis of Conventional and Sterically Stabilized Liposomes. *Biochemistry* **1998**, *37* (37), 12875–12883. https://doi.org/10.1021/bi980096y.

(375) Maret, W. Zinc in Cellular Regulation: The Nature and Significance of "Zinc Signals." *Int J Mol Sci* **2017**, *18* (11), 2285. https://doi.org/10.3390/ijms18112285.

(376) Krężel, A.; Maret, W. Zinc-Buffering Capacity of a Eukaryotic Cell at Physiological PZn. *J Biol Inorg Chem* **2006**, *11* (8), 1049–1062. https://doi.org/10.1007/s00775-006-0150-5.

(377) Maret, W. Zinc Biochemistry: From a Single Zinc Enzyme to a Key Element of Life. *Advances in Nutrition* **2013**, *4* (1), 82–91. https://doi.org/10.3945/an.112.003038.

(378) Li, S.-S.; Zhang, M.; Wang, J.-H.; Yang, F.; Kang, B.; Xu, J.-J.; Chen, H.-Y. Monitoring the Changes of PH in Lysosomes during Autophagy and Apoptosis by Plasmon Enhanced Raman Imaging. *Anal. Chem.* **2019**, *91* (13), 8398–8405. https://doi.org/10.1021/acs.analchem.9b01250.

(379) Ohkuma, S.; Poole, B. Fluorescence Probe Measurement of the Intralysosomal PH in Living Cells and the Perturbation of PH by Various Agents. *Proceedings of the National Academy of Sciences* **1978**, *75* (7), 3327–3331. https://doi.org/10.1073/pnas.75.7.3327.

(380) Nowak-Lovato, K. L.; Wilson, B. S.; Rector, K. D. SERS Nanosensors That Report PH of Endocytic Compartments during FcεRI Transit. *Anal Bioanal Chem* **2010**, *398* (5), 2019–2029. https://doi.org/10.1007/s00216-010-4176-8.

(381) Degen, A.; Kosec, M. Effect of PH and Impurities on the Surface Charge of Zinc Oxide in Aqueous Solution. *Journal of the European Ceramic Society* **2000**, *20* (6), 667–673. https://doi.org/10.1016/S0955-2219(99)00203-4.

(382) Martin, S. J.; Reutelingsperger, C. P.; McGahon, A. J.; Rader, J. A.; van Schie, R. C.; LaFace, D. M.; Green, D. R. Early Redistribution of Plasma Membrane Phosphatidylserine Is a General Feature of Apoptosis Regardless of the Initiating Stimulus: Inhibition by Overexpression of Bcl-2 and Abl. *Journal of Experimental Medicine* **1995**, *182* (5), 1545–1556. https://doi.org/10.1084/jem.182.5.1545.

(383) Zhang, G.; Gurtu, V.; Kain, S. R.; Yan, G. Early Detection of Apoptosis Using a Fluorescent Conjugate of Annexin V. *BioTechniques* **1997**, *23* (3), 525–531. https://doi.org/10.2144/97233pf01.

# Appendix

## List of publications

M. Carofiglio, S. Barui, V. Cauda, M. Laurenti "**Doped zinc oxide nanoparticles: synthesis, characterization and potential use in nanomedicine**" APPLIED SCIENCES, 2020, Vol. 10(15), pp. 5194, EISSN 2076-3417, doi: 10.3390/app10155194

M. Laurenti; M. Grochowicz; E. Dragoni; M. Carofiglio; T. Limongi; V. Cauda "**Biodegradable and Drug-Eluting Inorganic Composites Based on Mesoporous Zinc Oxide for Urinary Stent Applications**". MATERIALS 2020, Vol. 13, pp. 3821, doi: 10.3390/ma13173821

M. Carofiglio, M. Laurenti, G.G. Genchi, G. Ciofani, M. Grochowicz, V. Cauda "**Ultrasound triggered ZnO-based devices for tunable and multifaceted biomedical applications**". ADVANCED MATERIALS INTERFACES – 2021, 8, 21, doi:10.1002/admi.202101021.

M. Carofiglio, M. Laurenti, V. Vighetto, L. Racca, S. Barui, N. Garino, R. Gerbaldo, F. Laviano, V. Cauda "**Iron-Doped ZnO Nanoparticles as Multifunctional Nanoplatforms for Theranostics. Nanomaterials**" NANOMATERIALS, 2021; 11(10):2628. doi: 10.3390/nano11102628

V. Vighetto, A. Troia, M. Laurenti, M. Carofiglio, N. Marcucci, G. Canavese, V. Cauda "**Insight into Sonoluminescence Augmented by ZnO-Functionalized Nanoparticles**". ACS Omega – 2022; 7, 8, 6591-6600, doi: 10.1021/acsomega.1c05837

M. Carofiglio, M. Conte, L. Racca, V. Cauda "**Synergistic phenomena between iron-doped ZnO nanoparticles and shock waves exploited against pancreatic cancer cells**" ACS Applied Nanomaterials, doi:10.1021/acsanm.2c04211

S. Barui, N. M. Percivalle, M. Conte, B. Dumontel, L. Racca, M. Carofiglio, V. Cauda "**Development of doped ZnO-based biomimicking and tumor targeted nanotheranostics to improve pancreatic cancer treatment**", Cancer Nanotechnology, doi: 10.1186/s12645-022-00140-z

V. Cauda, S. Appendino, V. Vighetto, M. Carofiglio "**Stimuli-responsive hybrid nanoconstructs for efficient theranostic applications in nanomedicine**", The Project Repository Journal, doi: 10.54050/PRj1519538

N. M. Percivalle, M. Carofiglio, M. Conte, G. Rosso, A. Bentivogli, G. Mesiano, V. Vighetto, V. Cauda "**Artificial and Naturally Derived Phospholipidic Bilayers as Smart Coatings of Solid-state Nanoparticles: Current Works and Perspectives in Cancer Therapy**", International Journal of Molecular Sciences, doi: 10.3390/ijms232415815

L. Racca, G. Rosso, M. Carofiglio, S. Fagonee, G. Mesiano, F. Altruda, V. Cauda "**Effective combination of biocompatible zinc oxide nanocrystals and high-energy shock waves for the treatment of colorectal cancer**", Cancer Nanotechnology, under review

## Patents

"**A sonoluminescence contrast imaging method and apparatus assisted by nanoparticles in the biomedical field, in particular in the oncological field**" (Original title: "Metodo ed apparato per immagine di contrasto in

sonoluminescenza assistita da nanoparticelle in ambito medico diagnostico, in particolare oncologico"). Italian Patent Application N. IT102021000005123 of 8th March 2021, Inventors: V. Cauda, V. Vighetto, M. Carofiglio, A. Ancona, granted.

## Attended conferences and schools

**School of Nanomedicine** – University of Trieste, Trieste, Italy – 2019

Poster presentation: "*Nano and Micro-structured Zinc Oxide Films Inhibit Bone Tumoral Cell Growth*". M. Carofiglio, M. Laurenti, G.G. Genchi, G. Ciofani, D. Pugliese, M. Grochowicz, V. Cauda.

**CancerTO** – UniTO and PoliTO conference series in cancer, Nanoscience in Cancer Immunotherapy, Turin, Online event, Italy – 2021

Poster presentation: "*Development of multifunctional iron-doped ZnO nanoparticles addressing pancreatic cancer cells*". M. Carofiglio, M. Laurenti, L. Racca, S. Barui, N. Garino, V. Cauda.

**Virtual Workshop – Latest advances in Urinary Stents. Biomaterials, Technology and Coatings** – Online event – 2021

Oral session: "*Layered ZnO microparticles-based films for remotely-activated antimicrobial activity*". M. Carofiglio, M. Laurenti, G.G. Genchi, G. Ciofani, M. Grochowicz, V. Cauda.

**NanoMedicine International Conference and Exhibition 2021** – Milano, Italy – 2021

Poster session: "*Synthesis and characterization of multifunctional iron-doped ZnO nanoparticles for anti-tumoral applications*". M. Carofiglio, M. Laurenti, L. Racca, S. Barui, N. Garino, V. Cauda.

**American Advanced Materials Congress** – International Association of Advanced Materials, Miami, USA – 2022

Poster session: "*Synergy between iron doped ZnO nanoparticles and pressure waves: a novel approach against pancreatic cancer cells*". M. Carofiglio, L. Racca, M. Laurenti, M. Conte, V. Vighetto, V. Cauda.